Report Title: Design Optimization of Liquid Fueled High Velocity Oxy-

Fuel Thermal Spraying Technique for Durable Coating for

Fossil Power Systems

Type of Report: Final

Reporting Period: July 8, 2012 – December 31, 2015

Principal Author: Ahsan R. Choudhuri, PhD

Date Report Issued: November 4, 2016

DOE Award Number: DEFE0008548

Submitting Organization: The University of Texas El Paso

500 W. University, ENG. Annex Suite A126

El Paso, TX 79968

Disclaimer:

This report was prepared as an account of work sponsored by an agency of the United States Government. Neither the United States Government nor any agency thereof, nor any of their employees, makes any warranty, express or implied, or assumes any legal liability or responsibility for the accuracy, completeness, or usefulness of any information, apparatus, product, or process disclosed, or represents that its use would not infringe privately owned rights. Reference herein to any specific commercial product, process, or service by trade name, trademark, manufacturer, or otherwise does not necessarily constitute or imply its endorsement, recommendation, or favoring by the United States Government or any agency thereof. The views and opinions of authors expressed herein do not necessarily state or reflect those of the United States Government or any agency thereof.

Abstract

High-velocity oxy-fuel (HVOF) thermal spraying was developed in 1930 and has been commercially available for twenty-five years. HVOF thermal spraying has several benefits over the more conventional plasma spray technique including a faster deposition rate which leads to quicker turn-around, with more durable coatings and higher bond strength, hardness and wear resistance due to a homogeneous distribution of the sprayed particles. HVOF thermal spraying is frequently used in engineering to deposit cermets, metallic alloys, composites and polymers, to enhance product life and performance. HVOF thermal spraying system is a highly promising technique for applying durable coatings on structural materials for corrosive and high temperature environments in advanced ultra-supercritical coal-fired (AUSC) boilers, steam turbines and gas turbines. HVOF thermal spraying is the preferred method for producing coatings with low porosity and high adhesion. HVOF thermal spray process has been shown to be one of the most efficient techniques to deposit high performance coatings at moderate cost. Variables affecting the deposit formation and coating properties include hardware characteristics such as nozzle geometry and spraying distance and process parameters such as equivalence ratio, gas flow density, and powder feedstock. In the spray process, the powder particles experience very high speeds combined with fast heating to the powder material melting point or above. This high temperature causes evaporation of the powder, dissolution, and phase transformations. Due to the complex nature of the HVOF technique, the control and optimization of the process is difficult. In general, good coating quality with suitable properties and required performance for specific applications is the goal in producing thermal spray coatings. In order to reach this goal, a deeper understanding of the spray process as a whole is needed. Although many researchers studied commercial HVOF thermal spray systems, there exists a lack of fundamental understanding of the effect of hardware characteristics and operating parameters on HVOF thermally sprayed coatings. Motivated by these issues, this study is devoted to investigate the effect of hardware characteristics (e.g. spraying distance) and operating parameters (e.g. combustion chamber pressure, equivalence ratio, and total gas flow rate) on HVOF sprayed coatings using Inconel 718 alloy. The current study provides extensive understanding of several key operating and process parameters to optimize the next generation of HVOF thermally sprayed coatings for high temperature and harsh environment applications. A facility was developed to support this endeavor in a safe and efficient way, including a HVOF thermal spray system with a Data Acquisition and Remote Controls system (DARCS). The coatings microstructure and morphology were examined using X-Ray Diffraction (XRD), Scanning Electron Microscope (SEM) and Nanoindentation.

Table of Contents

List of Tables	6
List of Figures	7
Chapter 1: Introduction	9
1.1 Overview	9
1.2 Advantages of HVOF Thermal Spray Systems	13
1.3 Problem Statement	15
1.4 Practical Relevance	15
1.5 Research Objectives	16
1.6 Center for Space Exploration Technology Research (cSETR)	17
1.7 Report Organization	17
Chapter 2: Literature Review	18
2.1 Introduction	18
2.2 Numerical/Computational Studies	18
2.3 Experimental Studies	21
2.3.1 HVOF Spraying Parameters Affecting Coating Quality	21
2.3.2 Mechanical and Chemical Properties of HVOF Coatings	23
2.3.3 Coating Powder Characterizations	25
Chapter 3: Experimental Setup & Technical Approach	27
3.1 Methodology	27
3.1.1 Injector	28
3.1.2 Combustion Chamber	30
3.1.3 Converging-Diverging Nozzle	32
3.1.4 Barrel	33
3.1.5 Cooling Jacket	34
3.2 Experimental Setup	35
3.3 Safety Considerations	46
Chapter 4: Computational Fluid Dynamics (CFD) Study	48
4.1 Introduction	48
4.2 Methodology	48
4.3 Modeling Parameters	50
4.4 Results & Discussion	51
4.5 Summary & Conclusions	57
Chapter 5: Results and Discussions	58

5.1. Gas-Fueled HVOF Thermal Spray Gun Design	58
5.1.1 Initial Hot Firing Tests	59
5.1.2 Final Hot Firing Tests	59
5.2 Characterization of Coatings	60
5.2.1 Materials Preparation, Treatment, and Analysis	61
5.2.2 Operating and Process Parameters	62
5.2.3 Inconel 718	64
5.2.4 Iron Aluminide	69
Chapter 6: Conclusions and Future Work	74
6.1 Introduction	74
Chapter 7: Commercialization Plan for the HVOF Thermal Spray Gun	76
7.1 Executive Summary	76
7.2 Development Stage	
7.3 Revolutionizing the Commercialization Process	76
7.4 Solution: Best Practices	77
7.4.1 Automation	77
7.4.2 Analysis	79
7.4.3 Optimization	79
BIBLIOGRAPHY	80
Appendix A	86
Appendix B	93
B.1 Particle Image Velocimetry (PIV)	93
B.2 High Speed Two Color Pyrometer	94
List of Tables	
Table 1.1: Comparison of thermal spraying processes (Al-Shehri, 2011)	
Table 1.2: Benefits of using HVOF coatings (Metco, 2012)	
Table 4.1: Summary of working conditions	
Table 5.1: Summary of operating conditions and geometric parameters	
Table 5.2: Comparison of Mach numbers for the hardness (Inconel 718)	
Table 5.3: Comparison of Mach numbers for the hardness (FeAl)	

List of Figures

Figure 1.1: Coating deposition techniques (Al-Shehri, 2011)	9
Figure 1.2: Schematic diagram of thermally sprayed spherical particle impinged onto a flat substra	
Shehri, 2011)	10
Figure 1.3: Schematic Diagram of a Thermal Spray Metal Coating (Dolatabadi A, 2003)	10
Figure 1.4: Typical cross section of a thermal spray coating (Dolatabadi A, 2003)	11
Figure 1.5: Typical flame temperature and particle velocity operation ranges for various thermal s	pray
systems (Oksa, Turunen, T, Varis, & and Hannula, 2011)	11
Figure 1.6: Gas-fueled Diamond Jet HVOF thermal spray gun (Metco, 2012)	13
Figure 2.1: The process map concept for the HVOF thermal spray process (Oksa, Turunen, T, Van	
Hannula, 2011)	
Figure 3.1: 3-D cross-sectional schematic of the current HVOF thermal spray gun	27
Figure 3.2: a) 3-D Schematic of the utilized shear co-axial injector, b) Schematic diagram of one of	orifice in
the shear co-axial injector used for experiments	
Figure 3.3: Schematic of geometric parameters in a converging-diverging nozzle attached to comb	oustion
chamber	31
Figure 3.4: Schematic of a converging-diverging nozzle	32
Figure 3.5: Schematic of test rig for gas-fueled HVOF thermal spray system	36
Figure 3.6: Storage tank	37
Figure 3.7: Centrifugal pump	37
Figure 3.8: Liquid turbine flow meter.	37
Figure 3.9: Air to liquid heat exchanger	38
Figure 3.10: Axial fan	38
Figure 3.11: Bimetal thermometers	39
Figure 3.12: J-type thermocouple	39
Figure 3.13: Nitrogen solenoid valve.	40
Figure 3.14: Thermal gas flow meter	40
Figure 3.15: Schematic of coating particles seeder	40
Figure 3.16: Oxygen solenoid valve	41
Figure 3.17: Gas turbine flow meter	41
Figure 3.18: Methane solenoid valve	42
Figure 3.19: Thermal gas flow meter.	42
Figure 3.20: Pressure transducer	43
Figure 3.21: DC transformer	
Figure 3.22: DC Power Supply	43
Figure 3.23: DAQ card	
Figure 3.24: LabVIEW interface	
Figure 3.25: Electrical device diagram	
Figure 3.26: Schematic of utilized spray booth	46
Figure 4.1: Schematic of gun geometry and computational domain with dimensions shown	
Figure 4.2: Contours of cell volume	
Figure 4.3: Variation of gas static pressure with distance along the centerline of the computational	
a) Case B at three different equivalence ratios 0.9, 1.0, and 1.1, b) equivalence ratio of 1.1 at three	
different cases A, B, and C	52

Figure 4.4: Variation of gas Mach number with distance along the centerline of the computational doma	iin,
a) Case B at three different equivalence ratios 0.9, 1.0, and 1.1, b) equivalence ratio of 1.1 at three	
different cases A, B, and C	. 53
Figure 4.5: Variation of gas axial velocity with distance along the centerline of the computational domain	in,
a) Case B at three different equivalence ratios 0.9, 1.0, and 1.1, b) equivalence ratio of 1.1 at three	
different cases A, B, and C	. 53
Figure 4.6: Contours of axial velocity in Case C, a) at rich equivalence ratio of 1.1, b) at stoichiometric	
equivalence ratio of 1.0, c) at lean equivalence ratio of 0.9	. 54
Figure 4.7: Variation of gas axial temperature with distance along the centerline of the computational	
domain, a) Case B at three different equivalence ratios 0.9, 1.0, and 1.1, b) equivalence ratio of 1.1 at th	ree
different Cases A, B, and C	. 55
Figure 4.8: Contours of axial temperature in Case C, a) at rich equivalence ratio of 1.1, b) at stoichiome	tric
equivalence ratio of 1.0, c) at lean equivalence ratio of 0.9	. 56
Figure 5.1: Actual HVOF flames at different operating conditions a) Mach of 1.0 and $\phi = 1.1$ (rich)	
without coating particles, b) Mach of 1.0 and $\phi = 1.1$ (rich) with coating particles, and c) Mach of 1.4 ar	ıd
ϕ = 1.1 (rich) without coating particles	. 60
Figure 5.2: Grit blasting machine	. 62
Figure 5.3: Partially melted particle of the HVOF coating after annealing	. 63
Figure 5.4: XRD graph for Inconel 718	
Figure 5.5: SEM images for the fixed parameters 100mm and 700°C, with the different Ma=1, Ma=1.2,	
Ma=1.4 with a magnification of 25K	
Figure 5.6: SEM images for the fixed parameters 150mm and 700°C, with the different Ma=1, Ma=1.2,	
Ma=1.4 with a magnification of 25K	
Figure 5.7: Box plot of the data from the nanoindentation at 600°C	
Figure 5.8: Box plot of the data from the nanoindentation at 700°C	
Figure 5.9: XRD graph for Iron Aluminide (FeAl)	
Figure 5.10: SEM images at a scale of 1micrometer and illustrates the different Mach numbers at 700°C	
Figure 5.11: Box plot of the data from the nanoindentation at 600°C	
Figure 5.12: Box plot of the data from the nanoindentation at 700°C	
Figure 7.1: Linking strategic planning to project planning and execution (McCoy, 2007)	
Figure A.1: Detailed schematic of the injector	
Figure A.2: Detailed schematic of the combustion chamber	
Figure A.3: Detailed schematic of the converging-diverging nozzle	
Figure A.4: Detailed schematic of the barrel	
Figure A.5: Detailed schematic of the HVOF thermal spray gun	
Figure B.1: Basic principles of the PIV system	
Figure B.2: Interrogation areas in one PIV image	. 94

Chapter 1: Introduction

1.1 Overview

There are several coating deposition techniques available. An overview is given in Fig. 1.1. These techniques are divided into two common groups, metallic and non-metallic. Metallic coating deposition has three categories, hard facing is the most important in the context of this research. Hard facing is used to deposit thick coatings of wear resistant materials on either a worn component or a new component, which is subjected to wear in service (Al-Shehri, 2011). There are three techniques of hard facing available: welding, cladding and thermal spraying. Thermal spraying is of most importance in this research, hence the following sections concentrates on this technique, especially the High Velocity Oxy-Fuel (HVOF) technique.

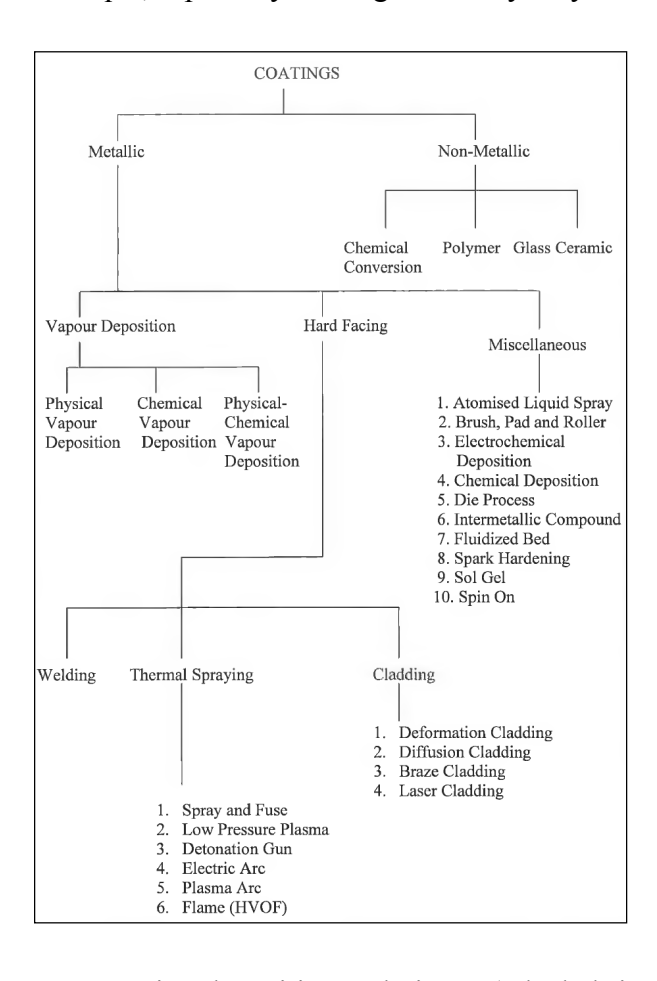


Figure 1.1: Coating deposition techniques (Al-Shehri, 2011)

Thermal spraying is a general term to describe all methods in which a coating is formed on a substrate from melted or semi-melted droplets. In thermal spraying, the material is in the form of a powder, wire or rod and is fed into the flame produced by a spray gun, the material then melts and the formed droplets are accelerated towards the substrate to be coated (Oksa, Turunen, T, Varis, & and Hannula, 2011). The thermal and kinetic

energy of the flame can be produced either with burning mixtures of fuel gas/liquid and oxygen, or by using an electrical power source. The process combines particle acceleration, heating, melting, spreading and solidification in a single operation. As the particles exit the gun and impact the substrate surface, they are flattened and firm thin splats or lamellae. See Fig. 1.2.

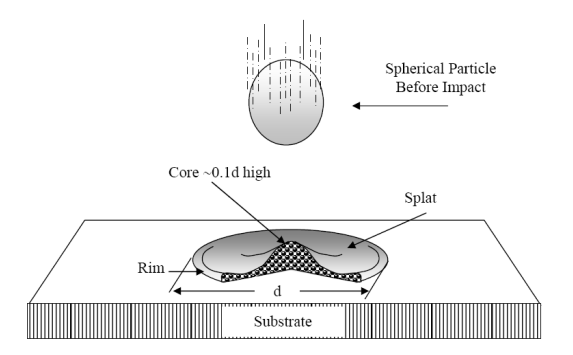


Figure 1.2: Schematic diagram of thermally sprayed spherical particle impinged onto a flat substrate (Al-Shehri, 2011)

Figures 1.3 and 1.4 exemplify a typical coating cross section of the lamellar structure of oxides and inclusions. Extensive use is made of thermal spraying in the aerospace, power generation and more recently in automotive industries to provide protective coatings on components that are exposed to heat, corrosion, and wear (Dolatabadi A, 2003).

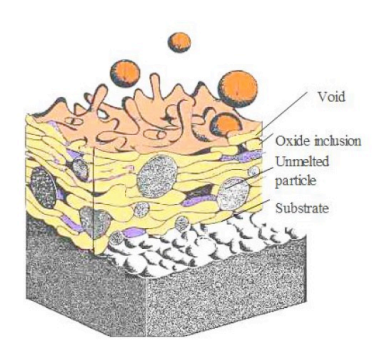


Figure 1.3: Schematic Diagram of a Thermal Spray Metal Coating (Dolatabadi A, 2003)

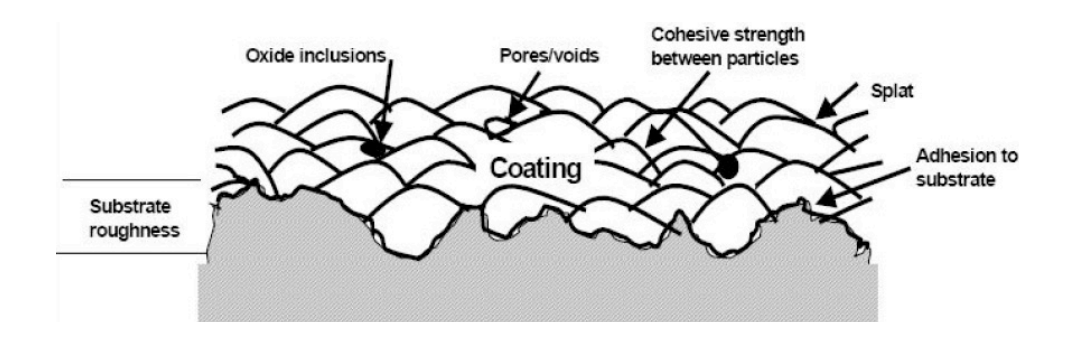


Figure 1.4: Typical cross section of a thermal spray coating (Dolatabadi A, 2003)

Thermal spray methods can be divided into a few main methodologies based on the energy source: i) plasma spray which includes atmospheric plasma spray, vacuum plasma spray, and low pressure plasma spray, ii) combustion flame spray, iii) high velocity oxy/air-fuel, iv) electrical arc, v) detonation, and vi) cold gas methods. Figure 1.5 demonstrates the typical operation ranges for the various spray systems.

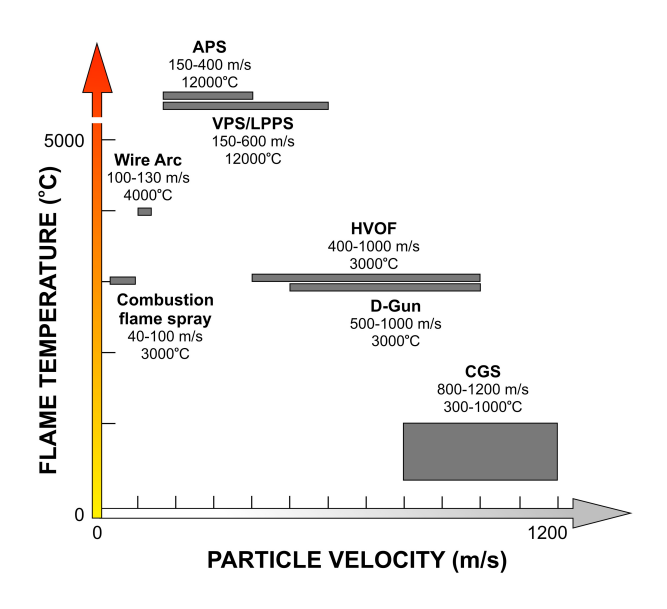


Figure 1.5: Typical flame temperature and particle velocity operation ranges for various thermal spray systems (Oksa, Turunen, T, Varis, & and Hannula, 2011)

Table 1.1 shows a comparison of thermal spraying process outputs. It is apparent that HVOF provides higher jet temperatures than flame spray, but lower than all other processes. Jet and particle velocities are higher than all other methods save for the detonation gun; its density range is greater than 95% corresponding to very high values, but the process has the disadvantage of moderate to dispersed oxides which may affect the overall durability of the coating (Al-Shehri, 2011).

Table 1.1: Comparison of thermal spraying processes (Al-Shehri, 2011)

Attribute	Flame spray	High-velocity oxyfuel	Detonation gun	Wire are	Air plasma	Vacuum plasma	Radiofrequency plasma
Jet							
Jet temperature, K Jet velocities, m/s (ft/s)	3500 50-100 (160-300)	5500 500-1200 (1600-4000)	5500 >1000 (>3300)	>25,000 50-100 (160-300)	15,000 300-1000 (1000-3300)	12,000 200-600 (700-2000)	10,000 20-80 (70-300)
Gas flow, sLm Gas types Power input, kW equiv.	O ₂ , acetylene 20	400-1100 CH ₄ , C ₃ H ₆ , H ₂ , O ₂ 150-300	N/A O ₂ , acetylene N/A	500–3000 Air, N ₂ , Ar 2–3	100–200 Ar, He, H ₂ , N ₂ 40–200	150-250 Ar, He, H ₂ 40-120	75–150 Ar, He, H ₂ 40–200 (plate)
Particle feed							
Particle temperature (max), °C (°F)	2500 (4500)	3300 (6000)	N/A	>3800 (>6900)	>3800 (>6900)	>3800 (>6900)	>3800 (>6900)
Particle velocities, m/s (ft/s)	50-100 (160-300)	200-1000 (700-3300)	N/A	50-100 (160-300)	200-800 (700-2600)	200-600 (700-2000)	20-50 (70-160)
Material feed rate, g/min	30-50	15-50	N/A	150-2000	50-150	25-150	20-50
Deposit/coating							
Density range (%)	85-90	>95	>95	80-95	90-95	90-99	95-99
Bond strength, MPa (ksi:)	7-18 (1-3)	68 (10)	82 (12)	10-40 (1.5-6)	<68 (<10)	>68 (>10)	>68 (>10)
Oxides	High	Moderate to dispersed	Small	Moderate to high	Moderate to coarse	None	None

In HVOF thermal spraying, heat is produced by burning a mixture of oxygen and fuel. Due to the spray gun design, a jet exiting the nozzle achieves supersonic speed. This allows for this technology to produce dense coatings with a low amount of degradation, oxidation of metallic materials, and phase transformations (Oksa, Turunen, T, Varis, & and Hannula, 2011). This feature is due to the short dwell time of the particles in the relatively cold flame. The HVOF process is used to produce cermet, metal coatings, and has also been used to deposit dense ceramic coatings on materials.

In the HVOF thermal spray process, fuel and oxygen are introduced to the combustion chamber together. The combustion of the gases produces a high temperature and high pressure in the chamber, contributing the supersonic flow of the gases through the nozzle. The powder particles used generally range in size from 5 μ m to 80 μ m and melt in the combustion chamber and during passage through the nozzle (Tabbara H, 2009). In some recent configurations, the powder particles melt or partially melt in the barrel section. For these oxy-combustion flames, temperatures can vary in the range of 2500 °C to 3200 °C, depending on fuel type, oxygen to fuel ratio, and gas pressure. Various other parameters also dictate the rate at which the particles melt including flame temperature, particle dwell time, material melting point, and thermal conductivity.

Figure 1.6 shows schematic of a gas-fueled Diamond Jet HVOF thermal spray gun. The gun consists of five main components including injector, combustion chamber, converging-diverging nozzle, barrel, and cooling jacket (Metco, 2012). Most general HVOF thermal spraying systems use this type of configuration. Geometries of combustion chamber volume, nozzle throat diameter, converging/diverging section angle,

and barrel length remain exclusive to each model and design based on the desired exit parameters (Tabbara H, 2009).

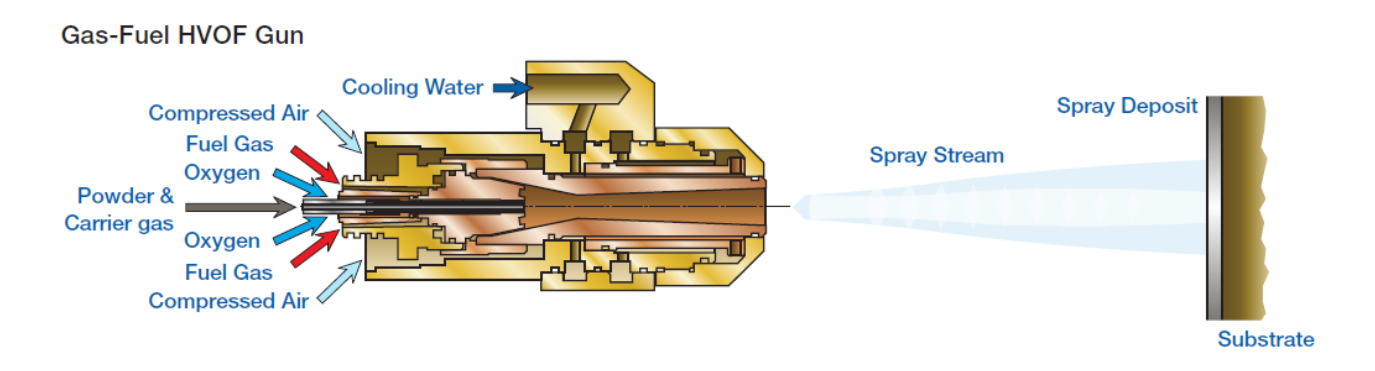


Figure 1.6: Gas-fueled Diamond Jet HVOF thermal spray gun (Metco, 2012)

Different HVOF thermal spray systems exist with partly different gun designs and capacities. Each gun design currently used can be divided into first, second, and third generations each having differences based on certain fundamental principles and desired outputs (Zhang D, 2003) (Swank WD, 1994). In first and second generation HVOF thermal spray guns, the pressurized burning of gaseous fuel with oxygen is used to produce an exhaust jet traveling at a speed of about 2000 m/s. The main fundamental difference between the first and second generation is the design of the nozzle. In the first generation gun design, there is typically a relatively large combustion chamber and a straight nozzle. For this type of design a maximum sonic velocity can be produced at the nozzle exit (Oksa, Turunen, T, Varis, & and Hannula, 2011). The second-generation type nozzle is based on the 'de Laval' nozzle, which enables higher than sonic velocities in the diverging part of the nozzle. Under standard spray conditions, the systems are operated at a power rating of about 100 kW and are capable of spraying about 2 to 3 kg/h of tungsten carbide-cobalt particles. Third generation systems have power ratings ranging from 100 to 300 kW, exhibit higher chamber pressures ranging from 0.8 to 2.5 MPa, and are capable of spray rates up to about 10 kg/h of tungsten carbide-cobalt particles.

1.2 Advantages of HVOF Thermal Spray Systems

Particle velocity is very important in thermal spray processes; higher velocity results in higher bond strengths, lower porosity, as the particle has less time to cool down at high velocities, thus impacts a substrate in a semi-molten state. The HVOF process is designed around producing these high velocities. The advantages that HVOF has over other thermal spray processes in terms of particle condition (Oksa, Turunen,

T, Varis, & and Hannula, 2011) including:

- a) Lower flame temperature compared with plasma spraying
- b) More favorable environment due to less oxidizing atmosphere
- c) Strongly limited reaction and phase transformations
- d) High compressive residual stress possible
- e) Strong adhesion to substrates
- f) High cohesive strength
- g) High density
- h) Lower capital cost and ease of use compared to other processes
- i) More uniform and efficient particle heating due to high turbulence
- j) Reduced mixing with ambient air once jet and particle leave the gun
- k) Thicker coatings than with plasma and arc spraying can be produced
- 1) Lower ultimate particle temperatures compared to other processes
- m) Process can be automated
- n) Smooth as-sprayed surface finish
- o) Excellent machined surface finish

Table 1.2 summarizes the reasons the HVOF process produces such high quality coatings.

Table 1.2: Benefits of using HVOF coatings (Metco, 2012)

Coating Benefit	Main Reasons for this Benefit
Higher density (lower porosity)	Higher impact energy
Improved corrosion barrier	Less porosity
Higher hardness ratings	Better bonding, less degradation
Improved wear resistance	Harder, tougher coating
Higher bond and cohesive strengths	Improved particle bonding
Lower oxide content	Less in-flight exposure time to air
Fewer un-melted particle content	Better particle heating
Greater chemistry and phase retention	Reduced time at higher temperatures
Thicker coatings (per pass & total)	Less residual stress
Smoother as-sprayed surfaces	Higher impact energies

1.3 Problem Statement

Although porosities are normal and necessary in Thermal Barrier Coatings (TBCs); heat treatment and usual service allow hot corrosive gas to reach the coated material, forming Thermally Grown Oxide (TGO) layers (Jang HJ, 2006). Failure of TBCs occurs mostly by cracking, delamination and spallation of the coating at a TGO layer; this layer is created during heat transfer and while in service, causing eventual crack growth and catastrophic failure. The bond coat plays a very important role in ensuring structural effectiveness and adhesion of the ceramic coating to the coated material. For this reason, there is a necessity to understand and develop increasingly reliable coating techniques.

An inherent problem of the HVOF system is the fact that gas temperatures are above the melting point of alloys and metals employed in spray powder. Particles may experience oxidation while traveling in the hot gas flow or when impinging on the substrate, resulting in the degradation of the top coat and affecting its overall properties (Katanoda H, 2011). The microstructure of the deposit and its mechanical characteristics are dictated by the velocity, temperature, and oxygen content of particles at the point of impingement. These characteristics are dependent on the physical and chemical state of coating particles upon impact, namely melting degree, velocity and oxidation properties (Tabbara & Gu, 2009) (Li M, 2003). An understanding of the mechanical and chemical properties, as well as failure mechanisms of the bond coat is essential to improve reliability and lifetime performance of coatings developed by this method (Jang HJ, 2006).

1.4 Practical Relevance

The discovery, design and development of the next-generation corrosion resistance coatings with enhanced thermal durability and reliability for high temperature environment are the most compelling requirements of the ever increasing performance needs for the next generation fossil power systems. The development of new coatings is limited, in part, by the available materials and coating technologies. New coating materials and engineering the coating with novel manufacturing processes must be developed in order to develop the coatings with unique struactural, tehrmal, thermo-chemical, and mechnaical properties for Advanced Ultra-supercritical Coal-Fired (AUSC) boilers, steam turbines, and gas turbines.

Experimental and computational efforts in this study will be directed towards understanding and optimizing operating and process parameters of gas-fueled HVOF thermal spray systems in order to produce highly durable high temperature corrosion resistance coatings. Gas-fueled HVOF thermally sprayed Inconel 718 coatings are expected to provide coatings that are much more unique in terms of micro-structure and thermo-

chemical characteristics. Inconel 718 is a nickel-based super alloy that is extensively used in a broad range of applications such as turbine blades, power generation, petroleum and nuclear reactor technology due to its good mechanical properties at intermediate and high temperatures.

Understanding the behavior and properties of Inconel 718 coatings will bridge the knowledge gap and enhance our ability to find excellent corrosion resistance coatings for high temperature extreme environments. Major outcomes of the proposed studies will be: (1) availability of an extensive operating and process parameters for industrial implementation of gas-fueled HVOF thermal spray systems and (2) realization of next-generation high temperature Inconel 718 corrosion resistance coatings for Advanced Ultra-supercritical Coal-Fired boilers, steam turbines, and gas turbines applications.

1.5 Research Objectives

While there have been several research projects related to the characterization of HVOF coatings, few works have considered the relationship between characterization of coatings and specific gun operating and process parameters. A thorough understanding of gas dynamics and particle behavior must be obtained through experimental and computational studies in order to develop the next-generation of high performance HVOF thermal spray systems.

The overarching aim of the current study is to enhance the understanding of relationships between operating and process parameters of HVOF thermal spraying systems and coating characteristics in order to optimize the effectiveness through two objectives. The first objective is to design and test a gas-fueled HVOF thermal spray system to investigate the particle dynamics using Inconel 718 alloy for a range of operating and process parameters (equivalence ratio, total gas flow rate, combustion chamber pressure, and spraying distance). The micro-structural and physical characteristics of HVOF-produced coatings are critically dependent on the physical, thermo-chemical states, and coating particles dynamics. The ultimate goal is to generate extensive data set quantifying the effects of these fundamental parameters on particle dynamics of HVOF thermal spray system and to ultimately relate them to the physical properties of coatings (Objective 2). Inconel 718 particles will be primarily used for most experimental measurements for technical tasks under Objective 1. The use of Inconel 718 particles will allow validating present measurements with some recently published computational data of particle dynamics in HVOF thermal spray systems. The second objective is to study the effect of operating and process parameters on coating characteristics. Detailed understanding of the structure and morphology of Inconel 718 coatings will be investigated using: X-ray diffraction (XRD) and high resolution scanning electron microscopy (SEM) coupled with Nanoindentation to measure hardness.

1.6 Center for Space Exploration Technology Research (cSETR)

The cSETR is a laboratory located at The University of Texas at El Paso (UTEP) focused on combustion, non-toxic based propulsion systems, material development, in-situ resource utilization, and fuel research for space systems and technology development. The work conducted in the lab uses novel experimental techniques and world class imaging capabilities. A general synopsis of applications the research performed at cSETR are gas turbine premixed burning optimization (preventing flashback), gas turbine blade efficiency improvement, gas turbine material strengthening for higher combustion temperatures, lunar regolith construction methods and techniques, meso-scale and micro propulsion development for miniature satellites, and non-toxic fuel research for environmentally conscientious combustion and propulsion systems.

cSETR's main mission is to provide world class research solutions while promoting professional development throughout its student researchers for the engineering workforce. The students that participate in lab projects and research gain novel experimental and theoretical application experience that compliments their academic studies. The hierarchy of the research is maintained with a professor providing close mentorship of a team of students that includes a doctoral graduate student managing at least two master's graduate students who in turn oversee any number of undergraduate students. This allows exemplary training of graduate students and at the same time cultivating next generation graduate students for program continuity in the laboratory.

1.7 Report Organization

The presented elements in this work are comprised of five main areas. These parts are the literature review, methodology and experimental setup, experimental results and discussions, computational fluid dynamics (CFD) study, and conclusions and future work. The literature review will discuss pertinent research about HVOF thermal spraying systems, coating characterization, and scope of the research. The methodology and experimental setup chapter presents theoretical and numerical approaches to design criteria and components used in the current HVOF thermal spray system. The testing conducted and results are then presented. A discussion then reflects on the results found in relation to theory and other work conducted. A thorough CFD study for different operating and process parameters follows the discussion section. Finally the work conducted and findings are summarized in the conclusion section along with recommendations for future work.

Chapter 2: Literature Review

2.1 Introduction

In order to be able to validate any study a review of previous investigations must be performed in order to examine their methods and compare their findings. A short summary of literature related to the subject follows below. Generally speaking, good coating quality, with suitable properties, and required performance for specific applications is the goal in producing thermal spray coatings. In order to reach this goal, a deeper understanding of the spray process as a whole is needed. The relationship between process parameters, measured particle state, coating microstructure and coating properties is described in Fig. 2.1.

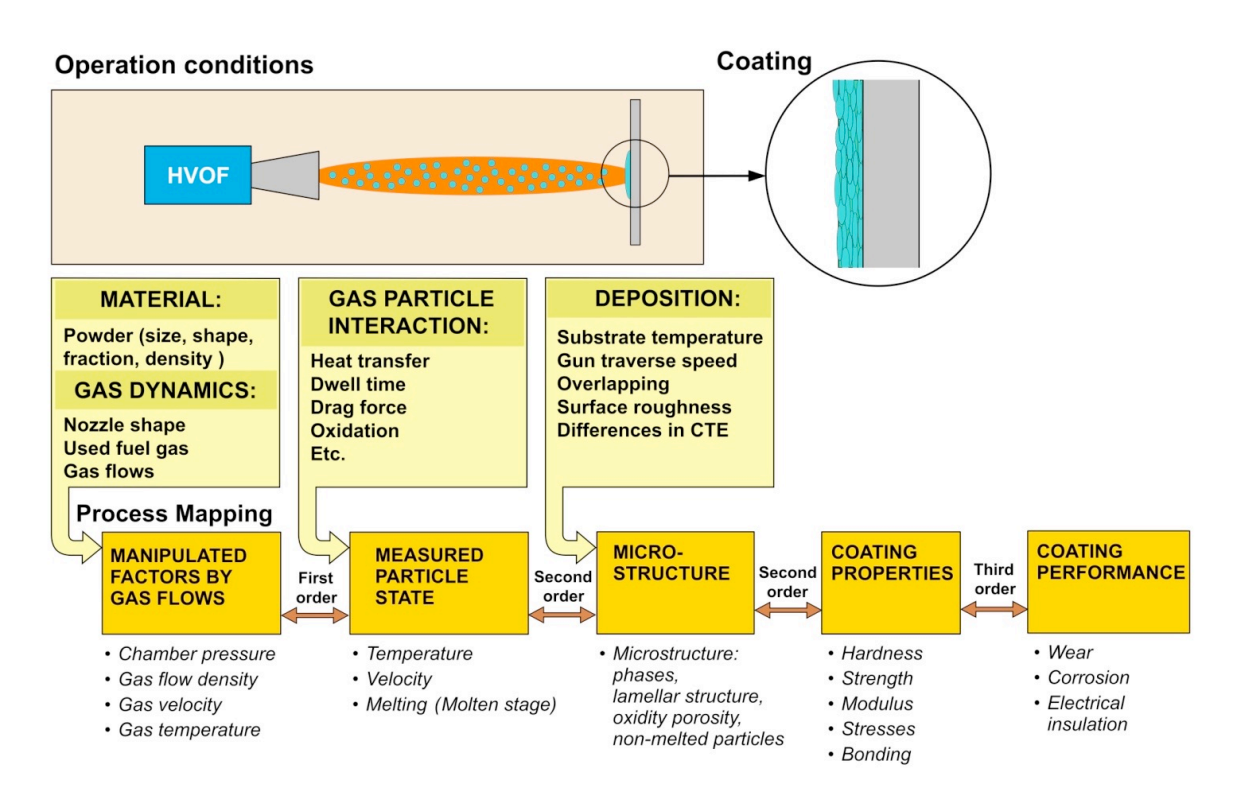


Figure 2.1: The process map concept for the HVOF thermal spray process (Oksa, Turunen, T, Varis, & and Hannula, 2011)

2.2 Numerical/Computational Studies

Past research of HVOF thermal spraying has been mainly focused on computational methods through the simulation of gas flow in two and three dimensions, using different computational approaches and codes, particularly ANSYS-CFX and ANSYS-FLUENT. Numerical modelling has become an important tool to

underpin the thermodynamics of thermal spraying process (Kamnis & Gu, 2006). Over the decades, many HVOF numerical models have been developed and have been able to provide insight to the gas flow, inflight particle dynamics, and even droplet impingement or coating formation. Furthermore, most of the modelling works are based on the gas fueled HVOF thermal spray systems (Power GD, 1991) (Smith EB, 1992) (Oberkampf WL, Analysis of a high velocity oxygen fuel (HVOF) thermal spray torch Part 1: numerical formulation, 1996) (Oberkampf WL, Analysis of a high velocity oxygenfuel (HVOF) thermal spray torch Part 2: computational results, 1996) (Hassan B, 1995) (Lopez AR, 1998) (Gu S, 2001) (Li M, 2003) (Cheng D X. Q., 2001) (Mostaghimi J, 2003). A thorough review on modelling developments can be found in the publication by Cheng et al. (Cheng D T. G., 2003).

Kamnis and Gu (Kamnis S G. S., 2005) reported the most systematic study for METJET (Kamnis & Gu, 2006) including the combusting gas flow (Kamnis S G. S., 2008) and the in-flight particle dynamics (Zeoli N, 2008) (Yang X, 1996). The computational study on METJET has shown that the thermodynamic flow field within the HVOF gun is sensitive to several parameters including the nozzle shape, oxygen–fuel ratio, fuel droplet size, and combustion chamber pressure. The design of the thermal spray gun is therefore critical in order to achieve consistency and a high performance from the coating.

Tabbara and Gu (Tabbara H, 2009) used a commercial CFD code to investigate flow regime and gas flow characteristics, particularly final temperature as a function of radial distance along the centerline. The study is one of the few to combine computational and experimental data. This investigation focused on the JP5000 geometry and changed mesh size to impact both throat diameter and chamber length. The research found a 20% decrease in throat diameter will induce a 60% increase in combustion chamber pressure, increasing downstream velocity as well; a flow of almost perfect condition was described through this geometrical change. A 20% reduction in combustion chamber length yielded realizable results, as there was not an excessive amount of fuel exiting the combustion chamber, and temperature and velocity profiles were not affected significantly. In addition, the study investigated the influence of droplet size on gas flow and flame shape, investigating the complications that accompany using liquid in an HVOF system. The investigation implies that optimization of industrial models is achievable through computational means and that models can be refined; this remains to be tested however as design modifications and their experimental results must accompany such implications.

An additional computational study focused on gas-fuelled systems (Kamali & Binesh, 2009) yielded dependence between axial gas velocity and Mach number on total flow rate and mixture ratio; in this particular study the highest velocity was found to be achieved on the most fuel-rich ratio, corresponding to

mixing conditions found in industrial HVOF models.

Katanoda (Katanoda, Morita, Komatsu, & Kuroda, 2011) proposed an experimental procedure to estimate cooling rates for the combustion chamber, mixing chamber and the barrel section of an HVOF gun. A mathematical model was presented to effectively predict pressure and temperature in the mixing chamber for varying rates of fuel, oxygen and nitrogen.

Dongmo et al. (Dongmo, Wenzelburger, & Gadow, 2008) investigated and modelled a 3-D gun based on an Eulerian-Lagrangian formulation using the eddy dissipation model, which assumes the reaction rate is limited by the turbulent mixing rate (Dongmo, Wenzelburger, & Gadow, 2008); the study modelled the reaction rate of combustion according to the resultant mass flow of the reactants, namely CO_2 . Although a different oxidizer/fuel combination (oxygen-propane) is used for this study than for the configuration studied in this research, temperature and pressure reached 3000 K and 6 bar (Dongmo, Wenzelburger, & Gadow, 2008), similar enough to what is expected in oxygen-methane and oxygen-kerosene combustion. Additionally, the investigation enhanced their results through the modeling of particle injection to discover optimal powder sizing; the study concluded that small particles (< $20 \, \mu m$) are not suitable for this process due to their small mass inertia. Finally, the investigation recommended that fluid-structure coupling and impinging jet influence on the substrate be considered in further modelling approaches.

Li (Li & Christofides, 2005) investigated the former, studying particle melting parameters and substrate forming using a mathematical code; they concluded particles of moderate size achieve higher velocity, temperature and impact than both extremely large and very small ones. The study found that spray distance has a significant influence on both velocity and melting degree of particles with small sizes; varying this parameter is useful when investigating a new design. Using a mixture of propylene, oxygen and air, Li et al. found that Fuel/oxygen ratio plays a very important ratio in particle heating, as flame temperature can be varied through this constraint. An equivalence ratio of 1.2 for this mixture helped to maximize flame temperature and two-phase heat transfer; it is expressed that for industrial applications this is the optimum point for a standoff (distance to substrate) of 200 mm under various flow rates. Additionally, they note that a high total gas flow rate helps to maintain gas velocity and temperature in the free jet at optimal levels (Li & Christofides, 2005) for a longer distance leading to better momentum and heat transfer processes between gas and particulates. Generally speaking, the total particle velocity increases as the overall gas flow does, increasing high gas momentum flux in the free jet. Nonetheless, particles do not have to be necessarily fully melted to achieve low coating porosity as long as the deposition efficiency is high. Finally, the study noted that the carrier flow rate must be kept at a minimum to enhance overall transfer of heat, as long as particles

can be fed into the flow in the smoothest manner possible.

Basu et al. (Basu & Cetegen, 2008) focused on modeling a thermo physical process in liquid ceramic droplets injected into an HVOF generated jet. The investigation provided a model consisting of several sub-models including aerodynamic droplet break-up, and heat and mass transfer within individual droplets within an HVOF environment. A parametric study was presented according to initial droplet size, concentration of mineral dissolution and the external temperatures and velocities of the HVOF jet to explore processing and injection parameters leading to different morphologies. It was found that the high jet velocity induces shear break-up of the droplets into those of several μ m, leading to a better entrainment and heating within the jet. In this study, the flame at the nozzle exit was characterized by a centerline temperature of about 3000 K and velocities exceeding 800 m/s; in this case, the under expanded supersonic jet became subsonic downstream through a system of oblique shock waves forming a shock diamond pattern.

2.3 Experimental Studies

Experimental studies have focused heavily on microstructure characterization and certain elements of inflight particle diagnosis. There have been numerous experimental research works related to the characterization of HVOF thermally sprayed coatings of different alloys (Katanoda H, 2011) (Dongmo E, 2008) (Basu & Cetegen, 2008) (Jang, et al., 2006) (Kawakita J, 2006) (Sidhu TS, 2005) (Tang F, 2004) (Bach FW, 2004) (Heath GR, 1997). However, very few works have considered the characterization of coatings and the relevant operating and process parameters. The following sections provide brief review of the earlier studies carried out in this field with special attention to HVOF coating parametric, microstructural and mechanical properties. The literature review of these sections is characterized under three topics which are (i) HVOF spraying parameters affecting coating quality; (ii) mechanical and chemical properties of HVOF coatings; and (iii) thermal spray powder characterizations.

2.3.1 HVOF Spraying Parameters Affecting Coating Quality

Many variables could affect metallic coating properties, particularly unmelted particles and oxidation level. Flame parameters such as equivalence ratio, velocity (Mach number), and temperature, are very important. Only one study has been published for the most widely used JP5000 Praxair gun (Tabbara H, 2009). In the study sufficient information about the combustion processes and associated complex flow processes of the thermal spray system was not presented. The combination of computation and physical investigation has

seldom been encountered in this subject.

Gourlaouen studied stainless steel substrates to address the influence of the spray variables on the coating characterization (Goulaouen, 1998). He concluded that the influence of the combustion temperature was small. On the other hand, an increase of the flame power led to higher the oxidation with low unmelted particles rates and the deposition efficiency was improved. Among the three parameters studied, the equivalence ratio had significant influence. The increase of the equivalence ratio, decreases the oxygen content, and consequently of the microhardness. Also, the increase of the number of unmelted particles resulted in a decrease of the deposition efficiency.

Wei et al. (W.C. Lih, 2000) examined the effect of HVOF spray condition on molten particle velocity and surface temperature. He used carbide/nickel-chromium alloy as a coating powder. He studied oxygen to fuel ratio, fuel gas flow rate, powder carrier gas flow rate, powder feed rate, gun barrel length, stand-off distance and substrate surface speed. The microstructure and mechanical properties of the coating were examined. He concluded that the feed stock rate, standoff distance and gun barrel length played a main role in the output temperature of the molten particle. In addition, he said that sufficient enhancement in abrasion wear resistance was observed by depositing coating at higher particle velocity. He mentioned that coating deposited by molten particles that were heated at high temperatures, ranging from 1650 °C to 1725 °C, showed lower porosity content of the coating.

Kuroda et al. investigated the relationship between the conditions of sprayed particles and the stress generated during deposition (S. Kuroda, 2001). They used 316 L stainless steel for both the sprayed powder and the substrates to eliminate the stress due to difference in thermal expansion. They examined different powder sizes and particles velocities to control the kinetic energy. They found that a strong negative correlation existed between the temperature and diameter. In contrast, the correlation was very weak between the diameter and the velocity. They concluded that the process of the stress generation of the HVOF coating was more complicated compared to conventional thermal spray processes because of the peening action of the particles. Their results revealed that a broad window for the stress control was available through the control of spray parameters with the HVOF process.

Totemeier et al. investigated the effects of HVOF spray parameters on spray particle characteristics, deposition efficiency, and residual stresses (T.C. Totemeier, Residual Stresses in High Velocity Oxy-Fuel

Metallic Coatings, 2004). They tested Fe₃Al and AISI type 316 stainless steel coating materials. They studied three different spray conditions for each material; the spray particle characteristics (size, distributions, velocity,) were assessed for each material and spray condition. They found that increasing torch chamber pressure resulted in increasing spray particles velocity with little change in the spray particles' temperature. Also, relative deposition efficiencies were maximized at an intermediate particle velocity. They mentioned that residual stresses in coating on thin substrates became slightly less compressive with increasing coating thickness.

Zhao et al. (L. Zhoa, 2004) investigated the effect of spray conditions on the particle in flight properties and the properties of HVOF coating of WC-CoCr. The particle size distribution of WC-CoCr powder was - 45/+11 µm. They evaluated the microstructure, hardness and wear behavior of the coatings. Their results indicated that the particle and coating characterizations reached different levels because of spray parameters such as the total gas flow rate, the powder fees rate and standoff distance. They concluded that high particle velocity and high particle temperature were caused by increasing the total gas flow rate and lowering the powder feed rate with a short standoff distance. Also, they reported that the particle velocity showed more sensitivity to spray parameters than the particle temperature. In addition, increasing the particle temperature and velocity led to enhancing the coating hardness and decreasing the porosity. They mentioned that the total gas flow rate is more effective parameter than powder feed rate, which had more effect than standoff distance.

Hasan et al. (M. Hasan, 2008) studied the influence of the spray variables on residual stress buildup of HVOF functionally graded coatings. They illustrated that many parameters could affect the residual stress generated on the obtained coating, such as equivalence ratio and spray distance. They concluded that the spray distance had significant influence on the residual stress. Its increase led to increase the flight time of the particles which in turn, lower the impact velocity and temperature.

2.3.2 Mechanical and Chemical Properties of HVOF Coatings

Few current investigations have analyzed substrate coating features based on equipment design characteristics; those examinations focused on coating properties have done that by employing industry-supplied HVOF guns. Physical and mechanical properties of HVOF spray coatings can be analyzed through failure testing such as cyclic loading and performance under high temperature conditions (Jang HJ, 2006). Final coating characteristics may also be analyzed in a Scanning Electron Microscope (SEM) (Tang F, 2004)

for detailed visuals on porosity and composition.

Jang et al. (Jang H. P., 2006) studied Co-Ni alloy coatings on a nickel-based super-alloy substrate. In this investigation mechanical properties such as hardness 'H' and modulus of elasticity 'E' were studied as a function of the thickness of the bond coat, as these values are essential in improving reliability and lifetime performance for thermal environments. In their results, the interface between the HVOF applied bond coat and substrate showed a relatively continuous microstructure, with the bond coat appreciated to be quite dense (Jang, et al., 2006); on the other hand, those samples prepared by the Atomic Plasma Spray (APS) process showed slight cracking. Additionally, the thermally grown oxide (TGO) layer formed during fatigue tests tended to increase as a function of temperature and dwell time, but was found to be independent of applied bond coat thickness.

Padilla et al. (K. Padilla, 2002) conducted an experiment in order to study the effect of Ni-5 Mo-5.5 Al (wt. %) applied by HVOF, on the fatigue properties of AISI 4140 steel. The investigation was carried out by comparing the fatigue behavior of uncoated samples with those of the specimens after grit blasting and after blasting and coating with such a deposit. They carried out tensile and fatigue tests. They concluded that grit blasting gave rise to a significant decrease in the fatigue properties of the material. Further coating of the grit blasted samples, applied by HVOF, led to a further reduction in the fatigue strength of the material. They suggested that such a further decrease was mainly associated with two different causes. First, the extensive fracture and delamination of the coating from the substrate had been observed from the microscopic analysis. Secondly, the possible existence of tensile residual stresses in the substrate, in the vicinity of the substrate deposit interface which would assist in the propagation of the fatigue cracks nucleated at the alumina particles.

Stoica et al. (V. Stoica, 2004) investigated the sliding wear behavior of as sprayed and Hot Isostatically Pressed (HIPed) thermal spray cermet coating deposited by HVOF. They sprayed WC-12C coating powder on bearing steel substrate followed by HIPed at 850°C. They characterized the coating using X-Ray Diffraction (XRD), Scanning Electron Microscope (SEM) and microhardness test. They concluded that a sufficient enhancement of thermal spray cermet coating wear resistance was observed by hot isostatic pressing post treatment where this offered about 100% improvement in wear behavior of cermet coatings. This enhancement in physical characterizations was due to the phase transformations where secondary phase W₂C and metallic tungsten were eliminated.

Wielage et al. (B. Wielage, 2006) carried out two studies in order to develop a HVOF thermal spray system. Firstly, they conducted a study to evaluate the wear behavior of cermet coating deposited on light weight material parts subjected to dynamical load. The second study, using advanced HVOF gun with high combustion chamber pressure to reduce the particle temperature was investigated. This was because that the cheap belt grinding could be used to finish the former coating. They concluded that HVOF cermet coatings applied on light weight material showed an excellent wear behavior without detraction of fatigue strength. Also, nickel or iron base coating deposited by high combustion pressure had high corrosion resistance due to high density and low oxy-gen content in the coating.

2.3.3 Coating Powder Characterizations

Tan et al. (J. Tan, 1999) studied the repair of worn components using HVOF thermal spray. They used stainless steel as coating material as well as substrate to restore the worn parts to their original dimensions. They found that HVOF thermal spraying process could be extremely useful as an excellent technique to repair and restore damages with various depths in 2D tool steel substrates. Also, the thickness of 5.5 mm could be achieved if the properties of the coating material with the substrate material were matched. They concluded that WC-Co wasn't an appropriate selection to be used in such repairs.

Reisal et al. (G.Reisel, 2001) investigated the oxidation of unreinforced and reinforced molybdenum disilicade (MoSi₂) coatings. The samples were subjected to high temperature 5000°C, 1000 °C and 1500 °C. They used Scanning Electron Microscopy (SEM), Energy Dispersive X-Ray analysis (EDX) and X-Ray Diffraction analysis (XRD) to evaluate the coating characterization. In addition, they employed simultaneous thermo gravimetric equipment to study the oxidation behavior. They noticed that the porosity of the coating had a gradual effect on the pesting reaction of the MoSi₂ at 500 °C. At 1000 °C, the tests showed that no effect was observed of the heating rate on the short term oxidation properties. At 1500 °C, they reported that a protective SiO₂ layer was formed with a thickness of 10 µm for the unreinforced MoSi₂ coating.

Hu et al. (W. Hu, 2008) studied the properties of NiAl nanostructured coating produced by HVOF spraying. Ni and Al compound powder in the atomic ratio 50:50 were melded under Ar gas atmosphere. They used XRD, SEM coupled with EDS to examine the coating properties. They reported that increasing the milling time, reduces the grain size of the powder and increases the lattice constant. They found that HVOF thermal spraying of milled metallic powder was effective for producing Ni Al nanostructure coatings. They found that micro-hardness, dynamic hardness and elastic modulus of the coating decreased as heat treatment

increased. In addition, they figured out that increasing temperature led to a decrease in the high temperature
hardness.

Chapter 3: Experimental Setup & Technical Approach

This section describes the laboratory scale fluidized bed system with different apparatus used to study the hydrodynamics of gas-solid fluidized bed system. Experimental procedure, technical approach and theoretical considerations are also presented in this chapter. Section 3.1 describes the design parameter of 12.4 cm diameter fluidized bed reactor and air supply, control procedure. Section 3.2 describe about test particles selection, preparation and different parameter of particles. Section 3.3 describes about experimental measurement procedures.

3.1 Methodology

In this section, all components of utilized HVOF thermal spray system and methodologies are presented including the injector, combustion chamber, converging-diverging nozzle, barrel, and cooling jacket. In addition, this section includes the design equations, considerations, and technical issues. The foregoing design calculations provide the dimensions, thicknesses, and orifice sizes for the major components of a gasfueled HVOF thermal spray gun. Figure 3.1 shows the completed schematic for the newly designed HVOF thermal spray gun.

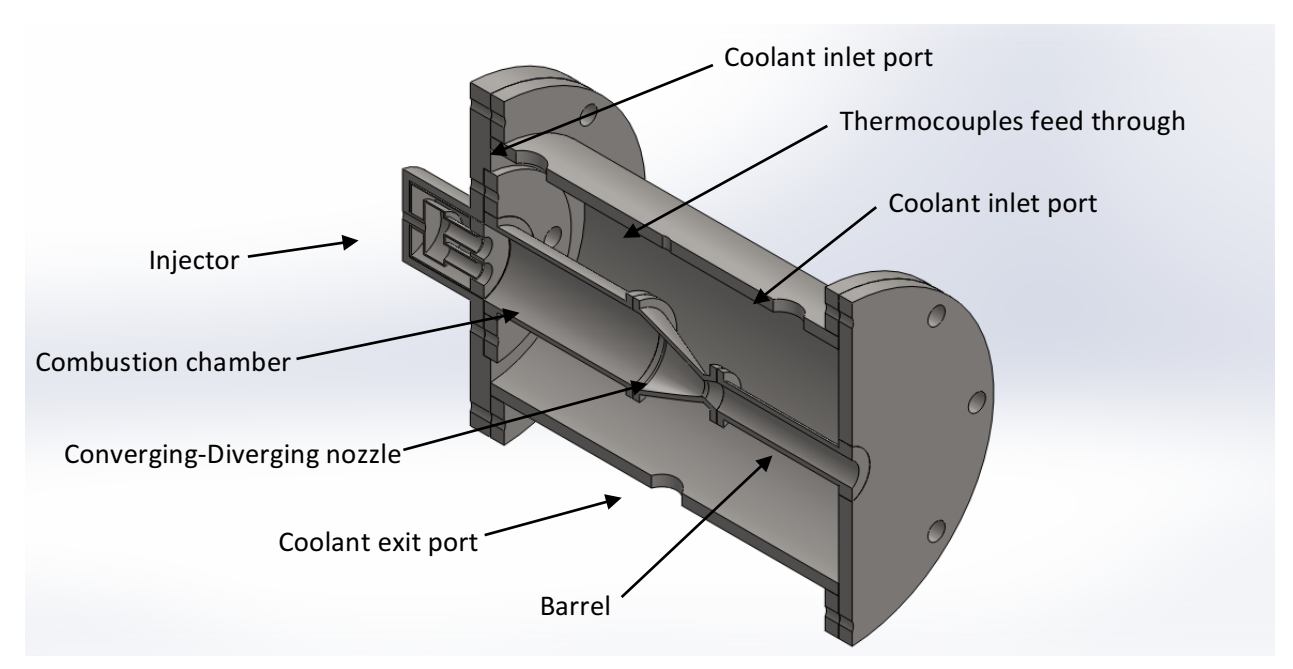


Figure 3.1: 3-D cross-sectional schematic of the current HVOF thermal spray gun

3.1.1 Injector

The function of the injector is to introduce the propellants into the combustion chamber in such a way that efficient combustion can occur. The utilized HVOF thermal spray gun in this study employs a shear co-axial injector in which oxidizer and gas fuel are fed under pressure from tanks into a combustion chamber. The propellants consist of gaseous methane along with oxidizer which for current experiments is gaseous oxygen. In the employed HVOF thermal spray gun, the main fuel line is divided into two lines right before the injector face. The first fuel line is partially premixed with the oxidizer line due to the existence of a small recess length between fuel and oxidizer orifices. The subsequent mixture is then injected into the combustion chamber through three even peripherally distributed orifices from the gun centerline. This design was selected since it would enhance mixing between the fuel and oxidizer. A detailed image of the injector system can be seen in Fig. 3.2.

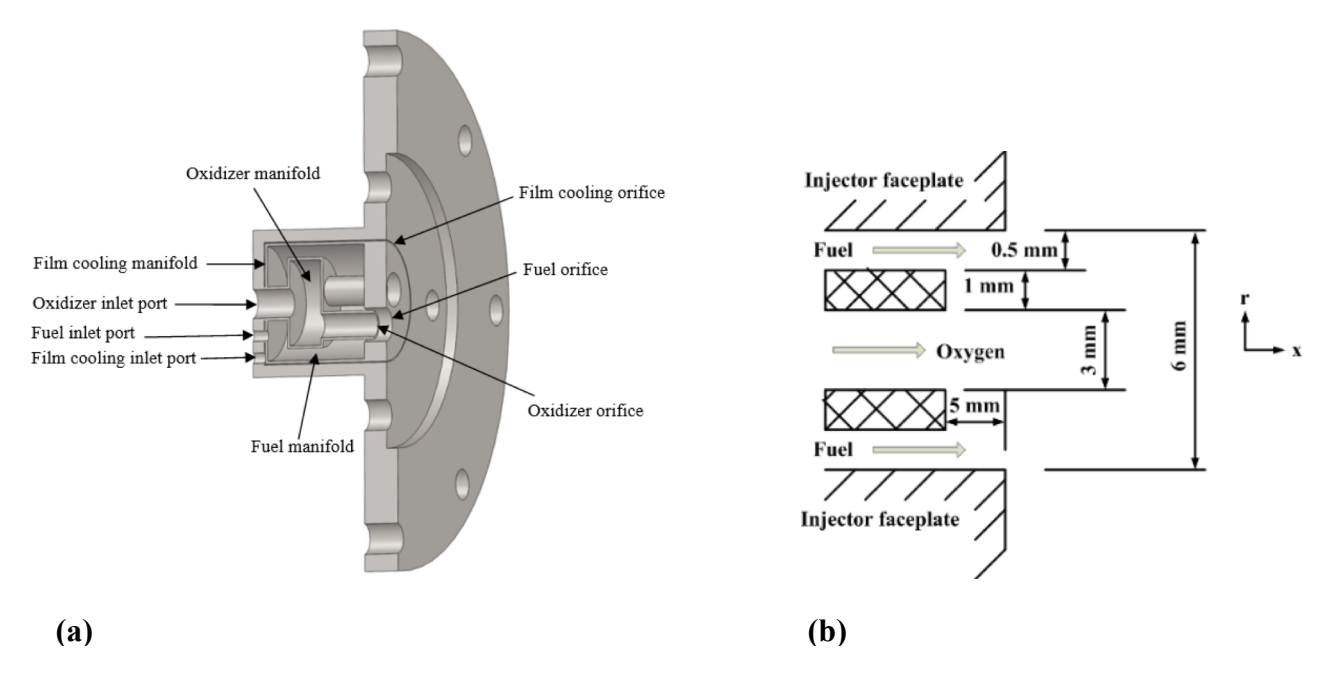


Figure 3.2: a) 3-D Schematic of the utilized shear co-axial injector, b) Schematic diagram of one orifice in the shear co-axial injector used for experiments

Since the fuel burning with oxygen near the stoichiometric equivalence ratio involves very high flame temperatures, a second fuel line enters the injector via a separate port and is injected through a special orifice, close to the chamber wall, to provide the chamber with a film of gas fuel to protect exposed combustion chamber wall surfaces. Film cooling protects the walls from excessive heat and lowers the mixture ratio of any errant streak.

Mass flow rates of total fuel and oxidizer can be calculated assuming the exhaust gas products are in gaseous

form. The equations used for the calculation of mass flow rate in the nozzle are from perfect gas law theory seen in Eqs. (1-6) (Huzel, 1992). These equations were used primarily to determine total propellants mass flow rate assuming the nozzle throat diameter is determined at the beginning of the design procedure.

$$m_{t}^{\circ} = \frac{A_{t} * P_{c}}{\pi} * \sqrt{\frac{\gamma * g}{R * T_{c}} * \left[\frac{2}{\gamma + 1}\right]^{\frac{\gamma + 1}{\gamma - 1}}}$$
 (1)

$$A_t = \frac{\pi D_t^2}{4} \tag{2}$$

$$R = \frac{\overline{R}}{M_{wt}} \tag{3}$$

$$m_t^{\circ} = m_0^{\circ} + m_f^{\circ} \tag{4}$$

$$m_o^\circ = \frac{m_t^\circ * {}^0/_F}{({}^0/_F + 1)} \tag{5}$$

$$m_{f}^{\circ} = \frac{m_{t}^{\circ}}{(0/_{F} + 1)}$$
 (6)

Where m_t° is the total propellants mass flow rate, A_t is the cross section area at nozzle throat, D_t is the throat diameter, P_c is the combustion chamber pressure, γ is the ratio of gas specific heats, g is the gravitational acceleration, R is the gas constant, R is the universal gas constant, R is the gas molecular weight, R is the propellants adiabatic flame temperature in combustion chamber, R is the oxidizer mass flow rate, R is the fuel mass flow rate, and R is the oxygen to fuel ratio.

Based on the output of Eqs. (1-6), injector orifices dimensions can be calculated from Eqs. (7-12) (Sutton, 2005).

$$A_f = \frac{m_f^{\circ}}{N * C_d * \sqrt{2 * g * \rho_f * \Delta P_f}}$$
 (7)

$$A_o = \frac{m_o^{\circ}}{N * C_d * \sqrt{2 * g * \rho_o * \Delta P_o}}$$
 (8)

$$\rho_f = \frac{P_f * \rho_{fatm}}{P_{atm}} \tag{9}$$

$$\rho_o = \frac{P_o * \rho_{o_{atm}}}{P_{atm}} \tag{10}$$

$$P_f = P_c + \Delta P_f \tag{11}$$

$$P_o = P_c + \Delta P_o \tag{12}$$

Where A_f is the fuel orifice cross section area, A_o is the oxidizer orifice cross section area, N is the number of orifices; ΔP_f is the injection pressure drop in the fuel line, ρ_f is the fuel density, ρ_{fatm} is the fuel density at atmospheric conditions, ρ_{oatm} is the oxidizer density at atmospheric conditions, C_d is a dimensionless discharge coefficient; ΔP_o is the injection pressure drop in the oxidizer line, ρ_o is the oxidizer density, P_f is the total pressure load in the fuel line, and P_o is the total pressure load in the oxidizer line.

The discharge coefficient is a function of injector orifice configuration. This value ranges from 0.5 to 0.92 and can be determined accurately by experimental means (Sutton, 2005) (Huzel, 1992). For a given injection velocity, a higher value of discharge coefficient results in a lower injection pressure drop. The injection pressure drop must be high enough to eliminate combustion instability inside the combustion chamber but must not be so high that the run tank and pressurization system used to supply fuel and oxygen to the gun are penalized (Huzel, 1992). These values were also taken into consideration during the design of the injection system.

3.1.2 Combustion Chamber

In order for the fuel and oxygen mixture to chemically react/burn to form hot gases, the chamber must be of sufficient length (Yang V, 2005). A parameter describing the chamber volume required for complete combustion is the characteristic chamber length, which is given by Eq. (13).

$$L^* = \frac{V_c}{A_t} \tag{13}$$

Here L* is the characteristic chamber length, and V_c is the combustion chamber volume.

The combustion chamber volume, V_c , includes the volumes of the chamber and the converging section of the nozzle (Huzel, 1992). To reduce losses due to flow velocity of gases within the chamber, the combustion chamber cross-sectional area should be at least three times the nozzle throat area (Sutton, 2005). Additionally, the chamber diameter for small combustion chambers should be three to five times the nozzle throat diameter so the injector will have useable face area (Huzel, 1992).

Chamber volume may be calculated from Eq. (14) assuming combustion chamber length and convergent nozzle half angle are known. A good value for the nozzle convergence half-angle, β , is from 20° to 45°; however, the nozzle divergence half-angle, α , should be no greater than 15° to prevent nozzle internal flow losses (Huzel, 1992), Fig. 3.3.

$$V_c = A_t \left[\frac{L_c * A_c}{A_t} + \frac{1}{3} \sqrt{\frac{A_t}{\pi}} * Cot \beta \left(\left(\frac{A_c}{A_t} \right)^{\frac{1}{3}} - 1 \right) \right]$$
 (14)

In Eq. (14) A_c is the combustion chamber cross section area, β is the convergent nozzle half angle, and L_c is the combustion chamber length.

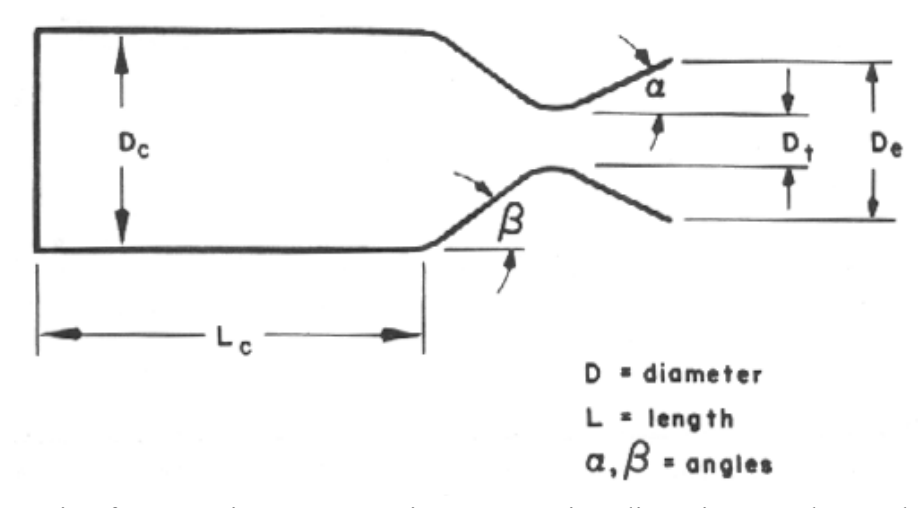


Figure 3.3: Schematic of geometric parameters in a converging-diverging nozzle attached to combustion chamber

In addition to geometrical considerations, the chamber must be strong enough to contain the high pressures and temperatures generated by the combustion process. In the current design the combustion chamber must be physically attached to the cooling jacket hence chamber wall thicknesses must be sufficient for welding and brazing purposes. Considering the chamber as a cylindrical shell, the chamber wall thickness was computed using Eq. (15) (Sutton, 2005). The chamber wall thickness should be somewhat greater to allow for welding, buckling, and stress concentration. In the current design a safety factor greater than one was used for the calculation of wall thickness. It was determined that the wall thickness of the combustion chamber wall, nozzle, and barrel section are equal (Yang V, 2005).

$$t_{w} = \frac{P_{c} * D_{c}}{2 * S} * safety factor$$
 (15)

In Eq. (15) t_w is the chamber wall thickness, D_c is the chamber diameter, and S is the allowable working

stress of chamber material.

3.1.3 Converging-Diverging Nozzle

The function of the nozzle is to convert the chemical/thermal energy generated in the combustion chamber into kinetic energy. The flow velocity through a nozzle increases to sonic velocity at the throat and then develops supersonically in the diverging section. The nozzle converts the slow moving, high pressure, high temperature gas in the combustion chamber into high velocity gas of lower pressure and temperature (Sutton, 2005). Since thrust or exhaust output of the system is the product of mass and velocity, a very high gas velocity is desirable for the current application. Nozzles, which perform this process, are referred to as de Laval nozzles and consist of a convergent and divergent section, as shown in Fig. 3.4.

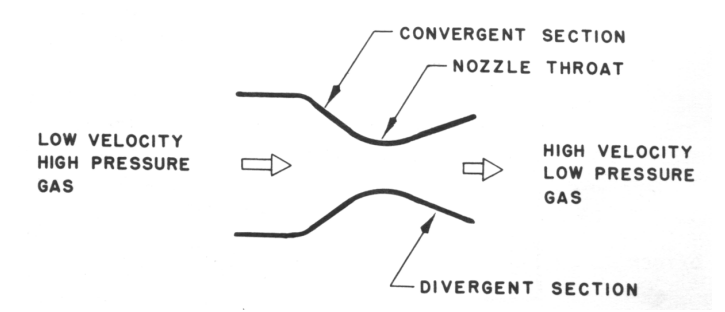


Figure 3.4: Schematic of a converging-diverging nozzle

For design purposes and simplicity it is assumed that flow through a nozzle is an isentropic expansion process, and that both the total temperature and the total pressure remain constant throughout the nozzle (Huzel, 1992). The static pressure at a nozzle throat with sonic flow, where the maximum mass flow per unit area occurs, is defined as the critical pressure (Yang V, 2005). The velocity of sound is equal to the velocity of propagation of a pressure wave within a medium. It is, therefore, impossible for a pressure disturbance downstream of the nozzle throat to influence the flow at the throat or upstream of the throat, provided that this disturbance will not create a higher throat pressure than the critical pressure (Sutton, 2005). It is one of the characteristic features of an attached diverging or de Laval nozzle, however, that sonic velocity in the nozzle throat is maintained even if the backpressure at the nozzle exit is greater than the pressure required at the throat for sonic velocity. As a result, a pressure adjustment must take place between the throat and the nozzle exit. This adjustment may take place through subsonic deceleration, or by way of non-isentropic discontinuities called shock waves, or by a combination of both. The flow area at the end of the divergent section is called the nozzle exit area. For the experimental design the temperature and pressure at the nozzle

throat was calculated from Eqs. (16-17).

$$T_{t} = T_{c} \left[\frac{1}{1 + \frac{\gamma - 1}{2}} \right] \tag{16}$$

$$P_{t} = P_{c} \left[1 + \frac{\gamma - 1}{2} \right]^{\frac{-\gamma}{\gamma - 1}} \tag{17}$$

In these equations T_t is the temperature at nozzle throat, and P_t is the pressure at nozzle throat.

The gas Mach number, velocity, and temperature at the nozzle exit were calculated for the current design from Eqs. (18-20) assuming the perfect gas law expansion expression (Huzel, 1992).

$$M_{a_e} = \sqrt{\frac{2}{\gamma - 1} \left[\left(\frac{P_c}{P_{atm}} \right)^{\frac{\gamma - 1}{\gamma}} - 1 \right]}$$
 (18)

$$V_e = \sqrt{\frac{2 * g * \gamma * R * T_c}{\gamma - 1} \left[1 - \left(\frac{P_{atm}}{P_c}\right)^{\frac{\gamma - 1}{\gamma}} \right]}$$
 (19)

$$T_e = T_t \left(\frac{P_{atm}}{P_t}\right)^{\frac{\gamma - 1}{\gamma}} \tag{20}$$

Where M_{a_e} is the Mach number at nozzle exit, V_e is the gas velocity at nozzle exit, T_e is the gas temperature at nozzle exit, and P_{atm} is the atmospheric pressure.

The nozzle exit cross section area corresponding to the exit Mach number is given by Eq. (21) (Huzel, 1992).

$$A_{e} = \frac{A_{t}}{M_{a_{e}}} \left[\frac{1 + \frac{\gamma - 1}{2} M_{a_{e}}^{2}}{\frac{\gamma + 1}{2}} \right]^{\frac{\gamma + 1}{2(\gamma - 1)}}$$
(21)

Here A_e is the nozzle exit cross section area.

3.1.4 Barrel

Powder particles can either be fed through the oxidizer stream or at some location downstream. The former has several disadvantages including particle overheating, wrongful deposition and deposition inside the configuration; nevertheless, it also solves the question on how to effectively introduce seeding powder into

a HVOF system. In order to decrease the possibility of overheating and introduce particles directly to supersonic flow most gun configurations inject particles into the barrel through a tapping angle. The barrel has been designed as the section where particle injection occurs and products exit the configuration. Although this section is responsible for controlling and optimizing coating properties, there currently exist no quantitative methods to determine the optimal length. Thus a wide range of experimental tests are being done in order to optimize the effectiveness of the system and will be presented in future works.

3.1.5 Cooling Jacket

The average heat transfer rate per unit area in the combustion chamber during the oxy-combustion process is about 6 MW/m² (Sutton, 2005). It is therefore necessary to implement a cooling system on the combustion chamber to avoid material failure (Yang V, 2005). In total, the largest part of the heat transferred from the hot chamber gases to the chamber walls is attributed to convection, with heat transferred by conduction and radiation comprising approximately 25% of the total heat transfer (Yang V, 2005).

The cooling jacket consists of an inner and outer wall. The combustion chamber forms the inner wall with another concentric but larger cylinder forming the outer wall. The space between the walls serves as the coolant passage. The injector under normal operation is self-cooled by the incoming flow of propellants. The combustion chamber, nozzle, and barrel however require additional cooling for longer duration periods of operation. Of particular importance is the nozzle throat region which because of the smaller geometry is exposed to a very high heat flux (Yang V, 2005). To cool this section of the system an advanced ethylene glycol formula, Dynalene (HC-10), is used because of its ability to absorb heat (Dynalene, n.d.), Table 2.

Table 3.1: Properties of Dynalene (HC-10)

Properties	Units of measure
Temperature range	263 to 491 K
Specific Heat capacity	3.28 kJ/kg.K
Density	1200 kg/m^3

The total heat transferred from the gun to the coolant can be calculated from Eqs. (22-24) assuming the area of the nozzle cone up to the throat to be 10% of the chamber surface area (Huzel, 1992).

$$Q_{total} = q * A_{total} (22)$$

$$A_{total} = \pi * L_c(D_c + 2 * t_w) + area of nozzle cone + \pi * L_{barrel}(D_{barrel} + 2 * t_w)$$
 (23)

$$A_{total} \cong 1.1 * \pi * L_c(D_c + 2 * t_w) + \pi * L_{barrel}(D_{barrel} + 2 * t_w)$$
(24)

Where Q_{total} is the total heat transferred, q is the average heat transfer rate per unit area of a HVOF thermal spray gun, assumed to be 6 MW/m² (Sutton, 2005), A_{total} is the total heat transfer area, L_{barrel} is the barrel length, and D_{barrel} is the barrel diameter.

The coolant mass flow rate can be calculated by assuming a desired temperature rise of the coolant from Eq. (25):

$$m_{coolant}^{\circ} = \frac{Q_{total}}{C_{p_{coolant}} * (T_o - T_i)_{coolant}}$$
 (25)

Where $m_{coolant}^{\circ}$ is the coolant mass flow rate, $C_{p_{coolant}}$ is the specific heat of coolant, T_{o} is the temperature of coolant leaving jacket, and T_{i} is the temperature of coolant entering jacket.

The annular flow passage between the combustion chamber wall and the outer jacket must be sized so that the flow velocity of the coolant is at least 10 m/s (Yang V, 2005). The flow passage dimensions can be calculated from Eqs. (26-28) (Huzel, 1992).

$$A_{cooling\ jacket} = \frac{m_{coolant}^{\circ}}{\rho_{coolant} * V_{coolant}}$$
 (26)

$$A_{cooling\ jacket} = \frac{\pi}{4} (D_o^2 - D_i^2) \tag{27}$$

$$D_i = D_c + 2 * t_w \tag{28}$$

Where $A_{cooling\ jacket}$ is the cooling jacket cross section area, $\rho_{coolant}$ is the coolant density, $V_{coolant}$ is the coolant average flow velocity, D_i is cooling jacket inner surface diameter, and D_o is cooling jacket outer surface diameter.

3.2 Experimental Setup

Figure 3.5 shows a schematic of utilized test rig. The test rig consists of four primary lines: oxidizer, fuel, carrier gas, and coolant along with two secondary lines: fuel purging and exhaust dilution. Each line consists of a combination of safety and measuring devices.

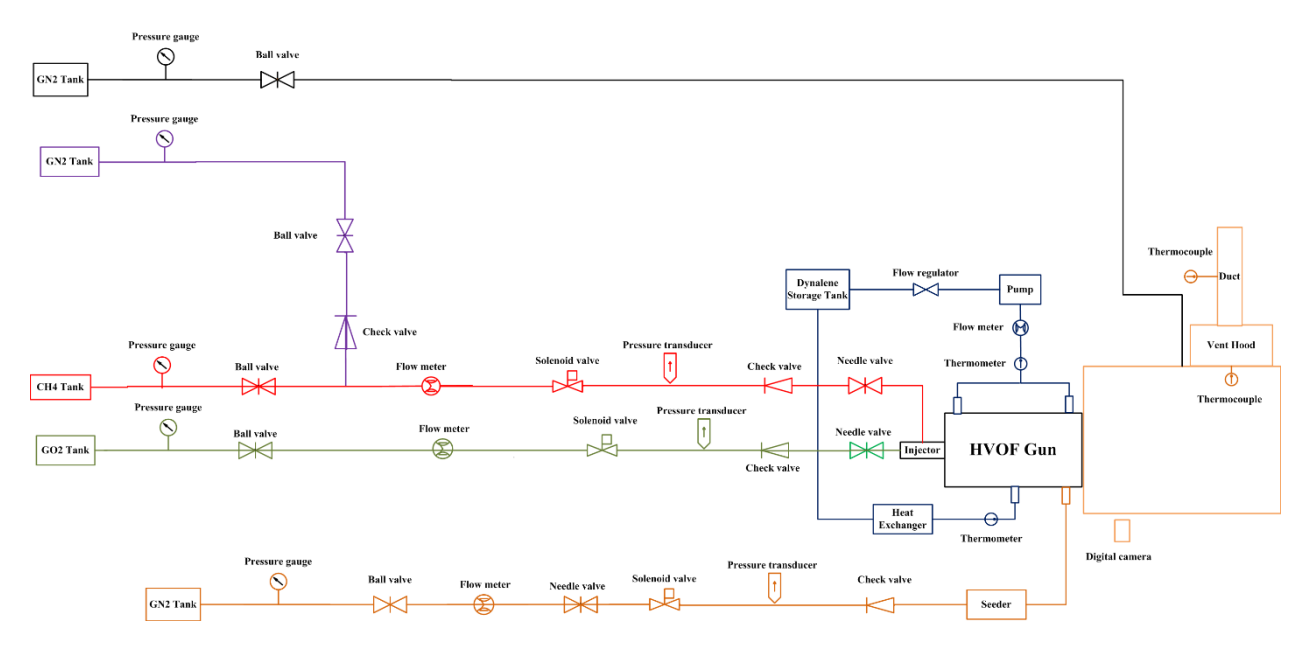


Figure 3.5: Schematic of test rig for gas-fueled HVOF thermal spray system

The coolant line starts with a 400 L storage tank from NORTHERN TOOL (part # 3490300), Fig. 3.6, followed by a 1.1 kW centrifugal pump from AMT (part # 4298-98), Fig. 3.7, to circulate the coolant into 25.4 mm stainless steel tube. A liquid turbine flow meter from OMEGA (part # FTB-1423), Fig. 3.8, is used in this line. After the coolant is introduced to the gun, the exit line goes to air to liquid heat exchanger from THERMATRON ENGINEERING (part # 728MP03A01), Fig. 3.9, that is equipped with eight 24-VDC axial fans from SPAL AUTOMOTIVE (part # VA89-BBL305-94A), Fig. 3.10, to enhance convection rate. Then the loop is closed by delivering the heat exchanger output back to the storage tank. There are two bimetal thermometers from TEL-TRU (part # 4210-02-79), Fig. 3.11, right before and after the cooling jacket to measure the inlet and exit coolant temperatures. Additionally, there are six J-type thermocouples from OMEGA (part # XC-20-J-12), Fig. 3.12, attached to the feed through connection on top of the cooling jacket to observe the temperature fluctuations on the outer surface of the gun.



Figure 3.6: Storage tank



Figure 3.7: Centrifugal pump



Figure 3.8: Liquid turbine flow meter

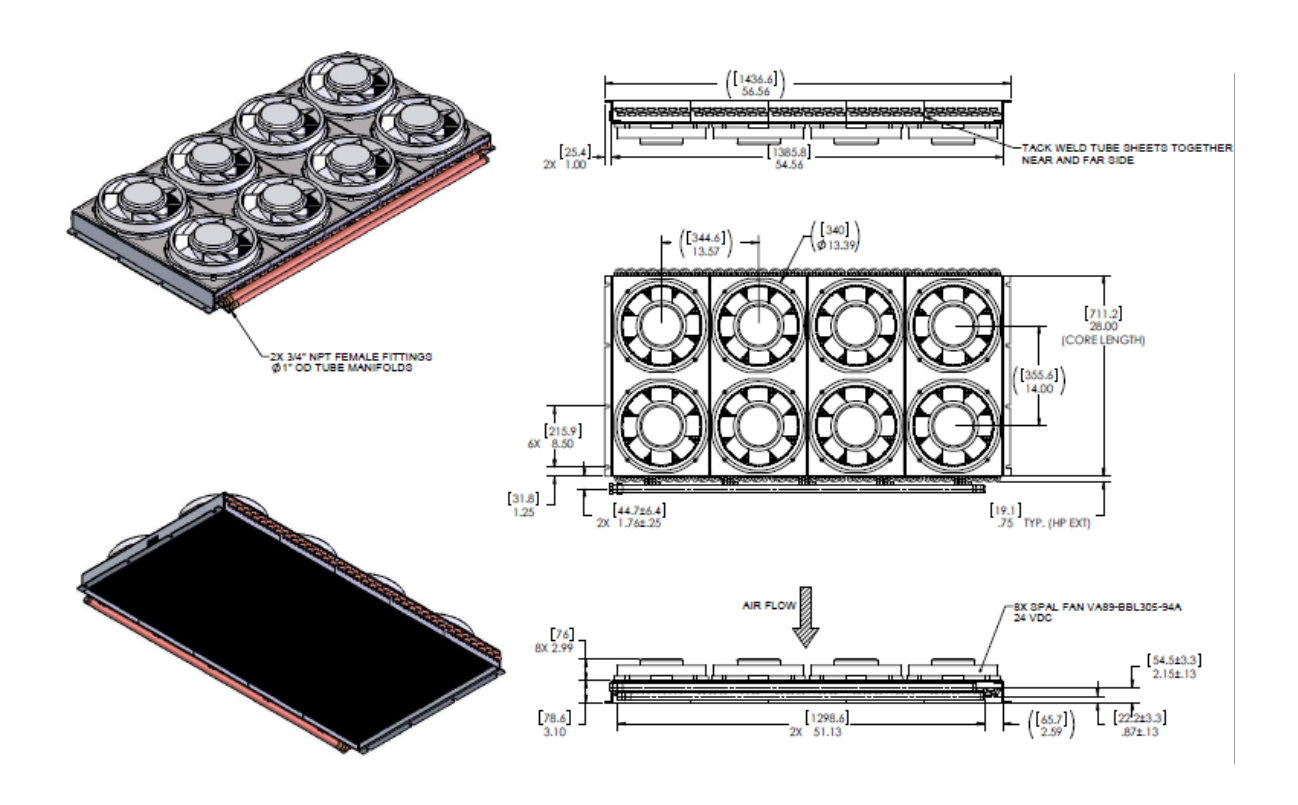


Figure 3.9: Air to liquid heat exchanger



Figure 3.10: Axial fan



Figure 3.11: Bimetal thermometers



Figure 3.12: J-type thermocouple

The carrier gas for coating particles line starts with an ultra-high purity nitrogen gas cylinder followed by a solenoid valve from JEFFERSON (part # 1390BN4T), Fig. 3.13, then a thermal gas flow meter from OMEGA (part # FMA1843), Fig. 3.14. The carrier gas is introduced to the seeder through a 12.7 mm stainless steel tube to carry the coating particles to be injected in the barrel section, see Fig. 3.15.



Figure 3.13: Nitrogen solenoid valve



Figure 3.14: Thermal gas flow meter

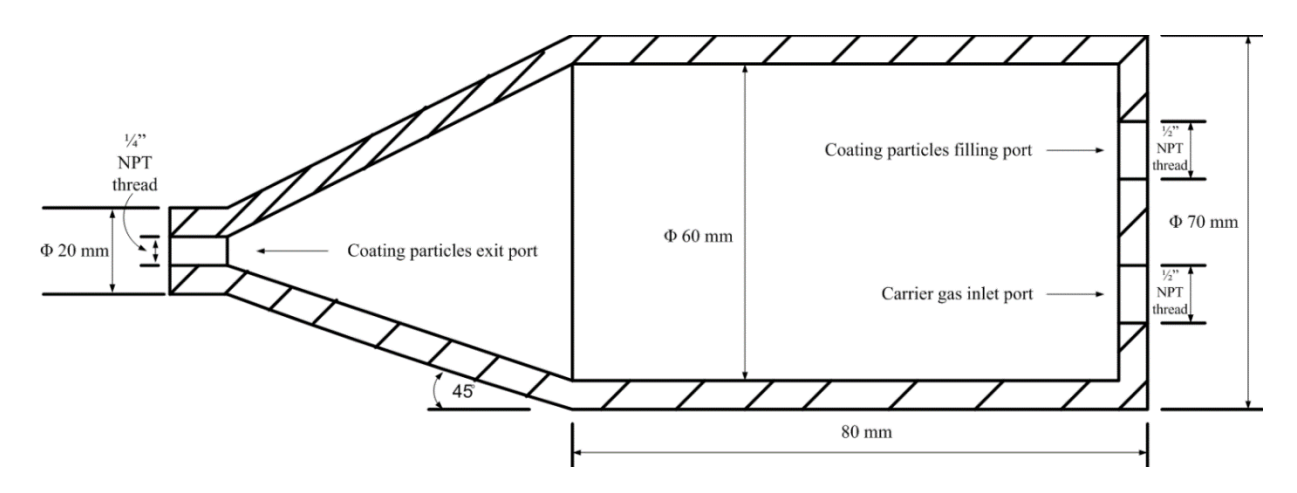


Figure 3.15: Schematic of coating particles seeder

The oxidizer line starts with a gaseous oxygen cylinder followed by a solenoid valve from JEFFERSON (part # 1342SN06T), Fig. 3.16, then a gas turbine flow meter from OMEGA (part # FTB-935), Fig. 3.17, and finally the gas is introduced to the injector through a 19 mm stainless steel tube. The gas fuel line which

starts with a gaseous methane cylinder followed by solenoid valve from JEFFERSON (part # 1390SA4T), Fig. 3.18, and then a thermal gas flow meter from OMEGA (part # FMA1844), Fig. 3.19. Methane is introduced to the injector in a 12.7 mm stainless steel tube. Oxidizer, fuel, and carrier gas lines are equipped with three pressure transducers from OMEGA (part # PX302-500GV), Fig. 3.20, one in each line, to monitor pressure fluctuations. The combustion chamber is equipped with a spark plug ignition system powered by 25k VDC generated by a transformer from ULTRAVOLT (part # 25A12-P4), Fig. 3.21, that requires 12 VDC generated by a quad output DC Power Supply from EXTECH INSTRUMENTS (part # 382270), Fig. 3.22.



Figure 3.16: Oxygen solenoid valve



Figure 3.17: Gas turbine flow meter



Figure 3.18: Methane solenoid valve



Figure 3.19: Thermal gas flow meter



Figure 3.20: Pressure transducer



Figure 3.21: DC transformer



Figure 3.22: DC Power Supply

All testing and recording procedures are conducted using LabView software and DAQ card from NATIONAL INSTRUMENTS (part # NI-PCI-6229-779068-01), Fig. 3.23. A program was written specifically for these oxygen/methane tests, Fig. 3.24. The program consists of two toggle switches. The first allows the user to switch between manual and automatic valve control modes, and the second tells the program whether or not to record data that is turned on manually during testing. Manual mode is used to

control the lines individually for cold flow tests, general maintenance, or troubleshooting. Automatic mode is used to control the valves opening and closing sequences during tests to ensure consistent testing parameters. Automatic mode is also used to activate the ignition system in such way that permits the fuel and oxidizer to burn in the combustion chamber and to start the temperature acquisition automatically from the thermocouples.



Figure 3.23: DAQ card

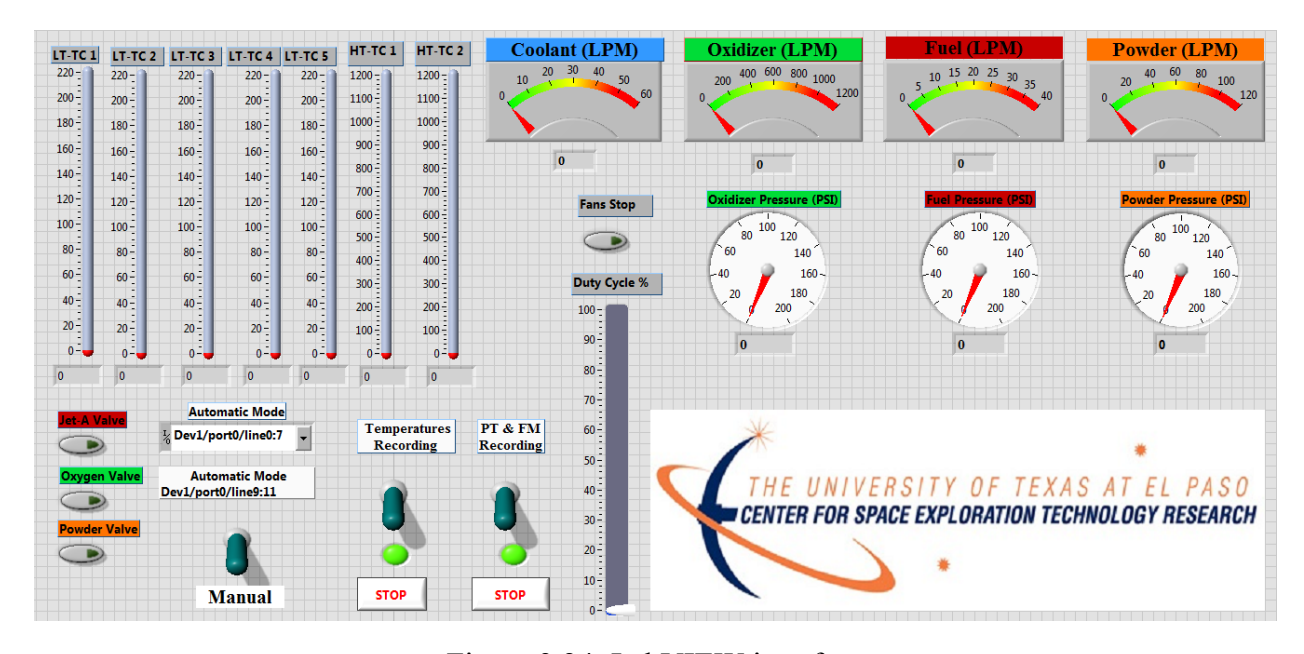


Figure 3.24: LabVIEW interface

A simple schematic of all electronic lines is shown in Fig. 3.25. The data acquisition system (DAQ) provides

an output in the form of a duty cycle to activate fan rotation frequency for the cooling line; the DAQ also provides a signal to the solenoid valves through a relay, which in turn indicates their ON/OFF sequence. The DAQ receives data from the flow meters and pressure transducers in the form of voltage and converts it to an actual reading; since the output of the pressure transducers is measured in mV, programmable voltage converters must always be included in the wiring setup. Low and high temperature thermocouple data is also received and interpreted by the DAQ. The cooling pump and heat exchanger fans are wired to the laboratory grid in terms of power supplement. The separate DC power supply provides voltage and current to the transformer box for the igniter as well as to all employed solenoid valves. An emergency stop button is wired in all supplied configurations to prevent further combustion in case of an emergency.

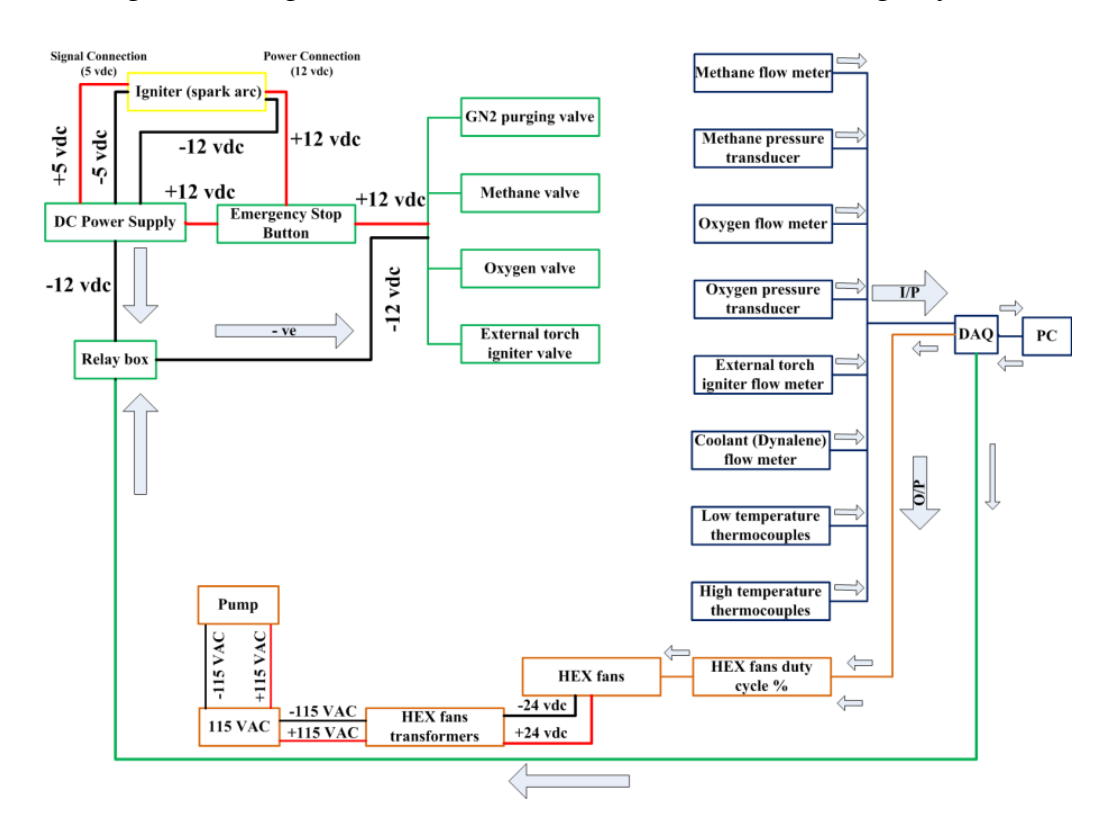


Figure 3.25: Electrical device diagram

A venting enclosure (spray booth) has been built as a confining volume to prevent plume expansion and possible damage to nearby laboratory instrumentation, Fig. 3.26. All walls save the lateral geometries are composed of stainless steel. Lateral walls are covered in fire proof blankets rated up to 1500 K in short term exposure. Recently, two internal deflectors were added to the design to prevent damage to vent hood equipment. A stainless steel kitchen range hood has been added to the top of this enclosure to properly draw out combustion products into the laboratory main suction vent. The combustion process is seen orthogonally through the left side of the setup exit; at this location a small piece of the fire blanket has been lifted to allow

for sufficient viewing space.

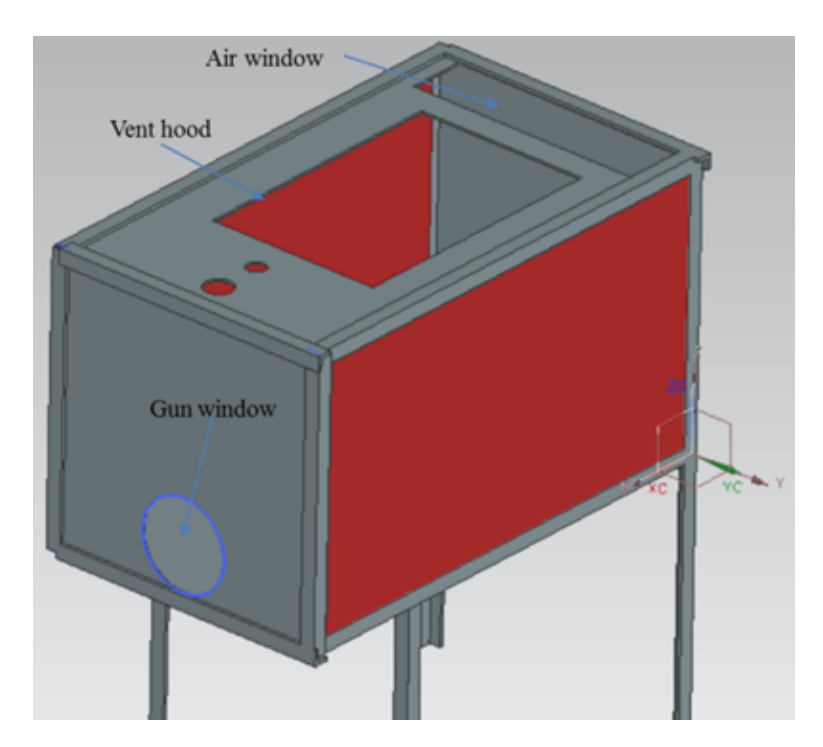


Figure 3.26: Schematic of utilized spray booth

3.3 Safety Considerations

A fast-acting, automatic control of solenoid valves is essential in the event of an emergency. Emergency switches must be present both in the interface as well as in a physical location; this is due to the possibility of software malfunction during a test, which could cause significant damage to the setup components. A manual button has been implemented in the operation control center, and it is readily available. At least one person during a test must take control of the switch in order to halt combustion at will. A fire extinguisher is to be on-hand at all times in the event of an uncontrolled firing. Off-setup, undesired combustion must be continuously prevented; an unburned hydrocarbon-monitoring device must be used before, after and inbetween runs. In the case of setup malfunctioning or overpressure, explosion-proof Kevlar walls are placed around the experimental area to protect all operators present. To prevent these events, continuous purging of the lines has been implemented into the test procedure; additionally, wait times have been established for venting possibly hazardous gases.

To reduce the possibility of an unplanned fire the gun must be examined and cleaned in between runs; examination of the device is conducted using a boroscope or small maneuverable camera. Although most experimentation is performed under a manual mode, redlines must be established in automatic operation.

Redlines are defined as overall safety limits; once the system detects a breaching of established boundaries, all operations must be halted. An oxygen monitor is employed to detect abnormal levels in the atmosphere; if a leak exists for inert gases or an enriched oxygen atmosphere is detected a signal will be transmitted. Due to the fact that noise levels for HVOF systems can range anywhere from 125 to 133 dba, all those present are required to wear adequate ear protection. As a final note on safety, no one except test operators is allowed to be in the laboratory during a session.

Chapter 4: Computational Fluid Dynamics (CFD) Study

4.1 Introduction

In this research, a computational fluid dynamic (CFD) model has been developed to predict gas dynamic behavior in a high-velocity oxygen-fuel (HVOF) thermal spray gun. The model assumes that oxygen (O₂) and methane (CH₄) are burnt in a combustion chamber linked to a parallel-sided converging-diverging nozzle. The CFD analysis is applied to investigate axisymmetric, steady-state, turbulent, compressible, chemically reacting, subsonic and supersonic flow within the gun and the external domain. Results describe the general gas dynamic features of HVOF spraying and give a detailed discussion of the numerical predictions of a computational fluid dynamic (CFD) analysis. The gas axial velocity, axial temperature, static pressure, and Mach number distributions are presented for various locations inside and outside the gun. Previous research (Gourlaouen, 1998) (W.C. Lih, 2000) (M. Hasan, 2008) proved that the most sensitive parameters affecting the HVOF thermal spraying process are the equivalence ratio and total gas flow rate. Hence, gas dynamic behavior along the centerline of the gun depends on both total gas flow rate and equivalence ratio.

4.2 Methodology

The current study is focused on the combustion process and subsequent gas flow pattern, while particle dynamics and gas—particle interactions are not included. The computational domain used in the present simulation is shown in Fig. 4.1. Since the gun geometry is symmetrical about its axis, a two-dimensional (2-D) axisymmetric grid is used to simulate the gas phase flow behavior. Figure 4.2 shows the used mesh cell volume. The used grid is finer and denser in the regions where large gradients of flow properties exist, and gradually changes to become coarser in the regions where small gradients of flow properties are expected. This fine mesh size will be able to provide good spatial resolution for the distribution of most variables within the combustion chamber, convergent-divergent nozzle, barrel, and external domain.

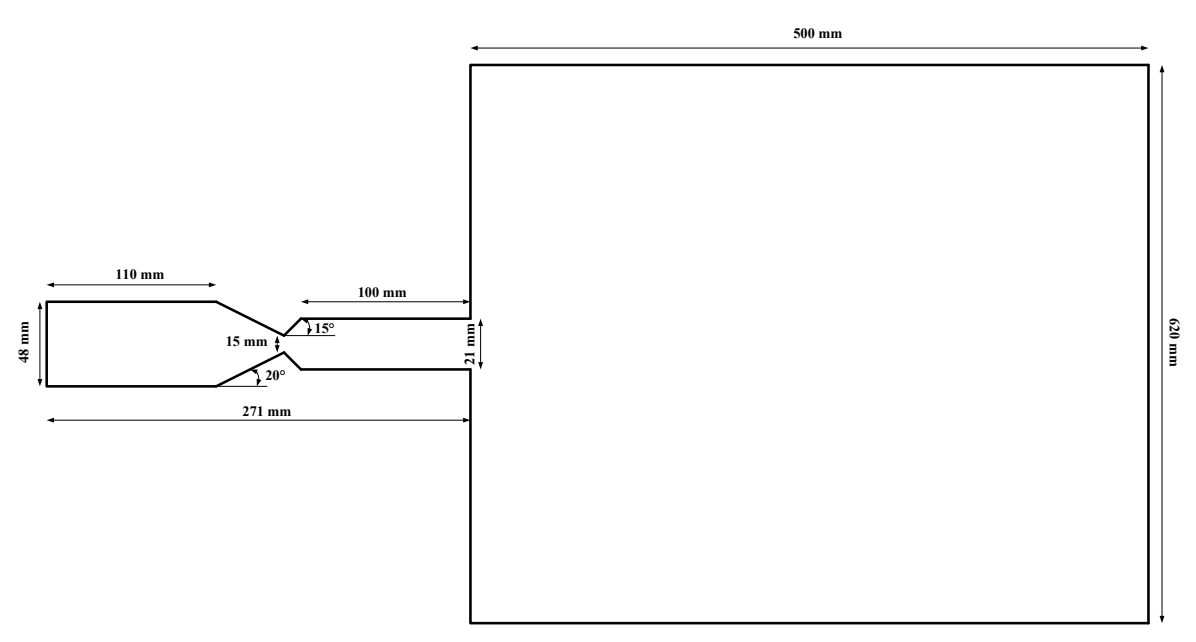


Figure 4.1: Schematic of gun geometry and computational domain with dimensions shown

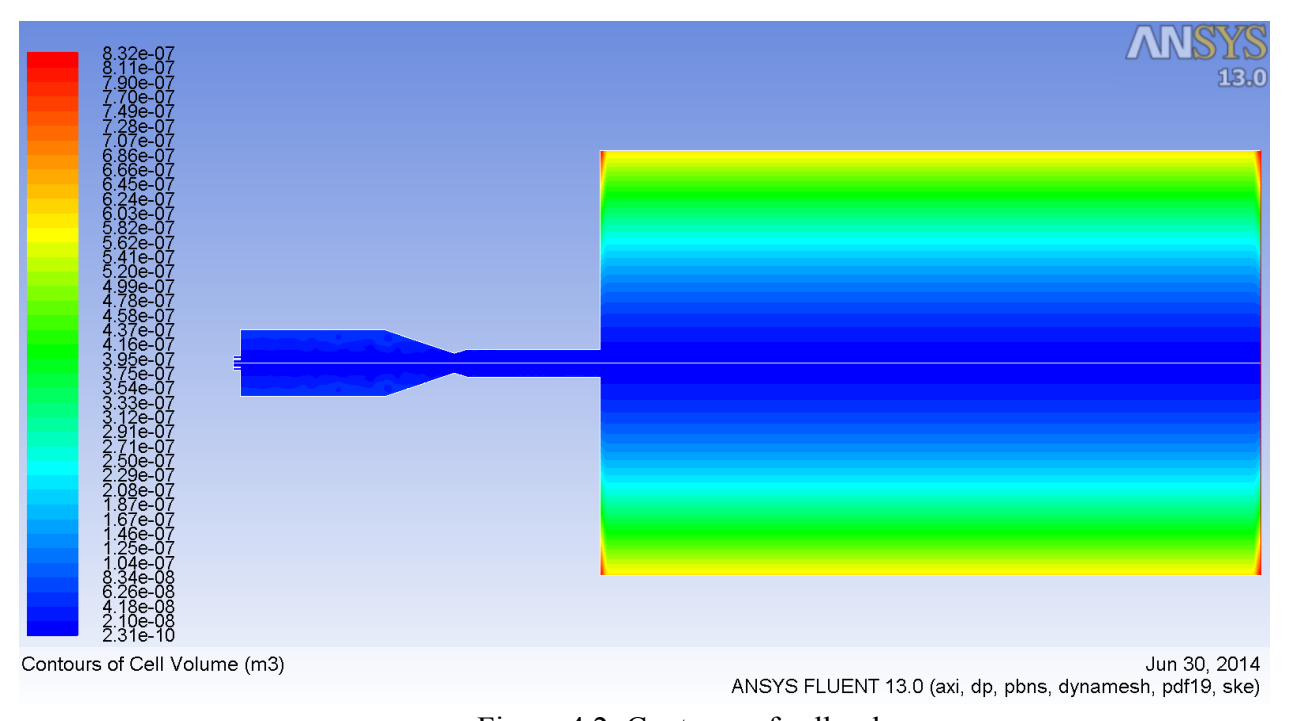


Figure 4.2: Contours of cell volume

A commercial CFD code, Fluent 6.3, is used to perform numerical simulations of the fluid flow in HVOF thermal spray system by solving the conservation equations of mass, momentum, energy and species. A two-equation, realizable $k - \varepsilon$ turbulence model is employed for the turbulent flow field. In comparison with the standard $k - \varepsilon$ model, the realizable $k - \varepsilon$ model contains a new formulation of the turbulent viscosity where the dynamic viscosity coefficient is no longer constant.

4.3 Modeling Parameters

Table 4.1 presents a summary of working conditions for the investigated cases in this study. Three different oxygen mass flow rates were considered, namely: A (20 g/s), B (25 g/s), and C (30 g/s). At each of these flows three different equivalence ratios were investigated: 0.9 (lean fuel mixture), 1.0 (stoichiometric fuel mixture), and 1.1 (rich fuel mixture). Equivalence ratio for this study is defined as the fuel to oxygen ratio divided by its stoichiometric value. The inlet temperatures of oxygen and fuel are considered to be uniform at 300 K. Axisymmetric boundary conditions are applied along the central axis of the combustion chamber. The interior surfaces of the gun are protected by the coolant from outside and defined as non-slip wall from inside with a constant temperature of 350 K. The gas exhausts from the gun to air, where external pressure boundary is applied to the ambient temperature of 300 K and atmospheric pressure of 1.013×10⁵ Pa.

Table 4.1: Summary of working conditions

	Oxygen mass flow rate, g/s	Fuel mass flow rate, g/s			
Case		At equivalence	At equivalence	At equivalence	
		ratio of 0.9	ratio of 1.0	ratio of 1.1	
A	20	4.5	5	5.6	
В	25	5.6	6.3	6.9	
C	30	6.7	7.5	8.3	

The numerical method used in this study is a coupled solution algorithm with a finite volume-based technique. The coupled solution was chosen, due to the advantage over the alternative method of segregated coupling between the velocities and pressure. This can help to avoid convergence problems and oscillations in pressure and velocity fields. This technique consists of an integration of the governing equations of mass, momentum, species, energy and turbulence on the individual cells within the computational domain to construct algebraic equations for each unknown dependent variable. The pressure and velocity are coupled using the COUPLED (implicit method for pressure linked equations) algorithm which uses a guess-and-correct procedure for the calculation of pressure on the staggered grid arrangement. It is more economical and stable compared to the other algorithms. The second order upwind scheme is employed for the discretization of the model equations as it is always bounded and provides stability for the pressure-correction equation. The CFD simulation convergence is judged upon the residuals of all governing equations.

4.4 Results & Discussion

A number of numerical simulations were performed to study the gas dynamic behavior in a high-velocity oxygen-fuel (HVOF) thermal spray gun in which non-premixed oxygen and methane were reacted in a combustion chamber. In considering differences among simulations, for the range of total gas flows and equivalence ratios examined results were plotted as centerline flow field variable versus axial distance. In this HVOF gun system, key process variables are total gas flow rate and equivalence ratio.

Figure 4.3 shows the variation of centerline gas static pressure with axial distance. The pressure remains high within the combustion chamber, decreases sharply in the convergent nozzle, reaches sub-atmospheric level at the nozzle throat and then increases slightly to reach near atmospheric level in the barrel. Maximum gas pressures inside the chamber are achieved at rich equivalence ratios with constant flow rate, Case B, seen in Fig. 4.3a. At a rich equivalence ratio of 1.1, a mean combustion chamber pressure of 2.85×10^5 Pa is achieved, Fig. 4.3a, while a corresponding value of 1.95×10^5 Pa is detected at a lean equivalence ratio of 0.9.

Similarly, maximum gas pressures inside the chamber are achieved at the highest total flow rate, Case C, at a constant equivalence ratio of 1.1, Fig. 4.3b. In Case C, a mean combustion chamber pressure of 3.35×10^5 Pa is achieved, Fig. 4.3b, while a corresponding value of 2.6×10^5 Pa is detected in Case A. Consequently, increasing the total gas flow rate and/or equivalence ratio results in increasing the gas pressure inside the combustion chamber as well as the convergent nozzle. Since the Mach number and gas velocity depend on combustion chamber pressure, high combustion chamber pressure results in a high Mach number and high gas velocity at the throat and the divergent nozzle. This is due to chamber pressure being responsible for promoting gas turbulence and choking phenomena.

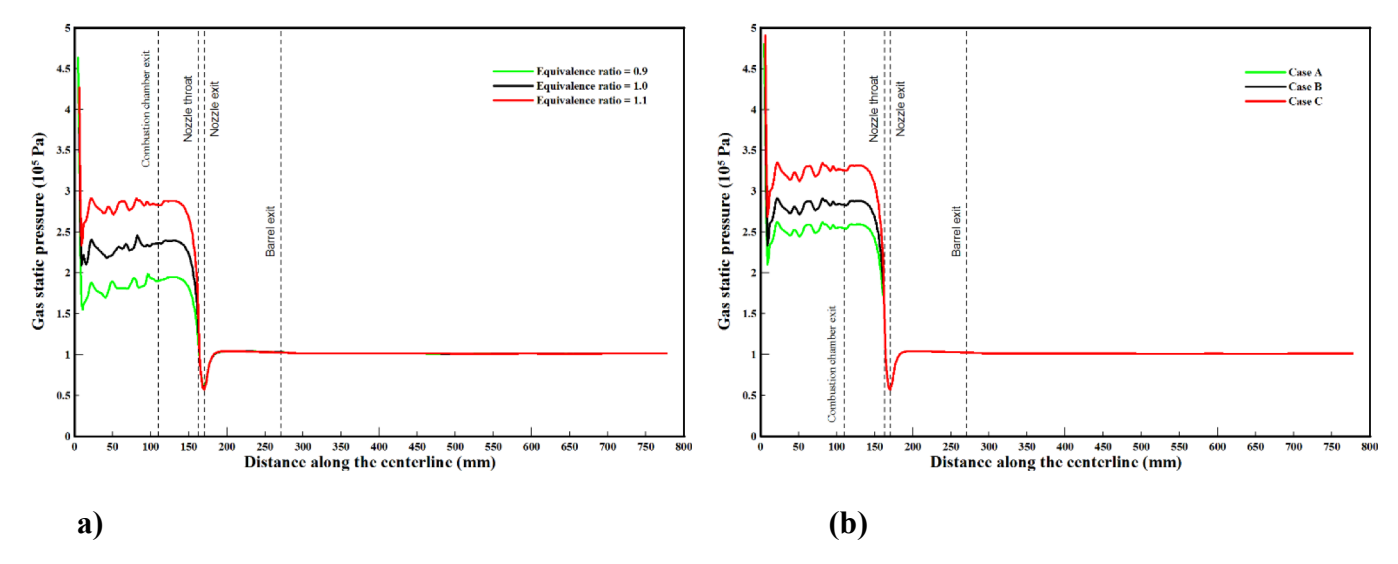


Figure 4.3: Variation of gas static pressure with distance along the centerline of the computational domain, a) Case B at three different equivalence ratios 0.9, 1.0, and 1.1, b) equivalence ratio of 1.1 at three different cases A, B, and C

The flow transition from subsonic to supersonic conditions through the convergent–divergent nozzle is shown by the Mach number plot in Fig. 4.4. The subsonic flow is accelerated in the convergent region reaching a sonic state at the throat and further accelerated to a supersonic condition in the divergent region. Upon entering the barrel the supersonic flow further expands through a series of shock waves and becomes stabilized. It needs to be pointed out that the shocks encountered in the divergent nozzle give rise to energy loss when the thermal energy is converted to kinetic energy in the gas phase and thus undesirable. The overall trend shows the Mach number to increase sharply as it converges into the nozzle but decreases only marginally within the parallel-sided region due to the shock wave effect. The maximum Mach number and axial gas velocity are achieved at a rich equivalence ratio with constant flow rate Case B, Figs. 4.4a and 4.5a. In addition, Fig. 4.6 proves the previous conclusion using Case C at three different equivalence ratios. At rich equivalence ratio of 1.1, Mach number of 1.95, and axial gas velocity of 2150 m/s are achieved as can be seen in Figs. 4.4a and 4.5a. This corresponds to values of 1.6 and 1800 m/s for Mach number and axial gas velocity, respectively, are detected at lean equivalence ratio of 0.9.

Similarly, the maximum Mach number and axial velocity are achieved at the highest total flow rate Case C at a constant rich equivalence ratio of 1.1, Fig. 4.4b and 4.5b. In Case C, a Mach number of 2.1 and axial gas velocity of 2450 m/s are achieved, Figs. 4.4b and 4.5b, while corresponding values of 1.7 and 1850 m/s for Mach number and axial gas velocity, respectively, are detected in Case A. Consequently, increasing the total gas flow rate and/or equivalence ratio results in increasing the Mach number/axial velocity at nozzle throat as well as the barrel section exit. It is clear that gas velocity decay in the free jet due to entrainment

of air.

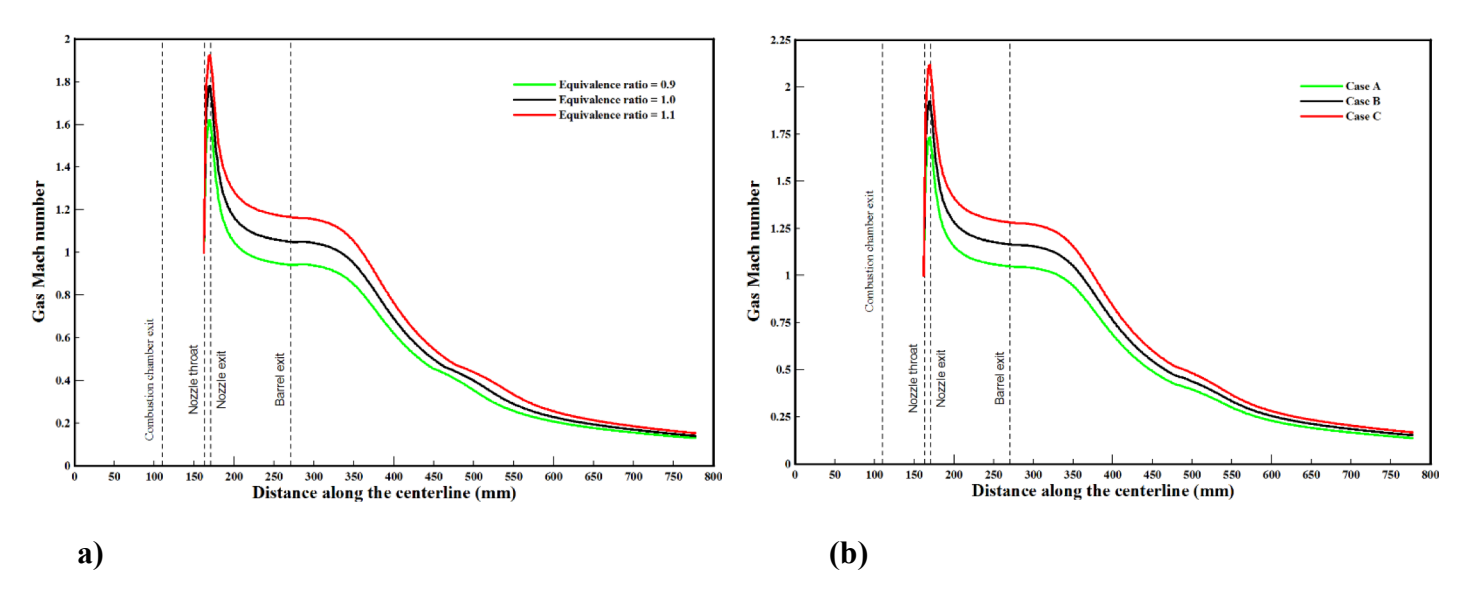


Figure 4.4: Variation of gas Mach number with distance along the centerline of the computational domain, a) Case B at three different equivalence ratios 0.9, 1.0, and 1.1, b) equivalence ratio of 1.1 at three different cases A, B, and C

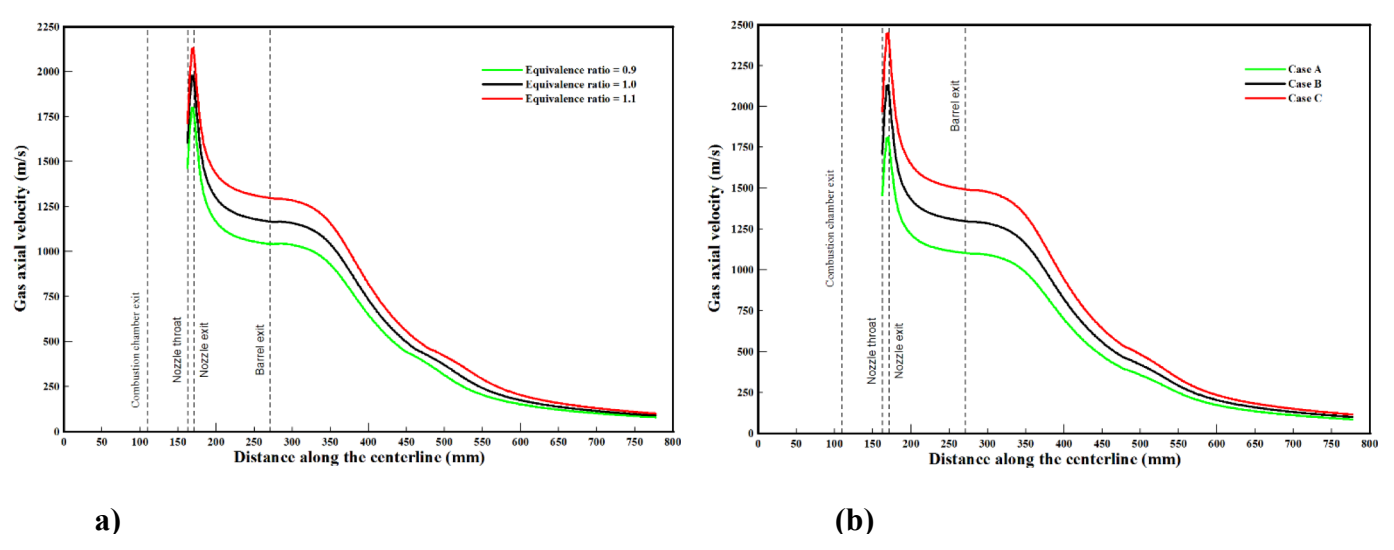


Figure 4.5: Variation of gas axial velocity with distance along the centerline of the computational domain, a) Case B at three different equivalence ratios 0.9, 1.0, and 1.1, b) equivalence ratio of 1.1 at three different cases A, B, and C

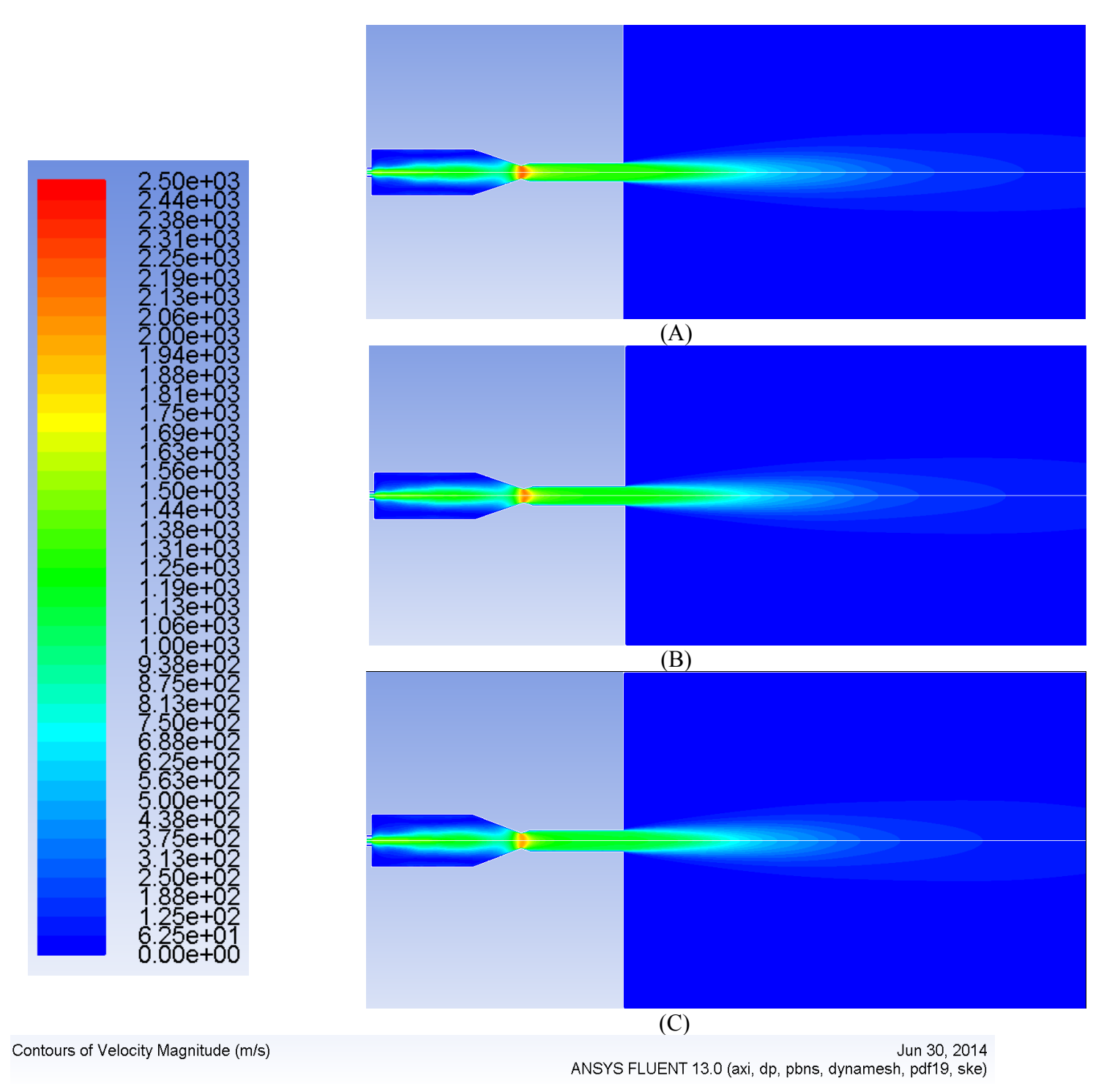


Figure 4.6: Contours of axial velocity in Case C, a) at rich equivalence ratio of 1.1, b) at stoichiometric equivalence ratio of 1.0, c) at lean equivalence ratio of 0.9

Figure 4.7 shows the variation of centerline gas axial temperature with axial distance. The gas temperature starts at an atmospheric value near the injector face followed by a significant increase in the last part of the combustion chamber. Temperature continues increasing inside the convergent-divergent nozzle and reaches its maximum value at nozzle throat and inside the barrel. Maximum gas temperature is achieved at the richest

equivalence ratio with constant flow rate Case B, Fig. 4.7a. In addition, Fig. 4.8 proves the previous conclusion using Case C at three different equivalence ratios. At a rich equivalence ratio of 1.1, a maximum gas temperature of 2950 K is achieved, Fig. 4.7a, while a corresponding value of 2750 K is detected at lean equivalence ratio of 0.9.

Similarly, maximum gas temperature is achieved at the highest total flow rate Case C at constant equivalence ratio of 1.1, see Fig. 4.7b. In Case C, a maximum gas temperature of 3150 K is achieved, see Fig. 4.7b, while a corresponding value of 2800 K is detected in Case A. Consequently, increasing the flow rate and/or equivalence ratio results in increasing the gas temperature in the barrel section. It is clear that gas temperature decay in the free jet due to the entrainment of air.

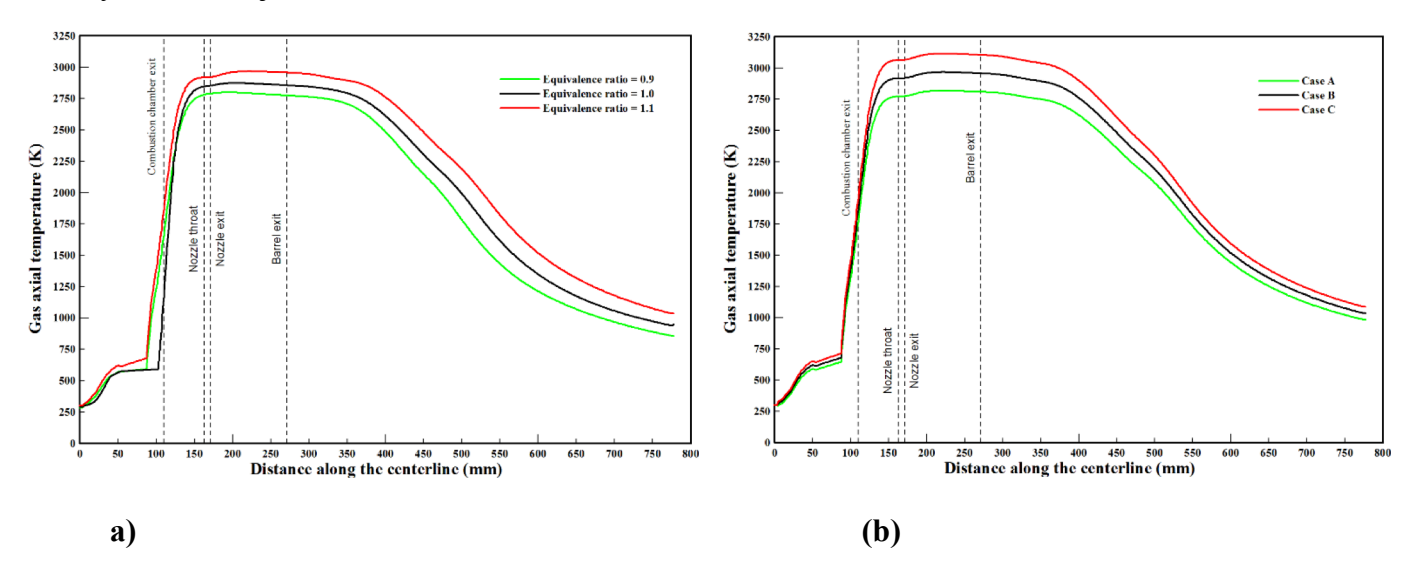


Figure 4.7: Variation of gas axial temperature with distance along the centerline of the computational domain, a) Case B at three different equivalence ratios 0.9, 1.0, and 1.1, b) equivalence ratio of 1.1 at three different Cases A, B, and C

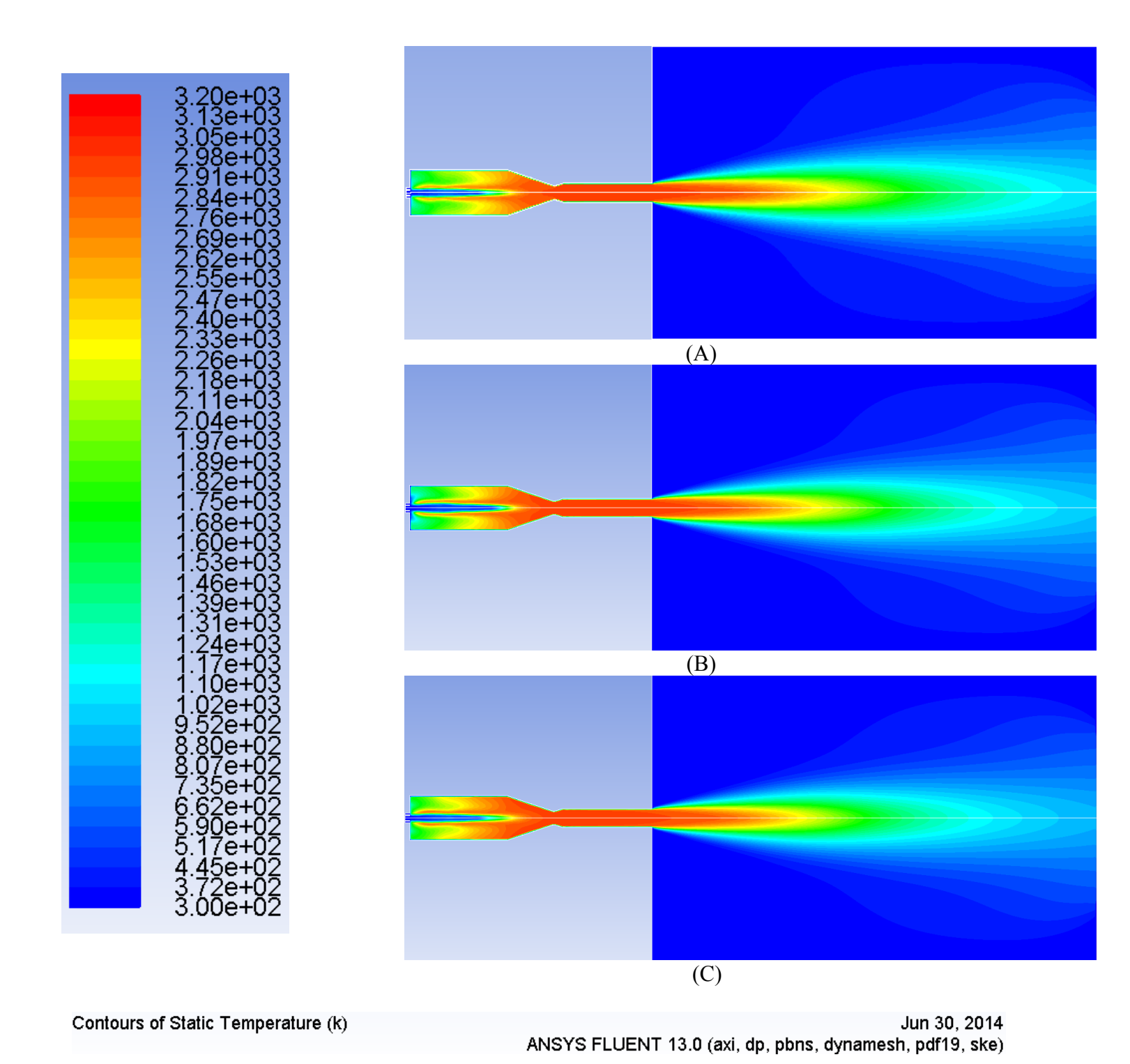


Figure 4.8: Contours of axial temperature in Case C, a) at rich equivalence ratio of 1.1, b) at stoichiometric equivalence ratio of 1.0, c) at lean equivalence ratio of 0.9

4.5 Summary & Conclusions

This study describes the gas dynamics features that exist inside and outside a high-velocity oxygen-fuel (HVOF) thermal spray gun in which non-premixed oxygen and methane are burned in a combustion chamber linked to a parallel-sided convergent-divergent nozzle where the hot gas is accelerated. A commercial CFD code, Fluent 6.3, is used to perform numerical simulations of the fluid flow in HVOF thermal system by solving the conservation equations of mass, momentum, energy and species. The gas axial velocity, axial temperature, static pressure, and Mach number distributions are presented for various locations inside and outside the HVOF system. The two-dimensional numerical simulations show large variations in gas axial velocity, Mach number, and axial temperature both inside and outside the gun due to flow features such as mixing layers, shock waves, and expansion waves.

The results reported in this research illustrate that the numerical simulation can be one of the most powerful and beneficial tools for the HVOF system design, optimization and performance analysis. The results indicate that the most sensitive parameters that affect the behavior of the system both total gas flow rate and equivalence ratio. The axial gas velocity and axial gas temperature depend on both flow rate and equivalence ratio; the highest velocity/temperature is achieved at the highest flow rate and/or rich equivalence ratio.

The numerical simulations show that the gas axial velocity, axial temperature, static pressure and Mach number distribution depend on both flow rate and equivalence ratio. The maximum velocity, temperature, and pressure are achieved at the highest flow rate and/or richest equivalence ratio. In addition, the results reported in this research illustrate that the numerical simulation can be one of the most powerful and beneficial tools for the HVOF thermal spray system design, optimization and performance analysis.

Chapter 5: Results and Discussions

5.1. Gas-Fueled HVOF Thermal Spray Gun Design

Table 5.1 summarizes all operating conditions and geometric parameters used in the design of the current gas-fueled HVOF thermal spray gun. The present HVOF thermal spray gun was designed to generate gas with velocity up to 1690 m/s, Mach number up to 1.9, and temperature up to 2475 K. The combustion chamber pressure of 700 kPa was selected as a typical condition representative in most commercial HVOF thermal spray guns. After system assembly, component testing was done to ensure the functionality of the system.

Table 5.1: Summary of operating conditions and geometric parameters

Inputs		Outputs		
Oxidizer	Oxygen	Oxidizer mass flow rate, m _o	0.062 kg/s	
Fuel	Methane	Fuel mass flow rate, m _f	0.018 kg/s	
Oxygen to fuel ratio, $^{0}/_{F}$	3.5	Total mass flow rate, m _t	0.080 kg/s	
Ratio of gas specific heats, γ	1.2	Gun wall thickness, t_w	5 mm	
Gas molecular weight, M_{wt}	26.7 g/mol	Combustion chamber volume, V_c	$2.6*10^{-4} \text{ m}^3$	
Oxidizer density at P_{atm} , $\rho_{o_{atm}}$	1.33 kg/m^3	Chamber characteristic length, L*	1.49 m	
Fuel density at P_{atm} , $\rho_{f_{atm}}$	0.69 kg/m^3	Gas temperature at nozzle exit, T_e	2475 K	
Discharge coefficient, C_d	0.75	Gas velocity at nozzle exit, V_e	1690 m/s	
Number of injector orifices, N	3	Gas Mach number at nozzle exit, $M_{a_{\rho}}$	1.9	
Combustion chamber pressure, P_c	700 kPa	Converging nozzle inlet diameter	50 mm	
Combustion chamber adiabatic flame temperature, T_c	3350 K	Diverging nozzle exit diameter	21 mm	
Allowable working stress of stainless steel (SS-316), <i>S</i>	10 MPa	Barrel inlet/exit diameter, D _{barrel}	21 mm	
Wall thickness safety factor	3	Cooling jacket inner diameter	85 mm	
Combustion chamber length, L_c	110 mm	Cooling jacket outer diameter	100 mm	
Combustion chamber diameter, D_c	50 mm	Cooling jacket wall thickness	7.5 mm	
Convergent nozzle half-angel, β	20°	Total heat transfer area, A_{total}	0.033 m^2	
Divergent nozzle half-angel, α	1 <i>5</i> °	Coolant inlet temperature, T_i	290 K	
Throat diameter, D_t	15 mm	Coolant exit temperature, T_o	440 K	
Barrel length, L_{barrel}	100 mm	Coolant mass flow rate, $m_{coolant}^{\circ}$	0.4 kg/s	
		Total heat transfer rate, Q_{total}	195.3 kW	

All instrumentation in the HVOF thermal spray system was tested for functionality. Readings on the pressure transducers and thermal-gas/turbine flow meters were verified with calibration charts and calculated values.

The ignition system was also run for several conditions to ensure that the spark produced was repeatable. Pressure testing was also done on the system. The line pressures were set to a pressure of 1.5 MPa, at this pressure leaks were detected and repaired in the system as well as the lines to ensure a proper propellants delivery to the gun. During this time, installed pressure transducers also verified their readings and measured 1.5 MPa. After component and leak testing, it was desired to maintain a stable repeatable flame.

Initial experience has been gathered from the hardware previously described to test baseline response and functionality. The operability of all newly developed hardware and software is crucial to the completion of the tests required for this study and needs to be validated. The results of these tests are presented in the following sections as well as lessons learned and proposed changes if any.

5.1.1 Initial Hot Firing Tests

Initial testing sessions served to show flaws in setup configuration and safety operations. Following unexpected combustion through detonation and a lag in emergency procedure implementation it was decided to provide easy access to the kill switch. An operator must now always be in charge of the procedure in the event of an emergency. Coolant leaks were apparent during the first rounds of testing; although Dynalene is not a flammable material and poses no risk, gaskets were added to manage the issue and provide effective sealing. Additionally, extra Kevlar walls were positioned to supply hazard management.

The appearance of sparks during the first testing rounds served to show the importance of managing residue inside the lines and setup; when inserting seeding materials these types of issues could be critical in the ultimate output of the coating. The most acute component found to be in necessity of alteration or redesign was found to be the ignition system. Delays in combustion can cause fuel accumulation resulting in either small explosions that can come to degrade the system or in an unexpected fire outside the experimental setup.

5.1.2 Final Hot Firing Tests

Preliminary tests using oxygen and methane were conducted at different Mach numbers and fixed rich equivalence ratio (ϕ) to obtain a stable/repeatable flame with and without introduction of coating particles, Fig. 5.1.

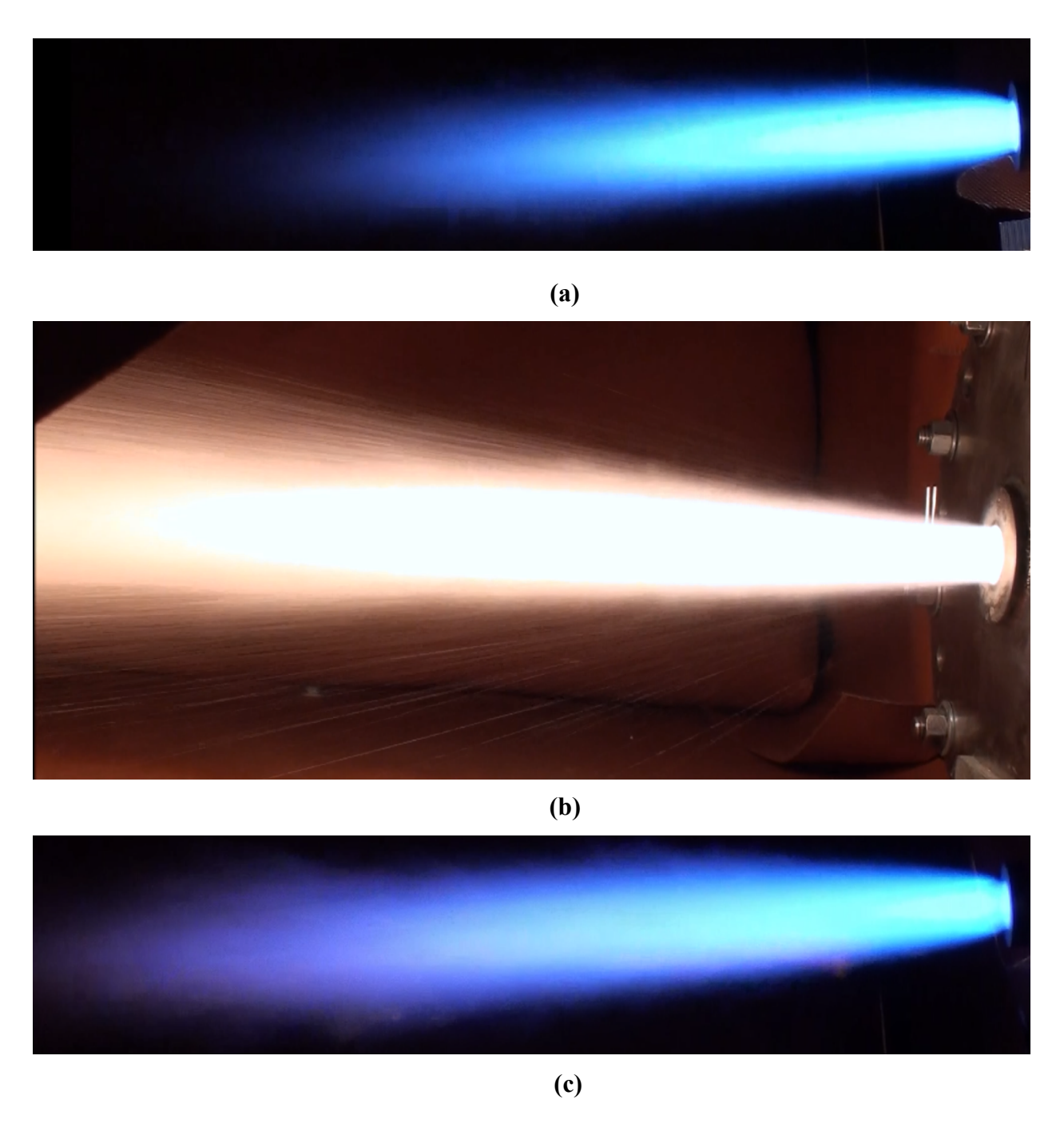


Figure 5.1: Actual HVOF flames at different operating conditions a) Mach of 1.0 and $\phi = 1.1$ (rich) without coating particles, b) Mach of 1.0 and $\phi = 1.1$ (rich) with coating particles, and c) Mach of 1.4 and $\phi = 1.1$ (rich) without coating particles

5.2 Characterization of Coatings

The research objective of this project was to understand the nickel-based and iron-based coatings for harsh high-temperature, corrosive environments. The coatings of interest were investigated for their coating characteristics and morphologies when subjected to different operating conditions and process parameters. The characteristics that were studied are structure, morphology and stability of coatings, and the effects of

thermal cycling, oxidation degradation and the influence of the complex interaction of coating failures.

The surface morphology is examined using scanning electron microscopy (SEM). The size, shape, and distribution of the particles on the surface, surface texture, and surface morphology can best analyzed using this microscopic method. SEM was employed to look at the interface structures and morphological evolution. SEM has many advantages over traditional microscopes. It has a large depth of field, which allows more of a specimen to be in focus at one time. The SEM also has much higher resolution, so closely spaced specimens can be magnified at much higher levels. Because the SEM uses electromagnets rather than lenses, the researcher has much more control in the degree of magnification. All of these advantages, as well as the actual strikingly clear images, make the scanning electron microscope one of the most useful instruments in research today.

The crystal structure and phase analysis of the coatings is performed using X-Ray Diffraction (XRD). To fully understand the structures of complex alloy coatings, it becomes necessary to understand the local or ultra-microstructures, often arising from structural defects or compositional changes. Local structure of the proposed alloy coating is best studied by grazing incidence x-ray diffraction (GI-XRD). These studies provide information on the atomic scale morphology, crystal structure and phase, and substrate-alloy interface structure of the HVOF coatings. The optimized conditions obtained from the microstructure characterization will be employed to prepare superb coatings for future investigations of thermo-mechanical and thermo-chemical properties.

Nanoindentation obtained the hardness and young's modulus of the coating along with other mechanical properties to determine the effects of velocity, temperature, oxidant content and the degree of melting of particles. Additionally, the test will evaluate which sample has a higher resistance to oxidation and higher material's strength to determine which of the parameters are best to meet the objective of durable coatings for high-temperature and harsh environment.

5.2.1 Materials Preparation, Treatment, and Analysis

Specimens/substrates (25.4 x 25.4 x 3.175 mm) were first polished using Acetone and then dried immediately. Since the quality assessment was part of this investigation, the surface modification was extremely essential to enhance and improve the adhesion of the coating. Grit blasting was carried out to roughen the surface, which in turn, removed and cleaned any contamination at the surface of the substrate prior to spraying. Moreover, a sufficient enhancement in the bond strength between the deposited coating and substrate surface was resulted by applying the grit blasting to the substrate surface. The girt blasting

process was conducted to all specimens using 20 mesh Al₂O₃ particles at pressure of 550 kPa to roughen the surface for three minutes. The grid blasted surfaces had roughness on the order of 50 - 60 μm. The specimens were cleaned once more by compressed air prior to apply the desire coating. The HVOF thermal spraying was applied directly after grit blasting process to avoid moisture contamination. A grit blasting machine manufactured by Empire Company was employed to perform the grit blasting process as shown in Fig. 5.2.



Figure 5.2: Grit blasting machine

5.2.2 Operating and Process Parameters

Several operating and process parameters were tested on substrates. One of the parameters chosen was distance, referring to the length in which the substrate is placed and the tip of the HVOF gun; where the substrate gets hit by the flame with the melting particles of the coating. The second parameter was Mach number which can be distinguished for the exit velocity, pressure chamber and exit temperature. Two different materials for the coatings were used, Inconel 718 and iron aluminide (FeAl), for the purpose of comparing the performance of both coatings.

Three different Mach number conditions of the gas flow were investigated. The particular gas velocities of interest corresponded to Mach numbers of 1, 1.2, and 1.4. The number of distances from the tip of the gun were: 50mm, 100mm and 150mm. However, when the hot firing testing was performed, it was observed that at the distance of 50mm and as the Mach number was increased with each test, the produced coating would fall off the substrate. The reason for such low bonding between the materials was due to a high deposition rate which accumulated until the coating was too thick to adhere properly to the substrate. For this reason,

the subsequent data presented would only be for two distances: 100mm and 150mm for Inconel 718. FeAl was sprayed in reduced conditions from the ones of Inconel 718, meaning that not all the parameters were performed for the past coating. Only one distance, 100 mm, and two Mach numbers, 1.0 and 1.2, were done, due to the observation of a decreased coating quality.

Moreover, each sample was subjected to thermal cycling and the data collected for one set of parameters (a specific Mach number with a specific distance) are: a) base sample (no thermal cycling), b) another sample subjected to a temperature of 600°C for 6 hours, and c) a sample that is put under annealing, which was previously subjected to the 600°C and goes into the furnace once again at a temperature of 700°C for 6 hours.

The expected morphology of the particles after spraying are a figure splatted or a particles partially melted with an aura of fully melted material around it making a figure of a sunny up egg according to (Sidhu et al, 2005). The figure they presented is accurate with the morphology that was found for both materials in all the coatings.

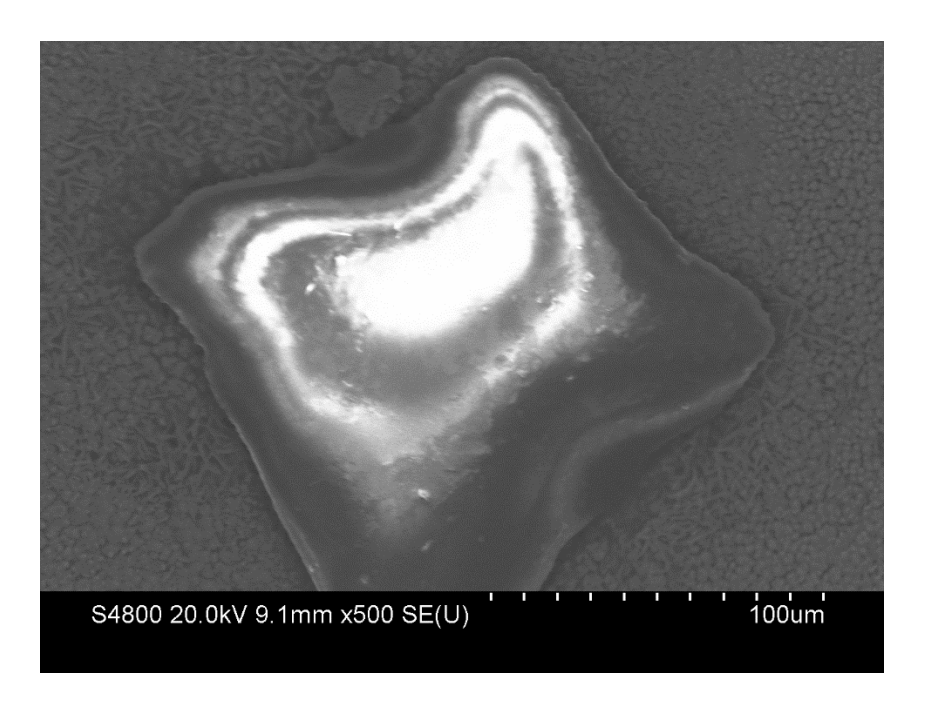


Figure 5.3: Partially melted particle of the HVOF coating after annealing

Samples were examined using a number of surface analysis techniques. X-Ray Diffraction (XRD) was used to XRD was done in order to obtain all diffraction peaks and phases, so that identifying the phases after the thermal cycling can be compared to the literature and know the oxidation phases, which affect the coating by weakening it.

SEM and XRD go hand in hand, since the crystalline size can be compared and validated with the image of the SEM and the calculations of the XRD. The ideal size of the grains that could be observed would be the smallest grain size after annealing. The reason why the smallest grain size are the most desirable is due to when the coating goes under micro fracture, the crack will go through all the grain until it hits another boundary. The smaller the grain size, the slower the crack fracture will propagate, since it needs to go through the boundary to keep moving. The annealing data is the critical data, since after annealing the grain size grows, and the smallest grain size after all the high temperature process would be an indicative of which process parameter would yield the most desirable results.

For Nanoindentation, the aim was to obtain the two most frequent mechanical properties that are measured using load and depth sensing with the nanoindentation techniques. Those properties are the elastic modulus, E, and the hardness, H. In a very common used technique, data is collected from one complete cycle of loading and unloading. The unloading data is then analyzed according to a model for the deformation of an elastic half space by an elastic punch which relates the contact area at peak load to the elastic modulus (Oliver & Georges, 2004). Techniques for independent estimates of the contact area from the indenter shape function are then used to provide separate measurements of E and H.

5.2.3 Inconel 718

The XRD graphs presented have the same intensity peaks for all the samples, therefore a single graph will be shown (Figure 5.4) for all parameters. For Inconel 718, it is observed that the peaks increase in intensity with increasing annealing temperature since they are in oxidation phase. Such is the case of Fe_2O_3 and Cr_2O_3 , where the peak increases in intensity meaning that the w.t. % of those compounds is increasing. It is observed from the XRD that the peaks tend to sharpen with each annealing as the coating's crystallization is increased via heat addition. The peaks match to those found in literature for Inconel 718 (J.A. Sue, T.P. Chang, 1995). The unoxidized sample shows a diffraction peak at 2Θ =45°; there is an overlapping of diffraction peaks belonging to Fe_2O_3 and Inconel 718 compounds.

The size of the grains can be calculate from the XRD graph, using the Scherrer formula:

$$\tau = \frac{K\lambda}{\beta\cos\theta}$$

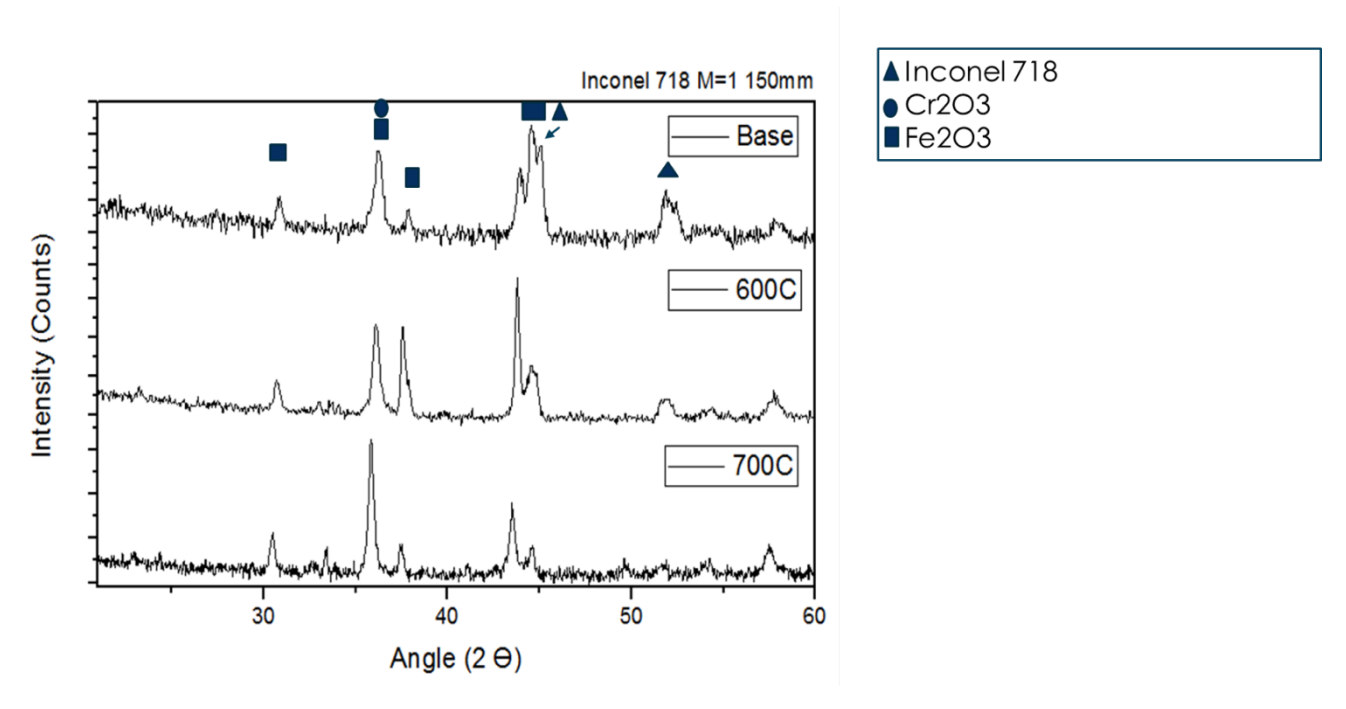


Figure 5.4: XRD graph for Inconel 718

For each individual sample, the crystalline size was calculated through the highest isolated peak, which is located at the 2Θ =35°. The Full width at half maximum (FWHM) was obtained through the analysis software Origin lab, a program that analyses the graph and data obtained from the XRD to calculate different parameters.

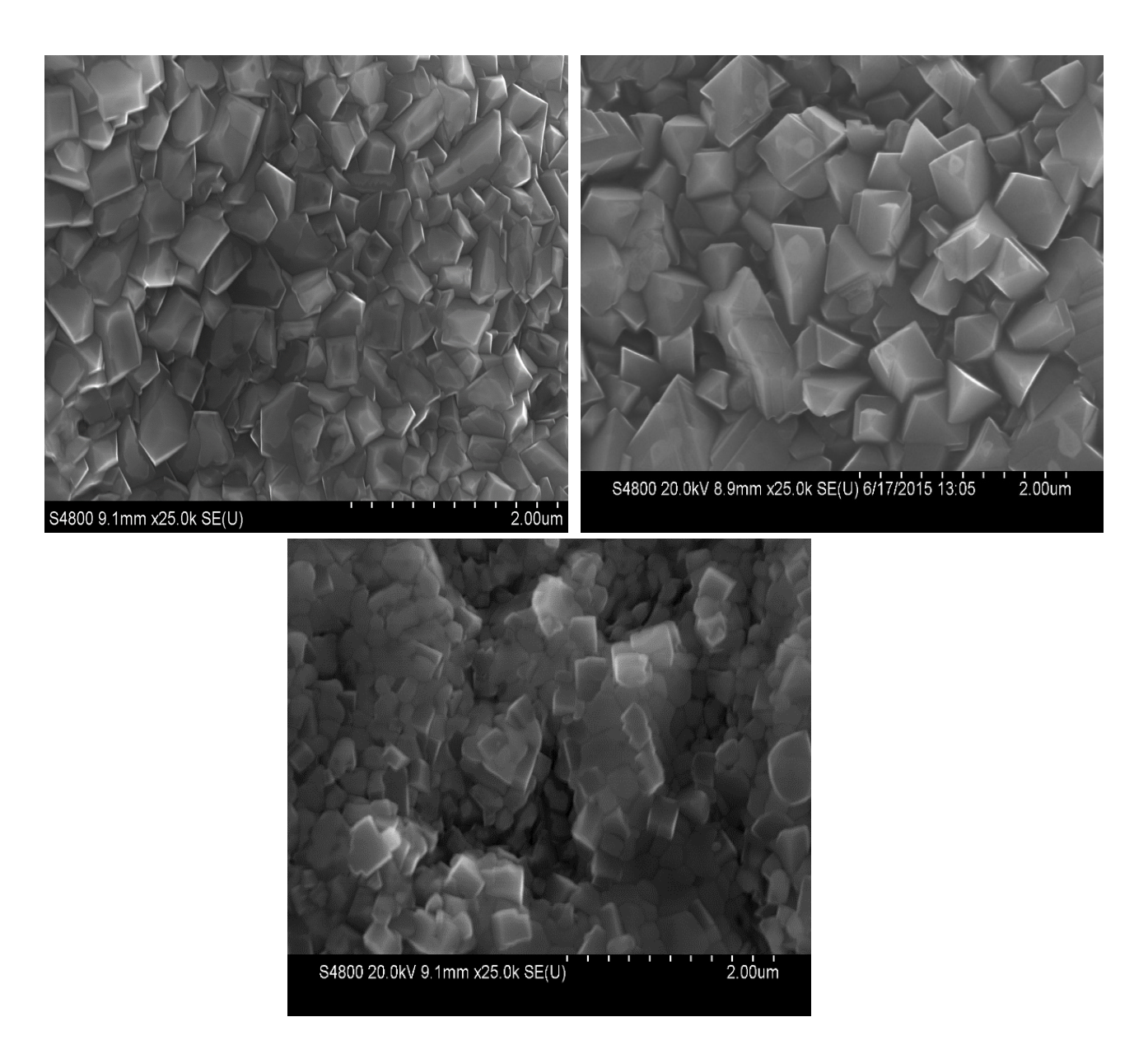


Figure 5.5: SEM images for the fixed parameters 100mm and 700°C, with the different Ma=1, Ma=1.2, Ma=1.4 with a magnification of 25K

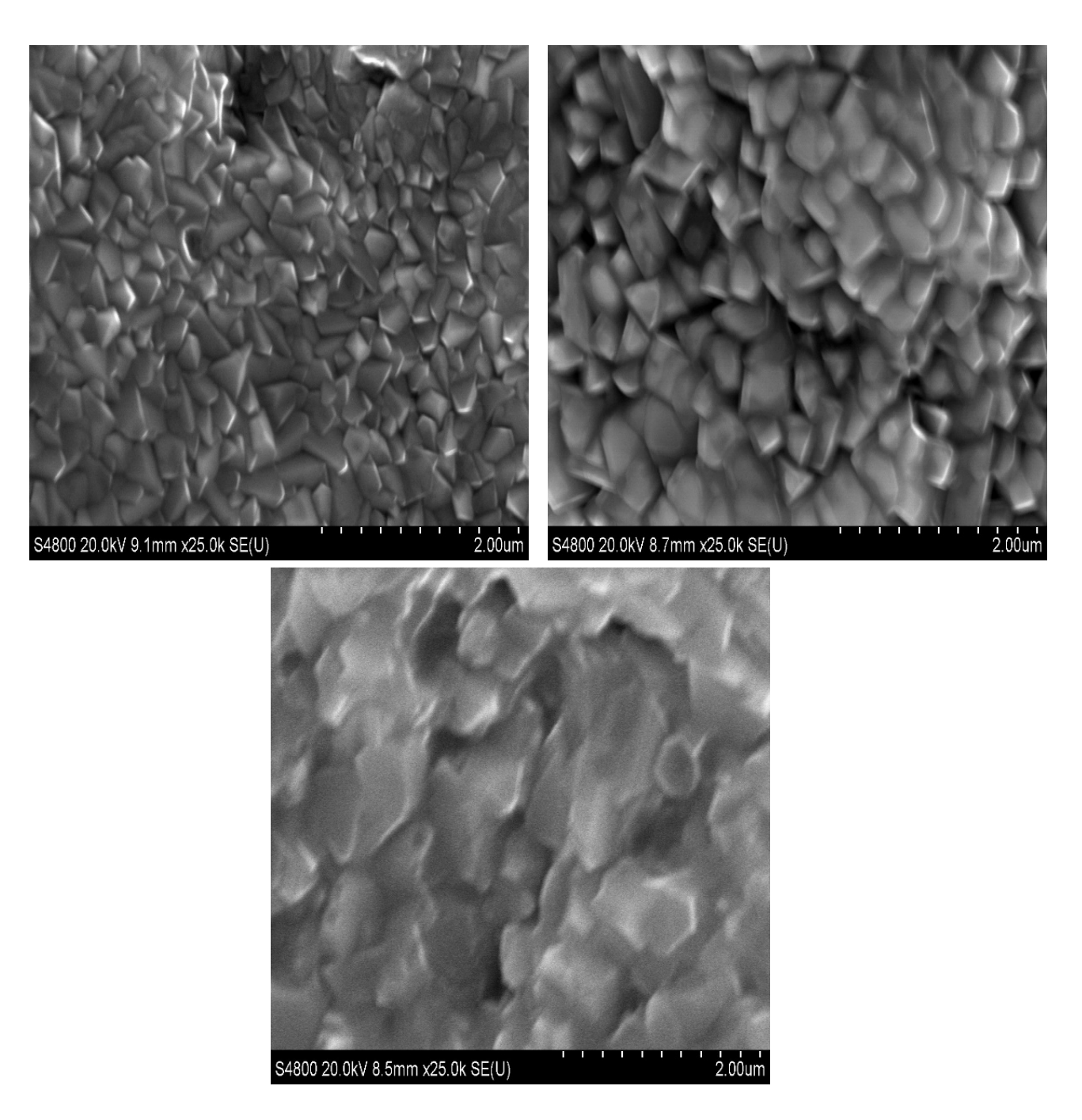


Figure 5.6: SEM images for the fixed parameters 150mm and 700°C, with the different Ma=1, Ma=1.2, Ma=1.4 with a magnification of 25K

Presented in figures 5.5 and 5.6 are the SEM images side to side to determine which grain size is smaller. Estimation of the grain sizes were based on the length scale from the lower right corner of the image. The images that fit the criteria seem to be the third image of figure 5.5 and the first image of figure 5.6. When comparing the calculations for the crystalline size of these two conditions, the smallest one comes out to be the one for Ma=1-150mm of 403.30nm as shown in figures 5.5 and 5.6, which is the smallest grain size of all samples.

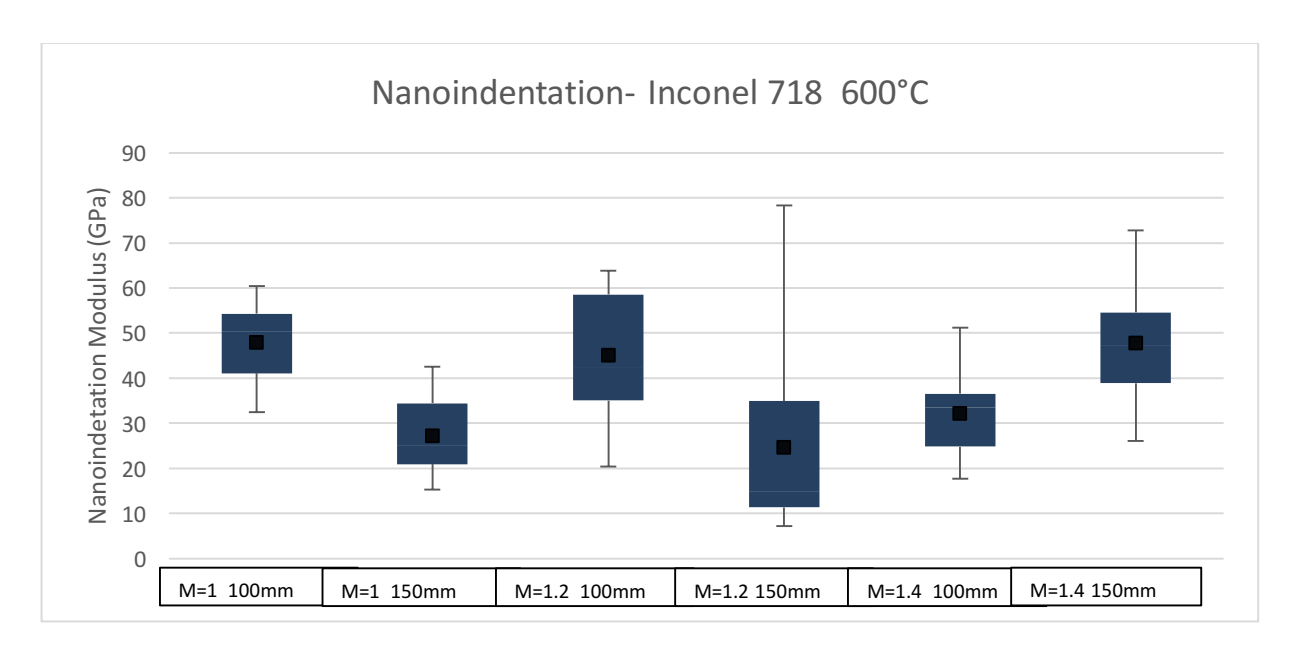


Figure 5.7: Box plot of the data from the nanoindentation at 600°C

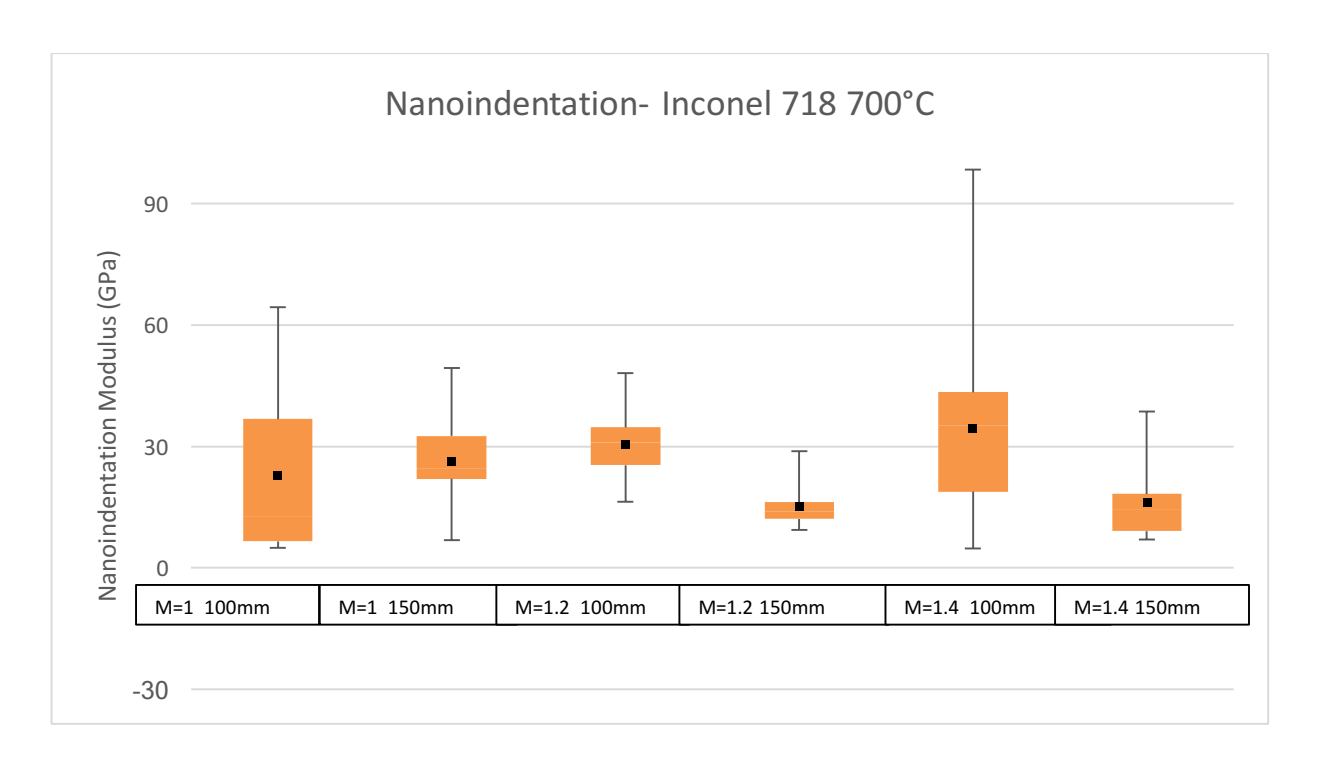


Figure 5.8: Box plot of the data from the nanoindentation at 700°C

Comparing the data obtained and looking for the smallest standard deviation and highest E, the sample that has Ma=1 at 150mm is the best, which is consistent with the sample chosen in the previous sections, as shown in table 5.2.

Table 5.2: Comparison of Mach numbers for the hardness (Inconel 718)

Temperature	Distance					
700°C	M=1	M=1	M=1.2	M=1.2	M=1.4	M=1.4
700°C	100mm	150mm	100mm	150mm	100mm	150mm
MEAN	22.924464	26.3552423	30.4070015	15.2589907	34.5181716	16.2670015
STANDARD	18.853430	10.2991431	8.16155873	5.02359103	21.4562148	8.88671102
DEVIATION						

5.2.4 Iron Aluminide

The other material of coating produced was iron aluminide (FeAl) which has a composition of 70% iron and 20% aluminum according to the specifications found in the material sheet provided by Praxair. This material was chosen for its unique qualities of resisting corrosive environments due to their content of aluminides (Guilemany et al, 2007). No literature source was found to use this exact composition; however at

(Guilemany et al, 2007) they used a powder composition of Fe40wt%Al where the sprayed conditions yielded a w.t. % of 70 % for iron. Therefore the data of that investigation will be used to identify the peaks from the XRD of this study's coatings. After thermal cycling, the corrosive product that has a greater presence on the coating is Fe₂O₃ (iron oxide) and Al₂O₃ (aluminum oxide).

For each individual sample, the crystalline size was calculated through the highest isolated peak, which is located at the 2Θ =33°. The FWHM was obtained through the analysis software Origin lab, a program that analyses the graph and data obtained from the XRD to calculate different parameters.

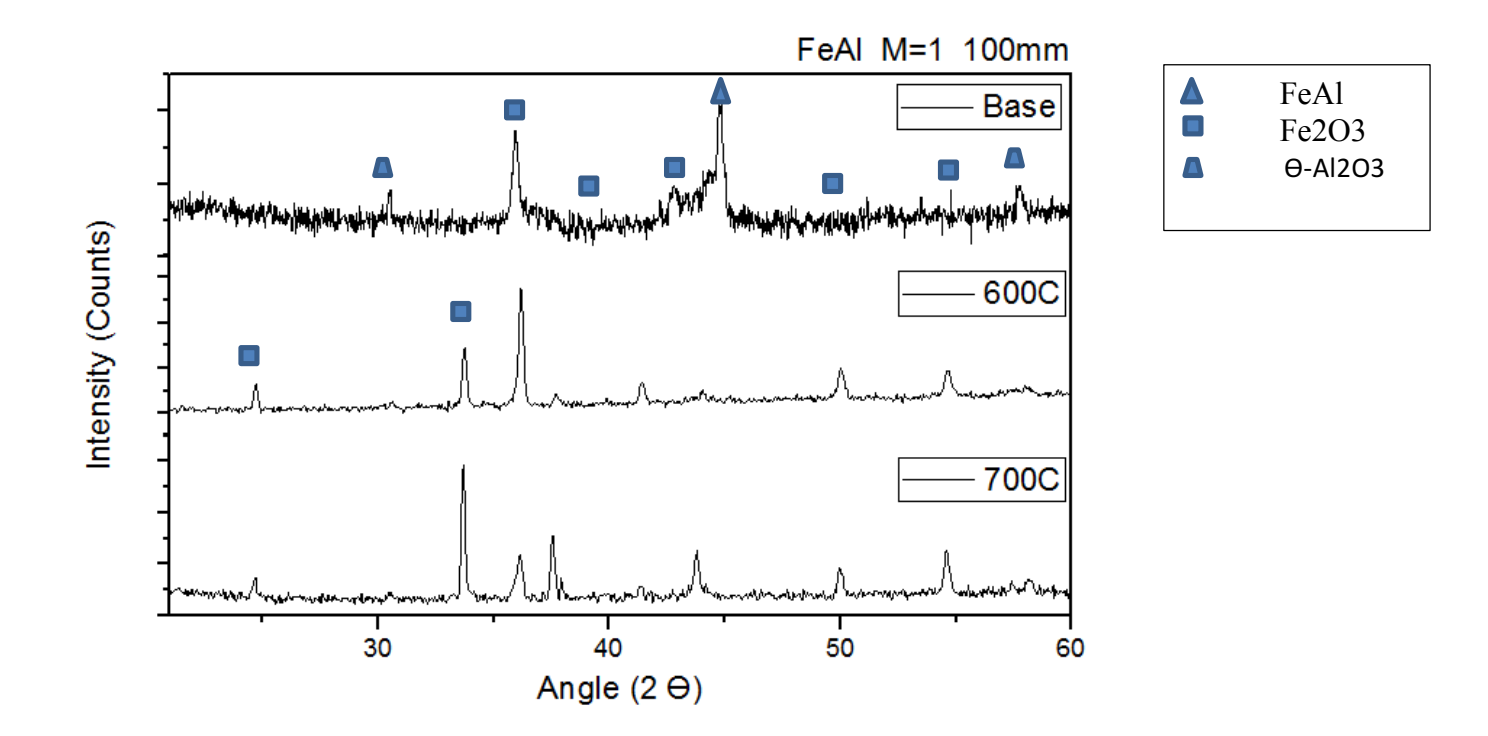


Figure 5.9: XRD graph for Iron Aluminide (FeAl)

70

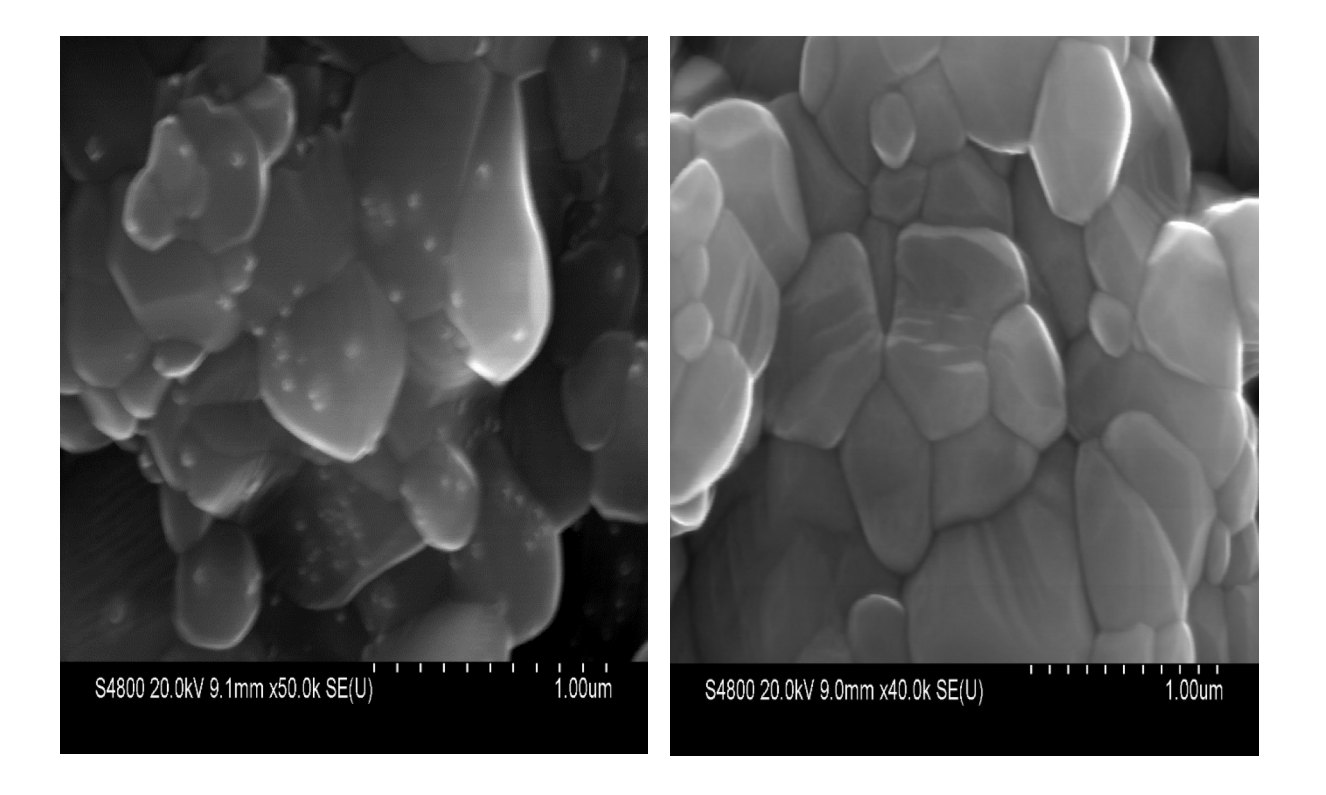


Figure 5.10: SEM images at a scale of 1micrometer and illustrates the different Mach numbers at 700°C

The SEM images shown side to side in figure 5.10 yield an estimation of the grain sizes of 839nm & 553nm for the respective pictures. The size were based on the length scale from the lower right corner of the image. The images that fit the criteria seem to be the second image of figure 5.10, corresponding to the Ma of 1.2 for this particular material where the nanoindentation data can be seen in figures 5.11 and 5.12.

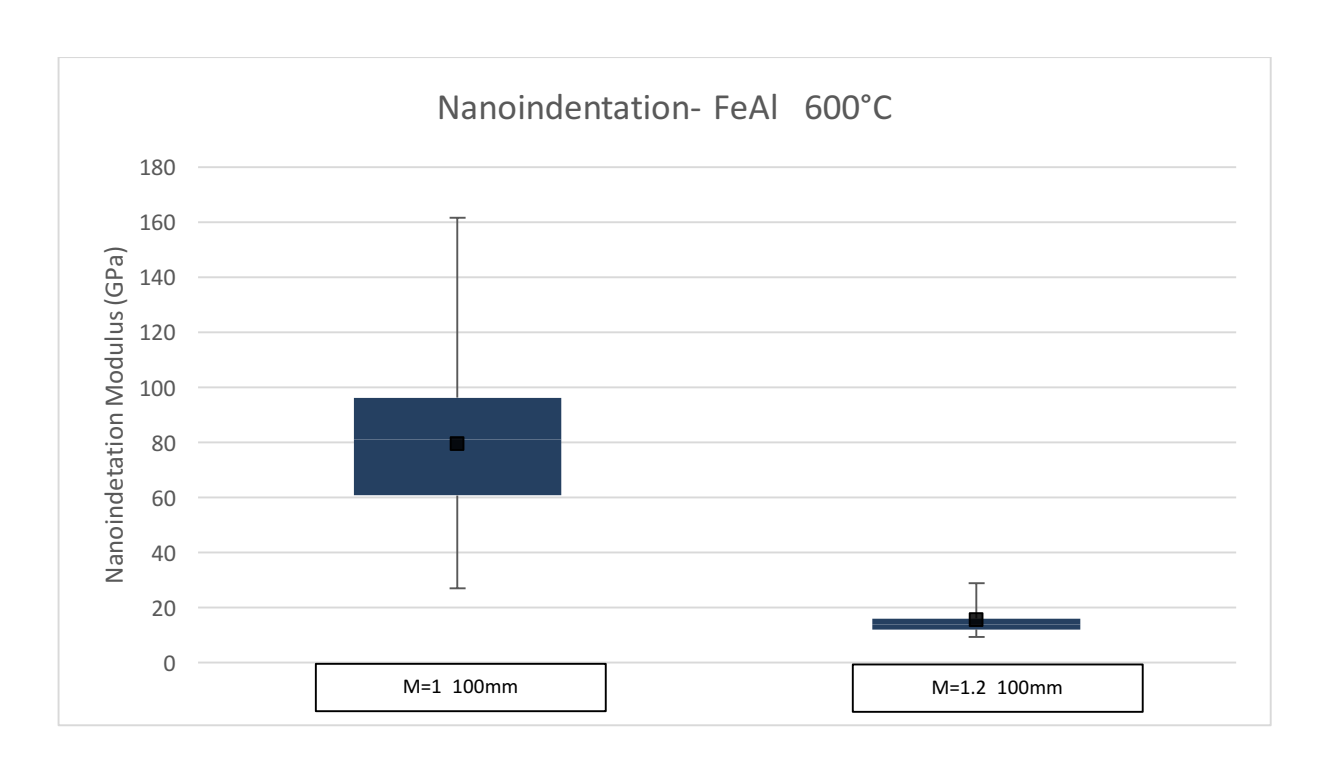


Figure 5.11: Box plot of the data from the nanoindentation at 600°C

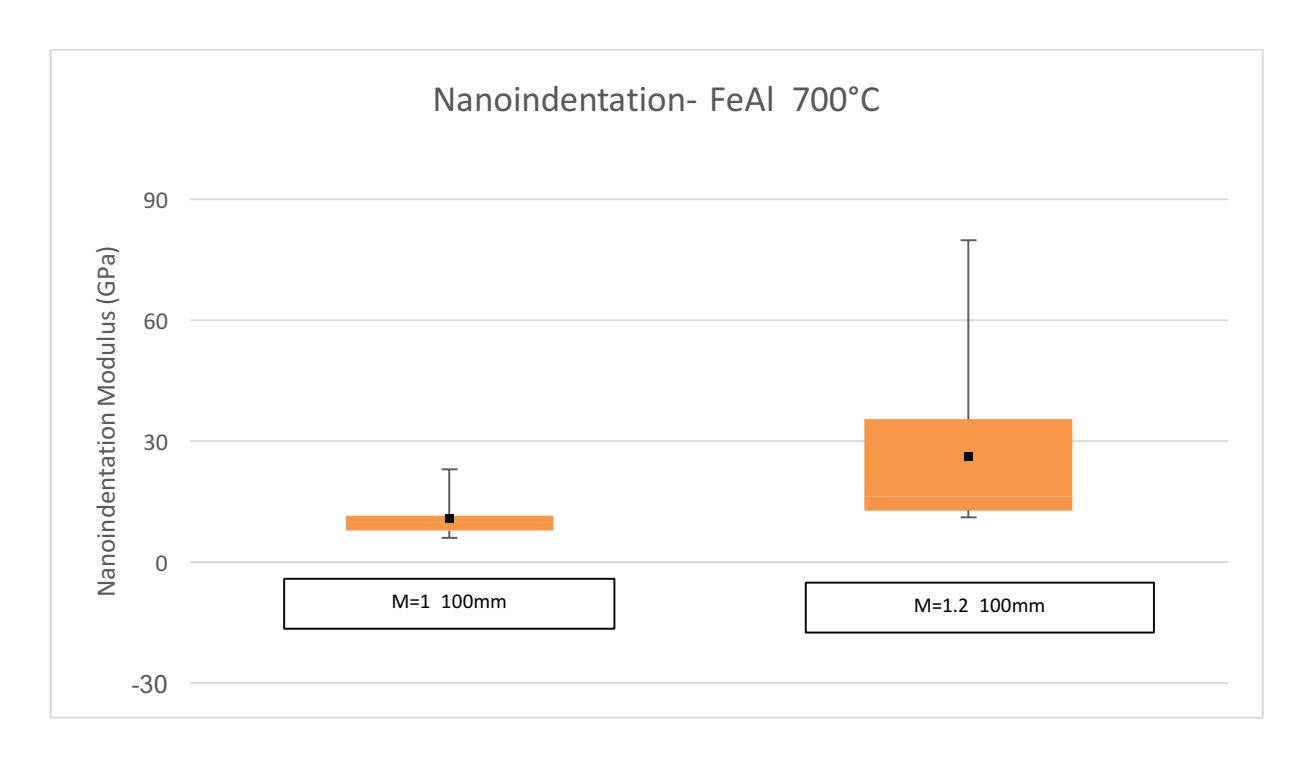


Figure 5.12: Box plot of the data from the nanoindentation at 700°C

Table 5.3: Comparison of Mach numbers for the hardness (FeAl)

Temperature	Distance		
700°C	M=1	M=1.2	
700 C	100mm	100mm	
MEAN	15.40904742	26.50350668	
STANDARD	5.391693614	18.71897761	
DEVIATION	3.371073014	10./109//01	

Comparing the data obtained and looking for the smallest standard deviation and highest E, the sample that has Ma=1 is the sample that shows the highest withstanding of loading as shown in table 5.3.

A limitation noticed was that oxidation may have compromised the samples' yield strength (hardness). One of the factors that influenced this result was the time between in which the sample was subjected to thermal cycling and the nanoindentation test.

Chapter 6: Conclusions and Future Work

6.1 Introduction

A gaseous based HVOF configuration has been developed according to rocket design guidelines. Design was manufactured and assembled with flow monitoring and regulating instrumentation. Setup behavior and flammability ranges have been investigated for a methane-oxygen mixture. Testing revealed initial flaws in lines and remote monitoring arrangements; adequate steps have been taken for the continuous improvement of setup and procedure. Successful tests have shown similar flame shape and oxygen-fuel mixing conditions to industrial HVOF systems with varying exit velocities and overall flow rates. The inclusion of a computational chapter has aided in the understanding of pressure-velocity exchange mechanisms for designed geometry.

- a) Investigation of particle dynamics of gas-fueled HVOF process for a range of operating and process parameters: experimental measurements of particle flux and particle velocity at different operating and process parameters are recommended to be conducted using high speed stereo Particle Image Velocimetry (PIV), while measurements of particle temperature at the same parameters could be performed using high speed two color pyrometer. The measured data should be compared with the included computational simulation data. The proposed test matrix may include testing of:
 - i. Combustion chamber pressure (200, 275, and 350 kPa)
 - ii. Total propellants mass flow rate (10, 15, and 20 g/s)
 - iii. Exit Mach number (1.0, 1.2 and 1.4)
 - iv. Equivalence ratio (ϕ) (0.9, 0.95, 1.0, 1.05, and 1.1)
 - v. Powder feedstock (1.5 and 3 kg/h)
 - vi. Spraying distance (75, 150, 225, and 300 mm)

Future work objectives are as follows:

b) Continuous setup improvement and transition into liquid: as evidenced in the conclusions, the testing setup must be always in the process of redesigning and reconfiguring to achieve the optimal operation of the experimental procedure. Although only one parameter must be changed per objective to properly correlate results with variations, the setup is expected to be able to alter one mechanism at a time until a completely new design is obtained. A liquid-gas combustion must be performed sometime in the future in order to compare the coatings produced by gaseous HVOF system to it. Finally, a system redesign may be able to take place to accommodate components that cannot be

integrated in the current setup (internal thermocouples, pressure sensing device inside the combustion chamber) and/or fulfill a different design approach.

Chapter 7: Commercialization Plan for the HVOF Thermal Spray Gun

7.1 Executive Summary

Advanced power generation plants with increased efficiency require operational parameters that produce extremely corrosive/harsh environments. High Velocity Oxy Fuel (HVOF) thermal spraying system is a highly promising technique for applying durable coatings on structural materials for corrosive/harsh and high temperature environments in advanced ultra-supercritical coal-fired (AUSC) boilers, steam turbines and gas turbines. The HVOF thermal spraying technique is widely applicable to high-temperature coating materials including iron, nickel, and cobalt-based alloys. The process is economical and highly scalable.

After a severe recession and in the midst of a still-sluggish economy, the global thermal spray industry finds itself growing robustly, but with a spotty recovery that has emphasized a few solid markets while others languish. In the next few years, the industry's recovery will be further challenged by growing competition from emerging plated wear coating solutions.

7.2 Development Stage

The newly designed HVOF gun is at the preclinical development stage. In particular, the gun is undergoing a series of reliability tests now.

7.3 Revolutionizing the Commercialization Process

This ideal commercialization cycle for HVOF guns leaves nothing to chance. It selects new initiatives based on financial metrics, and relies on factual data rather than hype throughout each phase of development, as described below:

- Doing the Right Projects
- Clear quantification via financial metrics

The ideal solution will lead to efficient business processes. These processes will enable the creation of a portfolio plan. The overall portfolio plan will clearly quantify the following financial metrics:

- Return on investment
- Profitability and margins

- Cash flows
- Budget fit
- Risk profile

Therefore, the ideal solution will link strategy to execution as shown in Fig. 7.1.

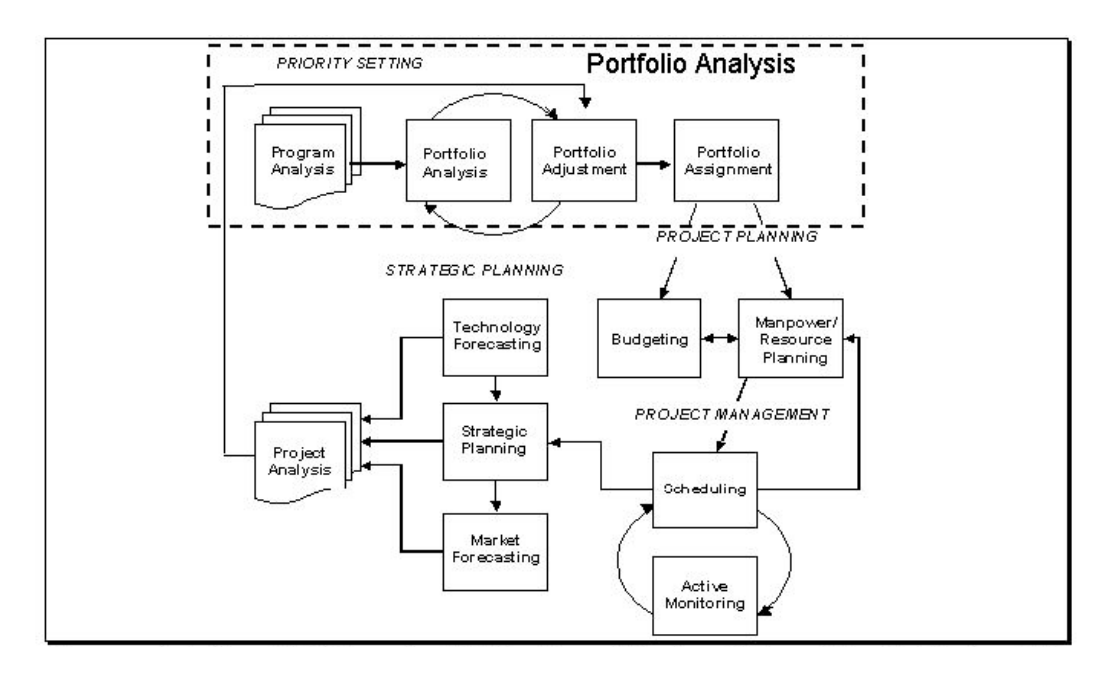


Figure 7.1: Linking strategic planning to project planning and execution (McCoy, 2007)

7.4 Solution: Best Practices

cSETR can achieve the benefits of the ideal solution described above by actively managing their portfolios of investments. An effective management strategy must incorporate three areas of efficiency:

- Automation
- Analysis
- Optimization

7.4.1 Automation

This refers to automating all manual processes. An effective system will let cSETR collect data effectively while also speeding up all processes. For example, many companies will be able to compare, for the first time ever, the actual data for people resource capacity versus the planned need for the resources to fund a new project concept. If a company is analyzing a portfolio of marketing expenditures, it can compare actual

numbers to budgeted numbers by marketing categories: by market segment, product segment, geography or region, or vertical industry. This ability to compare data represents a huge gain in efficiency for companies managing portfolios of new projects.

Automating the portfolio planning cycle will incorporate many steps:

- Collection of business planning assumptions from disparate sources to better evaluate capital funding requests; this data may include:
 - 1. Market forecasts (from product managers)
 - 2. Resource requirements (from development managers)
 - 3. Target costs and rates (from finance managers)
 - 4. Data on existing projects (from product managers)
 - 5. Planned campaigns (from product managers)
- Generation of a baseline portfolio
 - 1. Evaluation of alternative portfolio scenarios
 - 2. Recommendation of an ideal scenario

Once cSETR automates its enterprise project and resource management process, it will be able to:

- Allocate resources at an enterprise level
- Re-allocate resources based on changing priorities for projects
- Trigger warnings due to delays at various stages of the development cycle
- Monitor the status of all projects at the portfolio level

Similarly, once cSETR automates its product data management system, it will be able to:

- Manage engineering changes (ECOs) quickly
- Increase reusability of components, sub-assemblies and designs
- Control documents (including CAD drawings) both internally and across design partners
- Link engineering items and BOMs with those of the manufacturing system
- Monitor costs

7.4.2 Analysis

Analysis gives insight into what has already happened. It provides a scorecard on how well cSETR has executed, by comparing the key indicators for the planned versus actual performance (schedules, resources used, funds expended, etc.). It analyzes historical data, monitors performance threshold levels and identifies where improvements can be made. It gives signals and warnings so cSETR can incorporate workflows to prevent future problems.

Analysis also lets cSETR analyze various "impact" scenarios. For example, cSETR can measure the revenue impact of a delayed product launch, or the profit impact due to a bad decision during the development cycle.

7.4.3 Optimization

Optimization lets cSETR use predictive or forecasting data in addition to the historical data captured by analysis as described above. Optimization incorporates various types of uncertainties by measuring risks through probabilities and qualitative methods. During this stage, cSETR can simulate different business scenarios for its planned portfolio before making a decision.

cSETR can perform very sophisticated sensitivity analyses of the portfolio in varying degrees of detail, including:

- Analysis of groups of related projects at any organizational level (division, enterprise, etc.) for best/worst case scenario modeling
- Portfolio modeling in various dimensions, including: cash flow, margins, delay penalties, net present value (NPV), investment efficiency (ROI) and profit

BIBLIOGRAPHY

- Advance Surface Technology. (2008). Retrieved from www.surfacetechno.com
- Al-Shehri, Y. A. (2011). *Mechanical and Metallurgical Properties of Two-Layered Diamalloy 4010 and 2002 HVOF Coating*. Dublin City University.
- B. Hwang, S. L. (2001). Correlation of microstructure and wear resistance of molybdenum blend coating fabricated by atmospheric plasma spraying. *Material Science and Engineering*, *3*, 152-163.
- B. Wielage, A. W. (2006). Development and Trends in HVOF Spraying Technology. *Surface & Coating Technology*, *6*, 2032-2037.
- Bach FW, M. K. (2004). Particle Image Velocimetry in Thermal Spraying. *Materials Science and Engineering*, 1a, 146–152.
- Bach, F., Mohwald, K., Engl, L., Drobler, E., & Hartz, K. (2006). Particle Image Velocimetry in Thermal Spraying. *Advanced Engineering Materials*, 650-653.
- Basu, S., & Cetegen, B. M. (2008). Modeling of liquid ceramic precursor droplets in a high velocity oxyfuel flame jet. *Acta Materialia*, *56*, 2750-2759.
- C.N. Machio, G. A. (2005). Performance of WC-VC-Co thermal spray coating in Abrasion and slurry erosion tests. *Wear*, *5*, 434-442.
- Cheng D, T. G. (2003). Mathematical modeling of high velocity oxygen fuel thermal spraying of nano crystalline materials: an overview. *Modeling and Simulation in Materials Science and Engineering*, 8.
- Cheng D, X. Q. (2001). A numerical study of high-velocity oxygen fuel thermal spraying process Part I: gas phase dynamics. *Metallurgical and Materials Transactions*, 75, 1609–1620.
- D. Stewart, P. S. (1998). Influence of heat treatment on the abrasive wear behavior of HVOF sprayed WC-Co coatings. *Surface and Coatings Technology*, *32*, 13-24.
- Dolatabadi A, M. J. (2003). Effect of a cylindrical shroud on particle conditions in high velocity oxy-fuel (HVOF) spray process. *Journal of Materials Processing Technology*, 23, 214–224.
- Dongmo E, W. M. (2008). Analysis and Optimization of the HVOF Process by Combined Experimental and Numerical Approaches. *Surface & Coatings Technology*, 76, 4470–4478.
- Dongmo, E., Wenzelburger, M., & Gadow, R. (2008). Analysis and optimization of the HVOF process by combined experimental and numerical approaches. *Surface & Coatings Technology*, 4470-4478.
- Dynalene, C. (n.d.). *Dynalene Selection Guide*. Retrieved from http://www.dynalene.com/Fluid-selection-guide-s/1828.htm

- G.Reisel, B. W. (2001). High temperature oxidation behavior of HVOF-Sprayed unreinforced and reinforced molybdenum disilicida powders. *Surface and Coatings Technology*, *63*, 19-26.
- Goulaouen, G. (1998). Influence of Spray Parameters on Stainless Steel Coating Properties. *Proceeding of the 15th ITS*, 537-545.
- Gourlaouen, G. (1998). Influence of Spray Parameters on Stainless Steel Coating Properties. *Proceeding of the 15th ITS*, *31*, 537-545.
- Gu S, E. C. (2001). Computational fluid dynamic modeling of gas flow characteristics in a high-velocity oxy-fuel thermal spray system. *Journal of Thermal Spray Technology*, 12, 461–469.
- Guilemany, J.M., Cinca, N., Dosta, S., and Lima, C.R.C. (2007), High-temperature oxidation of Fe40Al coatings obtained by HVOF thermal spray, *Intermetallics*, Volume 15, Issue 10, Pages 1384-1394.
- H.Y. Al-Fadhli, J. S. (2006). The erosion-corrosion behavior of high velocity oxy-gen fuel (HVOF) thermally sprayed inconel-625 coatings on different metallic surfaces. *Surface & Coating Technology*, 14, 5782-578.
- Hassan B, O. W. (1995). Computational fluid dynamic analysis of a high velocity oxygen-fuel (HVOF) thermal spray torch. *Thermal Spray Science and Technology*, *54*, 193–198.
- Heath GR, H. P. (1997). An Assessment of Thermal Spray Coating Technologies for High Temperature Corrosion Protection. *Materials Science Forum*, *57*, 809-816.
- Huzel, D. a. (1992). Modern Engineering for Design of Liquid Propellant Rocket Engines.
- J. Tan, L. M. (1999). Component Repair using HVOF thermal spraying. *Journal of Materials Processing Technology*, 47, 203-208.
- J.M. Guliemany, J. F. (2002). Effects of thickness coating on the electrochemical behavior of thermal spray Cr3C2-NiCr coatings. *Surface & Coating Technology*, 75, 107-113.
- Jang HJ, P. D. (2006). Mechanical Characterization and Thermal Behavior of HVOF-Sprayed Bond Coat in Thermal Barrier Coatings (TBCs). *Surface & Coatings Technology*, 4355 4362.
- Jang, H. P. (2006). Mechanical characterization and thermal behavior of HVOF-sprayed bond coat in thermal barrier coatings (TBCs). *Surface & Coatings Technology*, *58*, 4355-4362.
- Jang, H., Park, D., Jung, Y., Jang, J., Choi, S., & Paik, U. (2006). Mechanical characterization and thermal behavior of HVOF-sprayed bond coat in thermal barrier coatings (TBCs). *Surfaace & Coatings Technology*, 200, 4355-4362.
- K. Padilla, A. V. (2002). Fatigue Behavior of 4140 Steel coated with a NiMoAl deposit Applied by HVOF Thermal Spray. *Surface & Coating Technology, 21*, 151-162.

- Kamali, R., & Binesh, A. (2009). The importance of sensitive parameters effect on the combustion in a high velocity oxygen-fuel spray system. *International Communications in Heat and Mass Transfer*, 978-983.
- Kamnis S, G. S. (2005). Numerical modelling of propane combustion in a high velocity oxygen fuel thermal spray gun. *Chemical Engineering and Processing: Process Intensification*, 74, 246–253.
- Kamnis S, G. S. (2008). Mathematical modelling of Inconel 718 particles in HVOF thermal spraying. *Surface & Coatings Technology, 35*, 2715–2724.
- Kamnis, S., & Gu, S. (2006). 3-D Modelling of kerosene-fuelled HVOF thermal spray gun. *Chemical Engineering Science*, 5427-5439.
- Katanoda H, M. H. (2011). Experimental and Numerical Evaluation of the Performance of Supersonic Two-Stage High-Velocity Oxy-Fuel Thermal Spray (Warm Spray) Gun. *Journal of Thermal Science*, 88-92.
- Katanoda, H. M. (2011). Experimental and Numerical Evaluation of the Performance of Supersonic Two-Stage High-Velocity Oxy-Fuel Thermal Spray (Warm Spray) Gun. *Journal of Thermal Science*, 73, 88-92.
- Katanoda, H., Morita, H., Komatsu, M., & Kuroda, S. (2011). Experimental and Numerical Evaluation of the Performance of Supersonic Two-Stage High-Velocity Oxy-Fuel Thermal Spray (Warm Spray) Gun. *Journal of Thermal Science*, 20(1), 88-92.
- Kawakita J, K. S. (2006). Dense Titanium Coatings by Modified HVOF Spraying. *Surface & Coatings Technology*, 86, 1250–1255.
- L. Fedrizzi, S. R. (2004). Bonora, Corrosion and wear behavior of HVOF cermet coatings Used to replace hard chromium Electrochimica Acta. *35*, 2803-2814.
- L. Zhoa, M. M. (2004). Influence of spray parameters on the particle in-flight properties and the properties of HVOF coating of WC-CoCr. *Wear*, *36*, 41-46.
- Li M, C. P. (2003). Modeling and analysis of HVOF thermal spray process accounting for powder size distribution. *Chemical Engineering Science*, *35*, 849-857.
- Li, M., & Christofides, P. (2005). Multi-scale modeling and analysis of an industrial HVOF thermal spray process. *Chemical Engineering Science*, 3649-3669.
- Lim, Y. W. (2007). Tribological behavior of nanostructured WC particles/polymer coatings. *wear*, 65, 1097-1101.
- Lim., Y. W. (2007). Tribological behavior of nanostructured WC particles/polymer coatings. *wear*, 69, 1097-1101.
- Lopez AR, H. B. (1998). Computational fluid dynamics analysis of a wire-feed, high-velocity oxygen fuel (HVOF) thermal spray torch. *Journal of Thermal Spray Technology*, 67, 374–382.

- M, B. S. (2008). Modeling of Liquid Ceramic Precursor Droplets in a High Velocity Oxy-fuel Flame Jet. *Acta Materialia*, 74, 2750–2759.
- M. Hasan, J. S. (2008). Effect of spray parameters on residual stress build-up of HVOF sprayed aluminum/toolsteel functionally graded coatings. *Surface & Coating Technology*, *63*, 4006-4010.
- Marple, R. L. (2003). Optimized HVOF Titania Coatings. *Journal of Thermal Spray Technology*, 32, 360-369.
- Metco, S. (2012). High Velocity Oxy-Fuel (HVOF) Solutions. Switzerland.
- Mostaghimi J, C. S.-A. (2003). Modeling thermal spray coating processes: a powerful tool in design and optimization. *Surface and Coatings Technology*, *67*, 1–11.
- O, S. G. (2010). Rocket Propulsion Elements.
- Oberkampf WL, T. M. (1996). Analysis of a high velocity oxygen fuel (HVOF) thermal spray torch Part 1: numerical formulation. *Journal of Thermal Spray Technology*, 24, 53–61.
- Oberkampf WL, T. M. (1996). Analysis of a high velocity oxygenfuel (HVOF) thermal spray torch Part 2: computational results. *Journal of Thermal Spray Technology*, 63, 62–68.
- Oksa, M., Turunen, E., T, S., Varis, T., & and Hannula, S. (2011). Optimization and Characterization of High Velocity Oxy-fuel Sprayed Coatings: Techniques, Materials, and Applications. *Coatings*, 52, 17-52.
- Oliver, W. C., & Pharr, G. M. (2004). Measurement of hardness and elastic modulus by instrumented indentation: Advances in understanding and refinements to methodology. *Journal of materials research*, Volume *19*, *No.* 1, Pages 3-20.
- P. Gao, C. L. (2008). Influence of substrate hardness on deposition behavior of single porous WC-12Co particle in cold spraying. *Surface and Coatings Technology*, *84*, 384-390.
- Power GD, S. E. (1991). Analysis of a combustion (HVOF) spray deposition gun. *UTRC*, 73, Report No. 91-8.
- S, K. S. (2006). 3-D Modelling of Kerosene-fuelled HVOF Thermal Spray Gun. *Chemical Engineering Science*, *51*, 5427 5439.
- S. Kuroda, Y. T. (2001). Peening Action and Residual Stresses in High Velocity Oxygen Fuel Thermal Spraying of 316L Stainless Steel. *Journal of Thermal Spray Technology*, 41, 367-374.
- Sidhu TS, P. S. (2005). Studies on The Properties of High Velocity Oxy-fuel Thermal Spray Coatings for Higher Temperature Applications. *Materials Science*, *43*, 805-823.
- Smith EB, P. G. (1992). Application of computational fluid dynamics to the HVOF thermal spray gun. *ASM International*, 23.
- Sue, J.A., Chang, T.P. (1995), Friction and wear behavior of titanium nitride, zirconium nitride and

- chromium nitride coatings at elevated temperatures, *Surface and Coatings Technology*, Volumes 76–77, Part 1, Pages 61-69.
- Sutton, G. (2005). History of Liquid Propellant Rocket Engines.
- Swank WD, F. J. (1994). HVOF gas flow field characteristics. *Proceedings of the Seventh National Thermal Spray Conference*, 73, 313–318.
- T.C. Totemeier, R. W. (2002). Microstructure and stresses in HVOF Sprayed Iron Aluminide Coatings. *Journal of Thermal Spray Technology*, *36*, 400-408.
- T.C. Totemeier, R. W. (2003). Mechanical and Physical Properties of High-VelocityOxy-Fuel-Sprayed Iron Aluminide Coatings. *Metallurgical and material Transactions A*, 42, 2223-223.
- T.C. Totemeier, R. W. (2004). Residual Stresses in High Velocity Oxy-Fuel Metallic Coatings. *Metallurgical and material Transactions*, *36*, 1807-1814.
- Tabbara H, a. G. (2009). Computational Simulation of Liquid-fuelled HVOF Thermal Spraying. *Surface & Coatings Technology*, 41, 676–684.
- Tabbara, H., & Gu, S. (2009). Computational Simulation of liquid-fuelled HVOF thermal spraying. Surface & Coatings Technology, 676-684.
- Tang F, A. L. (2004). Characterization of Oxide Scales Formed on HVOF NiCrAlY Coatings with Various Oxygen Contents Introduced During Thermal Spraying. *Scripta Materialia*, 68, 25–29.
- V. Stoica, R. A. (2004). Silding Wear Evaluation of Hot Isostatically Pressed Thermal Spray Cermet Coatings. *Journal of Thermal Spray Technology*, 74, 93-107.
- W. Hu, M. L. (2008). Preparation and properties of HVOF NiAl nanostructured coatings. *Material Science and Engineering A*, 56, 1-8.
- W.C. Lih, S. Y. (2000). Effects of process parameters on molten particle speed and surface temperature and the properties of HVOF CrC/NiCrcoating. *Surface and Coatings Technology*, *52*, 54-60.
- W.J. Trompetter, A. M. (2002). Role of oxides in high velocity thermal spray coatings. *Nuclear Instruments and Methods in Physics Research B*, 36, 518-523.
- Y. Qiao, T. F. (2003). The effects of fuel chemistry and feed stock powder structure on the mechanical and tribological properties of HVOF thermal-sprayed WC-Co coatings with very fine structures. *Surface and Coatings Technology, 43*.
- Yang V, H. M. (2005). Liquid Rocket Thrust Chambers.
- Yang X, a. E. (1996). Numerical analysis of the high velocity oxygen–fuel (HVOF) thermal spray (TS) system. *J. Therm. Spray Technol*, *17*, 175–184.
- Zeoli N, G. S. (2008). Numerical simulation of in-flight particle oxidation during thermal spraying. *Comput. Chem. Eng.*, 18.

Zhang D, H. S. (2003). Microstructure formation and corrosion behavior in HVOF-sprayed Inconel 625 coatings. *Material Science Engineering*, *57*, 45–56.

Appendix A

NOMENCLATURE

English

1	=	Cross section area at nozzle throat	$[m^2]$
A_t		Pressure at nozzle throat	
P_t	=		[Pa]
T _t	=	Temperature at nozzle throat	[K]
T_{e}	=	Temperature at nozzle exit	[K]
m_{t}°	=	Total propellants mass flow rate	[kg/s]
$ m m_o^\circ$	=	Oxidizer mass flow rate	[kg/s]
$ m m_f^\circ$	=	Fuel mass flow rate	[kg/s]
R	=	Gas constant	[J/kg.K]
\overline{R}	=	Universal gas constant	[J/kg.K]
M_{wt}	=	Gas molecular weight	[g/mol]
g	=	Gravitational acceleration	$[m/s^2]$
$^{\mathrm{O}}/_{\mathrm{F}}$	=	Oxygen to fuel ratio	[-]
T_c	=	Combustion chamber adiabatic flame temperature	[K]
P_c	=	Combustion chamber pressure	[Pa]
P_{atm}	=	Atmospheric pressure	[Pa]
M_{a_e}	=	Mach number at nozzle exit	[-]
A_{e}	=	Cross section area at nozzle exit	$[m^2]$
V_{e}	=	Gas velocity at nozzle exit	[m/s]
L^*	=	Combustion chamber characteristic length	[m]
V_c	=	Combustion chamber volume	$[m^3]$
A_c	=	Combustion chamber cross section area	$[m^2]$
D_c	=	Combustion chamber diameter	[m]
L_c	=	Combustion chamber length	[m]
$t_{\rm w}$	=	Combustion chamber wall thickness	[m]
S	=	Allowable working stress	[Pa]
N	=	Number of injector orifices/holes	[-]
A_f	=	Injector fuel orifice cross section area	$[m^2]$

A_{o}	=	Injector oxidizer orifice cross section area		$[m^2]$
C_d	=	Discharge (velocity and jet contraction) coefficient		[-]
ΔP_f	=	Injection pressure drop in the fuel line		[Pa]
ΔP_{o}	=	Injection pressure drop in the oxidizer line		[Pa]
ŭ	=			
P_f		Total pressure load in the fuel line		[Pa]
P_o	=	Total pressure load in the oxidizer line		[Pa]
A_{total}	=	Total heat transfer area		$[m^2]$
Q_{total}	=	Total heat transfer rate		[W]
T_i	=	Coolant inlet temperature		[K]
T_o	=	Coolant exit temperature		[K]
$ {m_{coolant}}$	=	Coolant mass flow rate		[kg/s]
D_{t}	=	Nozzle throat diameter		[m]
D_{barrel}	=	Barrel diameter		[m]
$L_{\rm barrel}$	=	Barrel length		[m]
D_{i}	=	Cooling jacket inner surface diameter		[m]
D_{o}	=	Cooling jacket outer surface diameter		[m]
$C_{p_{coolant}}$	=	Specific heat of coolant		[J/kg.K]
$ ho_{coolant}$	=	Coolant density		$[kg/m^3]$
$V_{coolant}$	=	Coolant velocity		[m/s]
q	=	Average heat transfer rate per unit area		$[W/m^2]$
Greek				
γ	=	Ratio of gas specific heats	[-]	
ρ_{o}	=	Oxidizer density	$[kg/m^3]$	
$ ho_{o_{atm}}$	=	Oxidizer density at atmospheric conditions	$[kg/m^3]$	
$ ho_{ m f}$	=	Fuel density	$[kg/m^3]$	
$ ho_{f_{atm}}$	=	Fuel density at atmospheric conditions	$[kg/m^3]$	
α	=	Divergent nozzle half angle	[°]	
β	=	Convergent nozzle half angle	[°]	

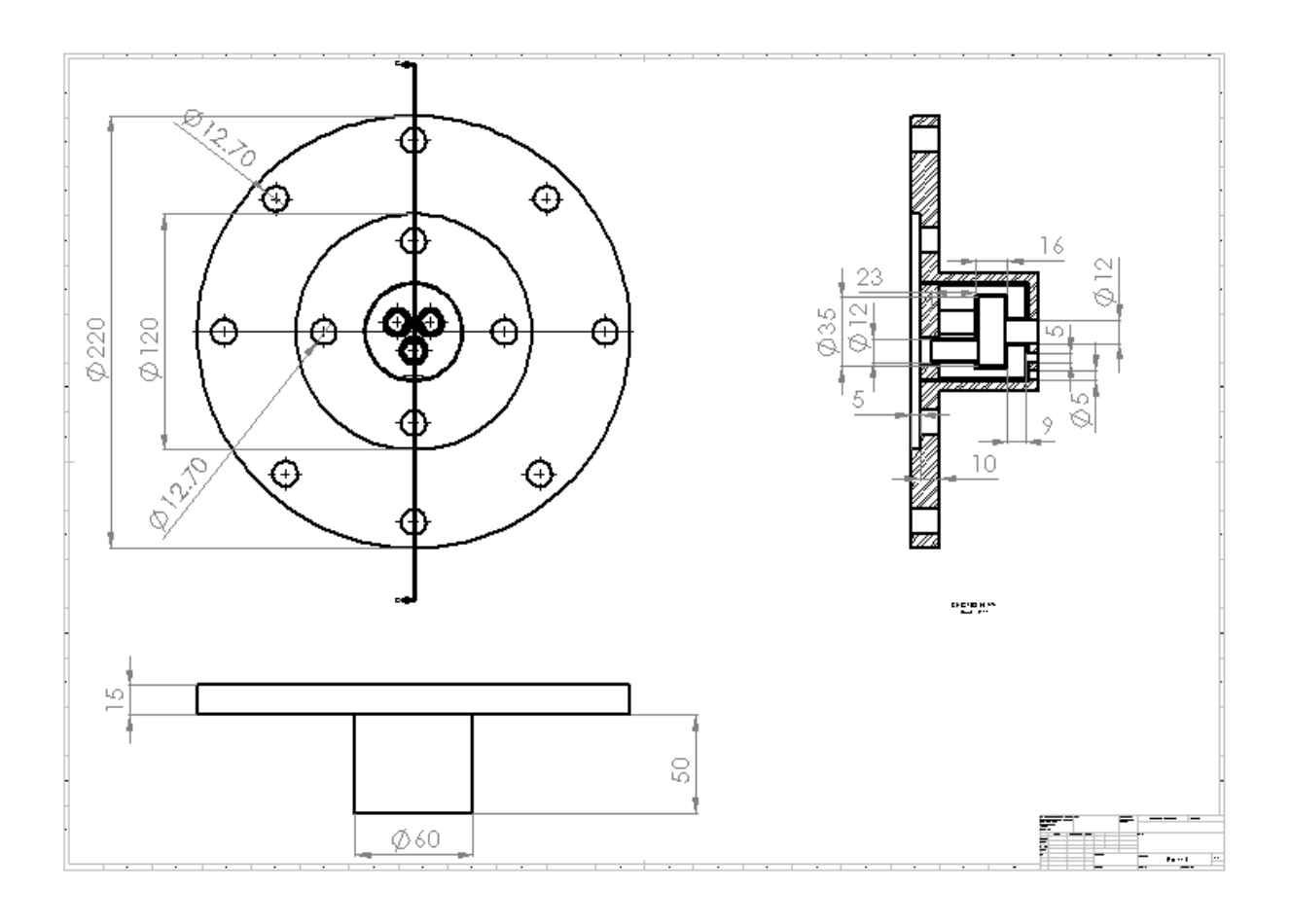


Figure A.1: Detailed schematic of the injector

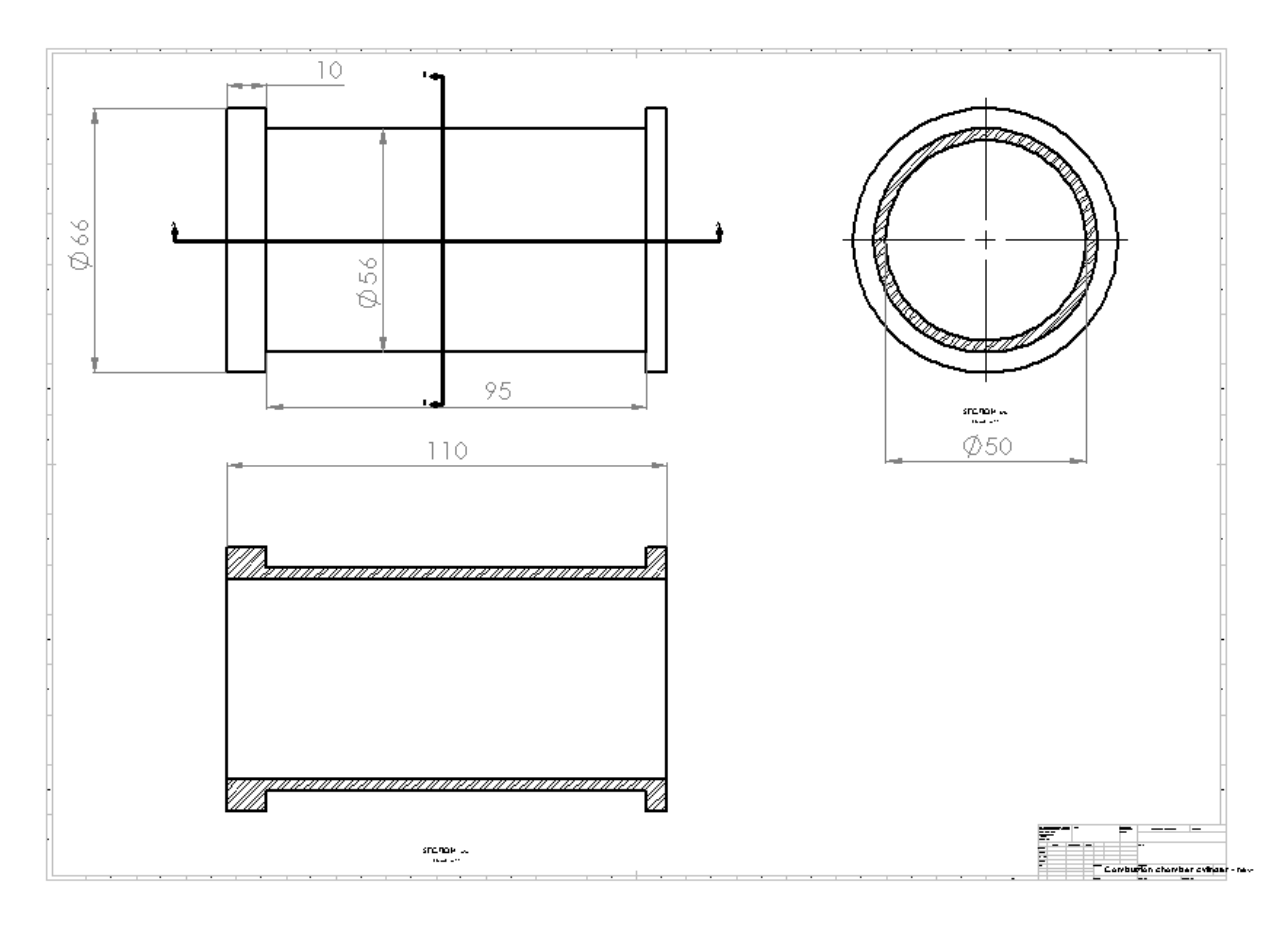


Figure A.2: Detailed schematic of the combustion chamber

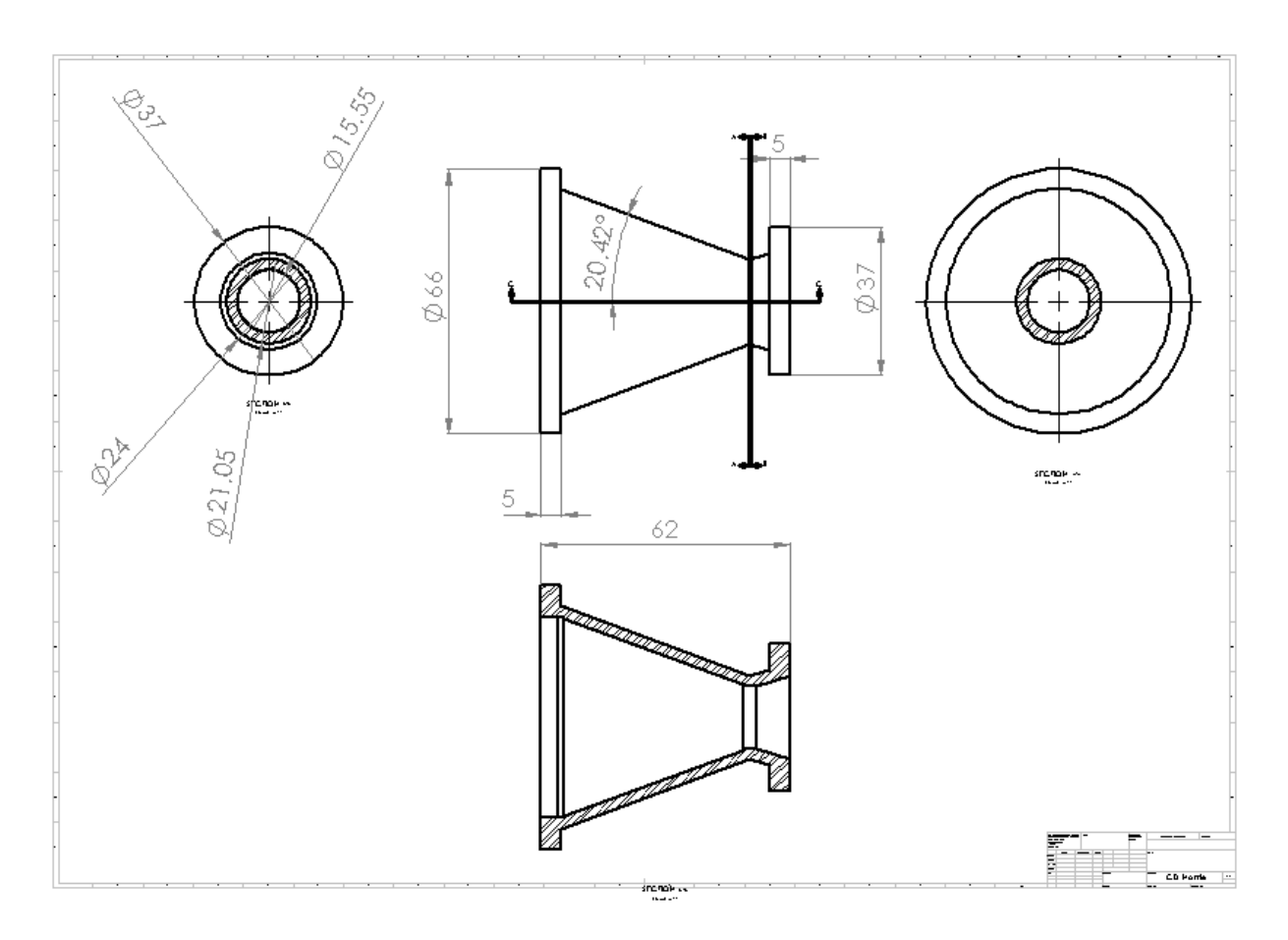


Figure A.3: Detailed schematic of the converging-diverging nozzle

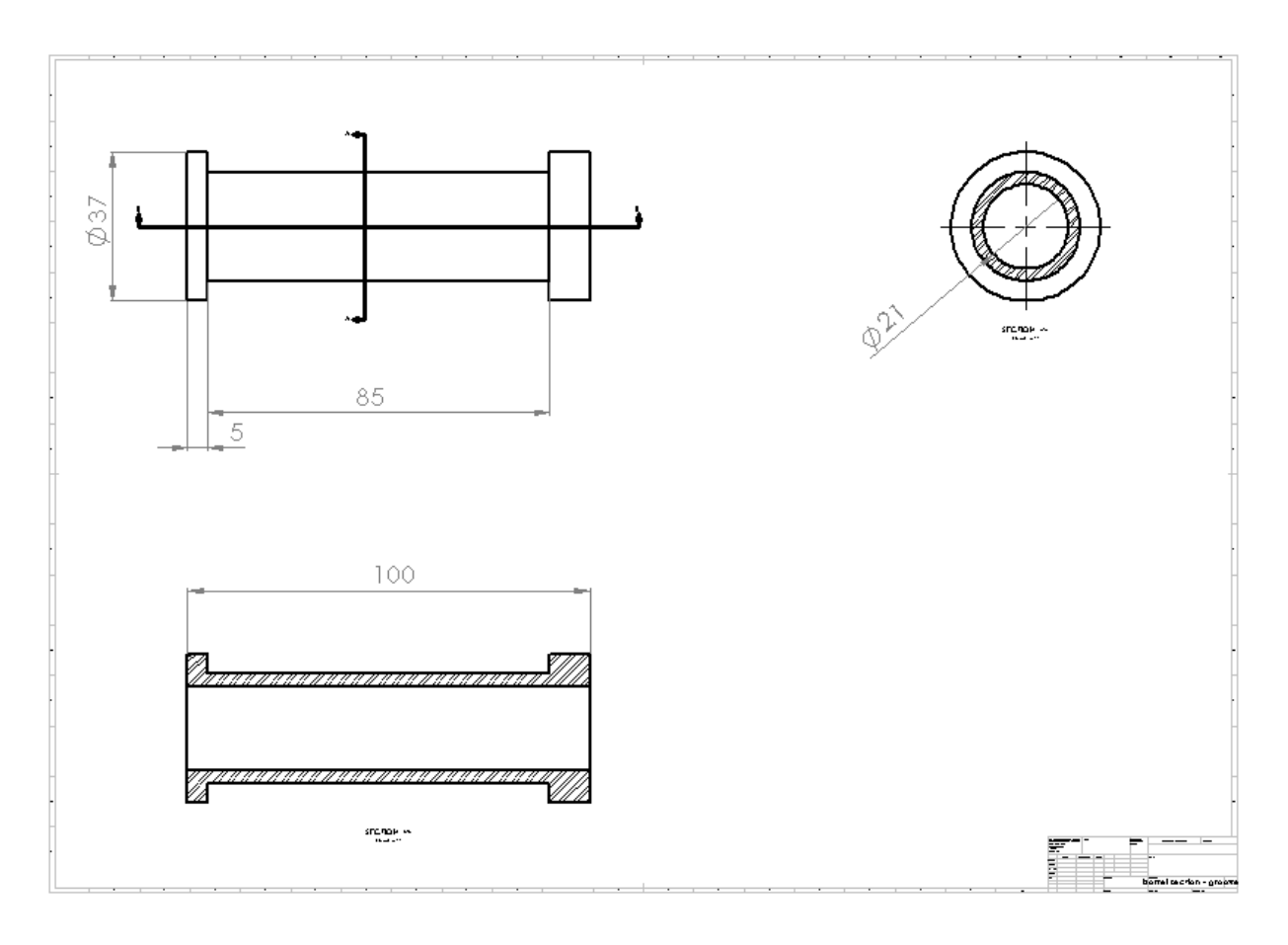


Figure A.4: Detailed schematic of the barrel

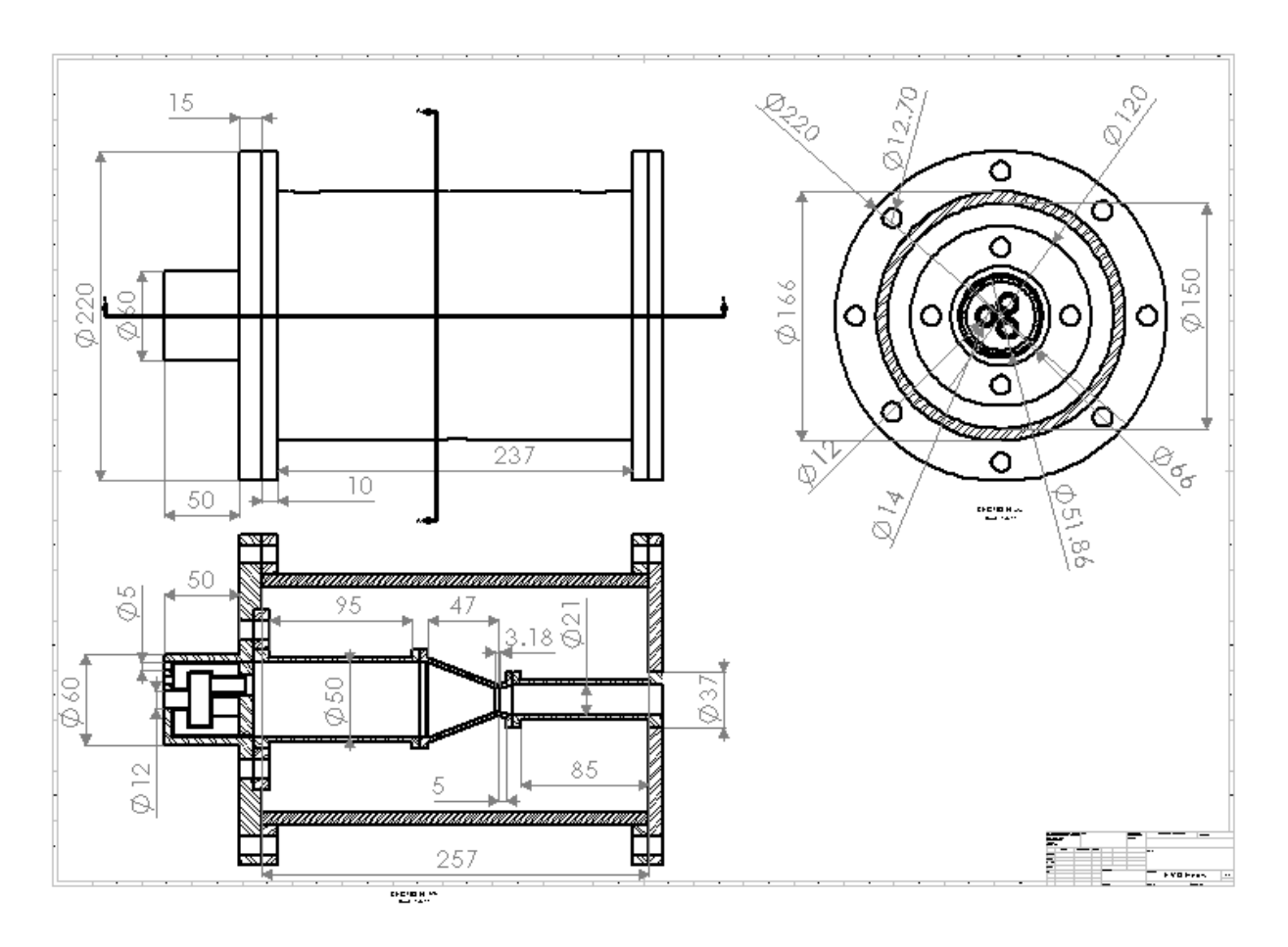


Figure A.5: Detailed schematic of the HVOF thermal spray gun

Appendix B

B.1 Particle Image Velocimetry (PIV)

Particle velocity varies at different positions in the jet depending on the process parameters. Diagnostics for the measurement of particle velocities are very important because the spray particle velocities have a substantial influence on HVOF thermal spraying processes. Analysis of particle velocities in many cases enables a better understanding of the process and possibilities for parameter optimizations could be pointed out. On the one hand, the velocity of a particle enters as a quadratic factor into its kinetic energy; on the other hand, it is responsible for its residence time in the spray jet (Bach FW, 2004). The kinetic energy influences on the adhesive strength and the porosity of a sprayed coating. Monitoring of particle properties at one single location in the jet is not sufficient to describe the complete particle jet. Consequently, a method that measures particle velocity simultaneously at many locations is preferable. Particle image velocimetry (PIV) is a suitable diagnostic tool for the measuring of the particle velocity field over a large area in thermal spraying processes (Bach FW, 2004).

In the last decade, PIV has become a very popular technique of measuring velocities. PIV is a non-intrusive, whole field and direct technique of measuring flow velocity. Figure B.1 provides a pictographic representation of the process. Upstream of the area of interest, micron-sized particles are injected and become entrained in the flow. The flow is then illuminated with a sheet of monochromatic light from a double-pulsed laser. The light reflects off the particles and is recorded by a digital camera timed coincident with the laser pulses. A high speed, high resolution camera is used to record the scattered light by the tracer particles at the two different frames. The camera has to be synchronized with the laser pulses and should be able to separate the images produced by each laser pulse. The lens of a camera, which is perpendicular to the light sheet, collects the light scattered by particles in the flow and projects their images onto camera chip. The recorded graphical photos of the measurement are then digitized for further analysis. Charged couple device (CCD) cameras are commonly used nowadays for PIV recording and have a large number of array sensor elements and very high rate of image capturing.

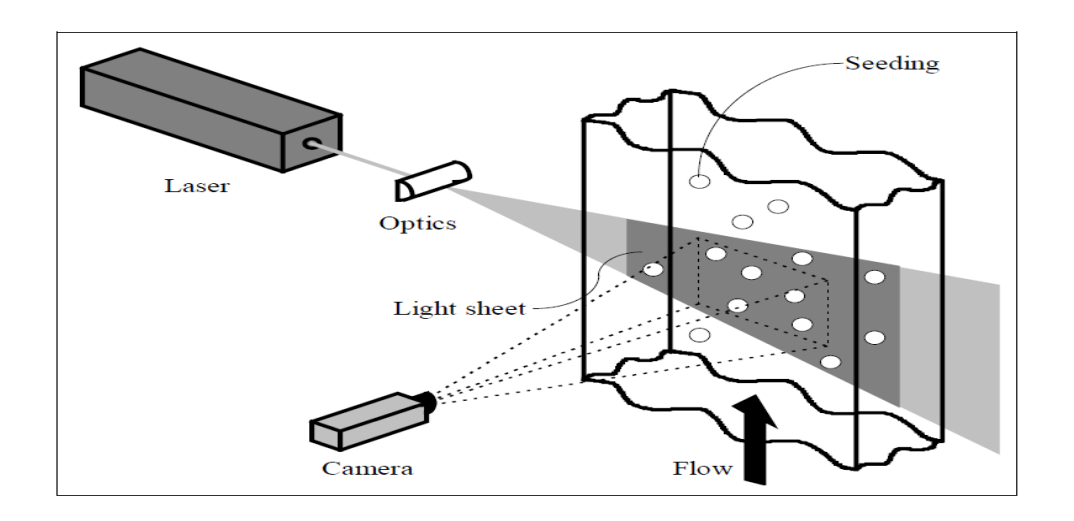


Figure B.1: Basic principles of the PIV system

The camera images are divided into rectangular regions called 'interrogation areas', as shown in Fig. B.2, and for each of these interrogation areas the image from the first and the second pulse of the light sheet are correlated to produce an average particle displacement vector. Doing this for all interrogation areas produce a vector map of average particle displacements. Dividing with the known time between the two images captured, the displacement vectors are converted into a map of so-called 'raw velocity vectors'. In theory, the maximum measurable velocity is a function of the size of the camera's plane of focus and the pulse delay. There are competing interests between dynamic range, spatial, and temporal resolution. In order to measure the maximum velocity, the delay between pulses should be as short as possible. Conversely, the pulse delay must be long enough to accurately determine an image displacement. The optimal pulse delay should be short enough that the majorities of the signals remain in the same interrogation region from one image to the next, but long enough in time that there is a measurable shift.

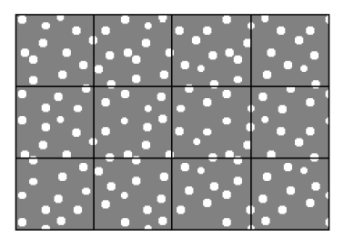


Figure B.2: Interrogation areas in one PIV image

B.2 High Speed Two Color Pyrometer

Continuous temperature measurement is essential to monitor the deposited material temperature while

spraying. A high speed two color pyrometer can be used to measure the molten particles and flame temperature. The optical pyrometer can measure temperatures in the range of 600 to 3300 °C. The pyrometer operates on the principle that all substances at temperatures above absolute zero emit radiant energy, due to the atomic and molecular agitation associated with the temperatures of these substances. As temperature increases the rate of emission of the radiation per unit area increases. The optical pyrometer 'collects' the radiant energy from the work piece from a range of a few millimeters to several meters (approximately 4 meters), thus is practical when direct contact or close proximity sensors are impractical. Some of the advantages of noncontact pyrometry are discussed below:

- It records temperature within fractions of seconds (fast response time).
- It does not influence the temperature and material of the target.
- Requires less maintenance and hence the longer life time.
- It can measure the temperature of the moving object.
- Measurements can be taken for hazardous or physically inaccessible objects (e.g. high-voltage parts and great measurement distance).
- As it is not in direct contact with target so high temperature can be measured.
- Being noncontact technique, it will not tamper the target mechanically.